INTERFACIAL EFFECTS IN BLENDS WITH A LIQUID CRYSTALLINE DISPERSED PHASE

by

PRADEEP K. RAI

A dissertation submitted to the Graduate Faculty in Engineering in partial fulfillment of the requirements for the degree of Doctor of Philosophy, The City University of New York

2004

This manuscript has been read and accepted for the Graduate Faculty in Engineering in satisfaction of the dissertation requirement for the degree of Doctor in Philosophy.

10 June 2004

Distinguished Professor Morton M Denn

Chair of the Examining Committee

6-14-2004

Professor Mumtaz Kassir

Executive Officer

Professor Charles Maldarelli

Professor Carol Steiner

Professor Alexander Couzis

Professor Boris Khusid

Supervisory Committee

THE CITY UNIVERSITY OF NEW YORK

ABSTRACT

INTERFACIAL EFFECTS IN BLENDS WITH A LIQUID CRYSTALLINE DISPERSED PHASE

by

Pradeep K Rai

Advisor: Albert Einstein Professor Morton M Denn

The wide range of applications of liquid crystalline materials has created new areas of academic and industrial research, including multiphase liquid crystalline systems. One of the most important new developments in display technology is the emergence of polymer-dispersed liquid crystals for applications in flat panel television technology and switchable windows. Dispersed liquid crystalline polymers act as "flow modifiers" for conventional thermoplastics, effecting substantial reduction in extrusion pressure at very low concentrations (< 5%). A similar effect is also observed in fiber spinning, in which spin speed is increased.

We have studied dispersions of two biphenylcarbonitriles, 5CB and 8CB, in polydimethylsiloxane as model systems to explore the properties of liquid crystal dispersions. 5CB exhibits nematic and isotropic phases, while 8CB exhibits smectic, nematic, and isotropic phases.

The interfacial tensions between 5CB and 8CB and polydimethylsiloxane were measured as functions of temperature using pendant drop tensiometry enhanced by video-

image digitization. The interfacial tensions are increasing functions of temperature, an apparent consequence of homeotropic orientation in the nematic phase and decreasing nematic order with increasing temperature. Nematic order near the interface persists above the bulk nematic-isotropic transition temperature. The interfacial tension in the smectic phase is too low to obtain a stable droplet.

We describe dielectric spectroscopy measurements on dispersions of 5CB and 8CB in a polydimethylsiloxane matrix. The spectra of the dispersions exhibit a temperature-dependent dielectric relaxation in the range from 100 to 1,000 Hz, with relaxation times that depend strongly on whether the dispersed phase is isotropic, nematic, or smectic. The dielectric relaxation time also depends on the viscosity of the matrix fluid and the droplet size. These results suggest a coupling between the electric field and the mechanics of the interface that affects the spectrum of the dispersed phase and shifts the Maxwell-Wagner interfacial polarization peak.

To simulate the dielectric measurements, we examine the director fluctuations in a radial nematic droplet subjected to an oscillating electric field using the Leslie-Ericksen-Parodi continuum model. The velocity and director fields are obtained analytically for planar and slightly curved nematic systems through a perturbation analysis. The deformation of the planar interface seems to be too small to affect the dielectric measurements.

ACKNOWLEDGEMENTS

This thesis is the result of four and half years of work during which I have been accompanied and supported by many people. It is a great pleasure to have the opportunity to express my gratitude to them.

I wish to express my sincere gratitude to my mentor, Professor Morton M Denn, for his excellent guidance, training, motivation, and assistance during the course of my Ph.D. His great personality and pleasant nature have made my doctoral study a truly gratifying experience. He has been a great advisor and most importantly a true teacher.

I gratefully acknowledge the help and advice of Professor Charles Mardarelli and Professor Boris Khusid. Professor Charles Maldarelli was very helpful in my tensiometry measurements, while all the dielectric experiments were carried out at New Jersey Institute of Technology with the assistance of Professor Boris Khusid. Both of them were constantly aware of the progress in my work, and they provided me with very good directions at every step of the way.

I sincerely thank Professor Carol Steiner and Professor Alexander Couzis for accepting to review my thesis and providing valuable suggestions towards my research work.

I would like to acknowledge the invaluable help of Mr. Andrew Eng, Ms. Mary Wright, and Mr. Zhen Rong Xu in the course of this work.

I thank my group members for their cooperation and valuable suggestions: Dr Xianfeng Li, who is currently working at Mount-Sinai Medical Center in New York City; Fang Xu; Dr. Yogesh Joshi, who is the newest faculty member of IIT Kanpur; John Singh; Rajesh Goyal; and Dr. Yongwoo Inn.

My warmest thanks to all my roommates for rendering me the sense and the value of brotherhood. During the close-to-five years of my stay in New York City, I had many wonderful roommates. Their assistance in chatting, partying, walking, biking, cooking, driving, and just about anything is greatly appreciated. I am especially indebted to my four longest roommates: Chandra, Anil, Manoj, and Jeevan. Their understanding and caring nature will always be a source of inspiration for me.

I am indebted to all my friends at City College and at *Om Sai Mandir*, Flushing who really made my stay in the city of New York both possible and memorable. Their company and constant support made my stay a truly enjoyable experience. A big *grazie* to all my Italian friends.

I would like to express my sincere thanks to my brother and sister-in-law who constantly provided me emotional support and took care of me in many ways. I owe my deep regards to my brother, Pramod Rai, for motivating me to do a Ph.D. at first place. My sister-in-law, Jagriti Sinha, always kept me smiling with her sweet nature. No words of thanks exist to acknowledge the efforts of my parents who have endured so many difficulties for my sake and have been a constant source of encouragement to me. I feel a deep sense of gratitude for my parents who formed part of my vision and taught me the good things that really matter in life.

CONTENTS

LIST OF FIGURES

Chapter 1

INTRODUCTION

Crystalline materials demonstrate long range periodic order in three dimensions. An isotropic liquid has no orientational or positional order. Certain materials do not directly transform from the crystalline solid to the isotropic liquid on heating, but instead exhibit one or more intermediate phases that can flow like a liquid but still retain anisotropic structure and physical properties. These are termed *liquid crystals* or *mesomorphic phases*. Since these phases are obtained by changing temperature, such materials are termed *thermotropic liquid crystals* (TLCs). Alternatively, liquid crystal phases can be obtained by dissolving a sufficient quantity of certain molecules that have a self-ordering tendency in a solvent. These substances are referred to as *lyotropic liquid crystals*. Finally, liquid crystal phases can be produced by change of pressure, in which case they are termed *barotropic liquid crystals*.

Four classes of liquid crystal phases are recognized: nematic, smectic, cholesteric, and columnar. Smectic phases are layered structures, whereas nematics are translationally disordered along the direction of axial symmetry. Columnar phases exhibit two-dimensional order perpendicular to the direction of axial symmetry. If the liquid crystal molecules have chemical groups with a center of symmetry, additional chiral order is imposed on the organization of the liquid crystal phase, which is referred to as cholesteric. Figure 1.1 is a schematic diagram of these phases.

The molecules in liquid crystalline phases are aligned on average with respect to a preferred axis in space called the director. One may define a unit vector $(\vec{n})$ along this

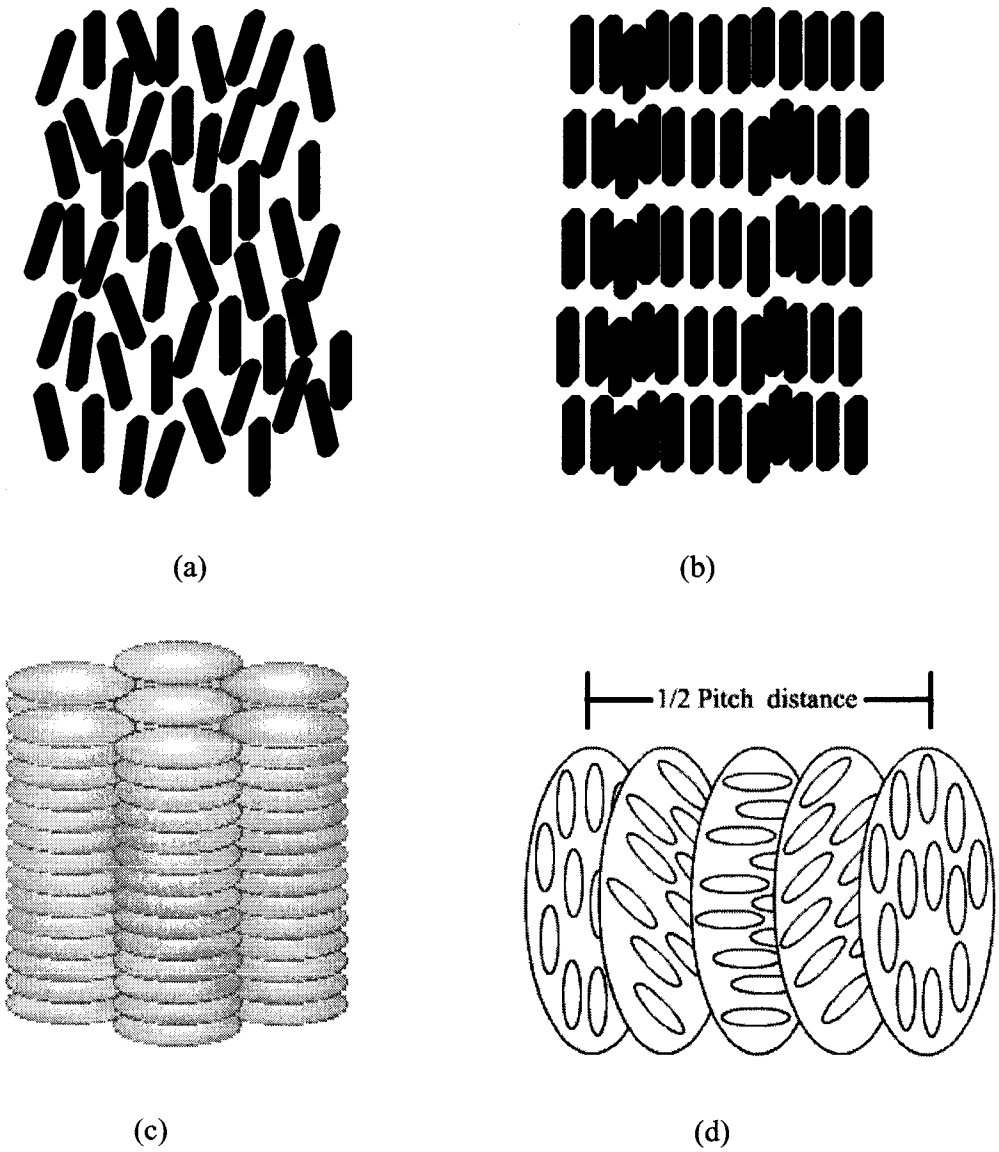

Fig 1.1: Different phases of liquid crystals: (a) Nematic phase, (b) Smectic phase, (c) Columnar phase, and (d) cholesteric phase.

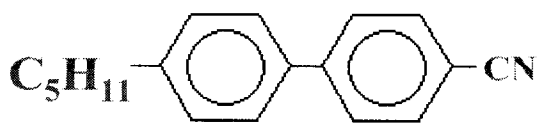

Fig 1.2: The molecular structure of 5CB.

axis and characterize the degree of order with respect to the director by a scalar order parameter S:

$$S = \{3\langle \vec{u}.\vec{n} \rangle - 1\}/2$$

where $\vec{u}$ is a unit vector along the axis of the rod-like molecule, and the angular brackets indicate a configurational average. S has a value between 0 (complete disorder) and 1 (perfect order) for rod-like molecules, and S typically decreases with increasing temperature within the liquid crystal state. The director for a disc is orthogonal to the surface; hence, S has a value of –1/2 for a perfectly ordered columnar phase. Typical values for the order parameter of a nematic liquid crystal range between 0.3 and 0.9, depending on temperature or concentration.

Rod-like low molar mass liquid crystals (LMMLC) require an extended conformation of the molecule, which must be maintained through the rigidity and linearity of its constituents. That is, in order for a molecule to display the characteristics of a liquid crystal, it must be rigid and rod-shaped. This is often accomplished by the interconnection of two rigid cyclic units. The interconnecting group should cause the resulting compound to have a linear planar conformation. Linking units containing multiple bonds such as -(CH=N)-, -N=N-, -(CH=CH)n-, -CH=N-N=CH-, etc. are used, since they restrict the freedom of rotation. These groups can conjugate with phenylene rings, enhancing the anisotropic polarizability. This increases the molecular length and maintains the rigidity. 5CB (a rod-like LMMLC) is shown in Fig. 1.2.

1.1 Characterizing Liquid Crystals

Positional order, orientational order, and bond orientational order describe the extent to which the liquid crystal sample is ordered. Positional order refers to the extent to

which an average molecule or group of molecules shows translational symmetry (as in a crystalline material). Orientational order represents a measure of the tendency of the molecules to align along the director on a long-range basis. Bond orientational order describes a line joining the centers of nearest-neighbor molecules without requiring a regular spacing along that line.

1.1.1 Electric and Magnetic Field Effects

The response of low molar mass liquid crystal molecules to an electric or magnetic field is the major characteristic utilized in industrial applications. The ability of the director to align along an external field is caused by the electronic structure of the molecules. Permanent electric dipoles result when one end of a molecule has a net positive charge while the other end has a net negative charge. When an external electric field is applied to the liquid crystal, the dipole molecules tend to orient themselves along the direction of the field.

Even if a molecule does not form a permanent dipole, it can still be influenced by an electric field. In some cases, the field produces a slight re-arrangement of electrons and protons in molecules such that an induced electric dipole results. While not as strong as permanent dipoles, orientation with the external field still occurs.

The effects of magnetic fields on liquid crystal molecules are analogous to electric fields. Because moving electric charges generate magnetic fields, electrons moving about atoms produce permanent magnetic dipoles. When a magnetic field is applied, the molecules will tend to align with or against the field.

1.2 Liquid Crystalline Polymers

Liquid Crystalline Polymers (LCPs) are a class of polymers that exhibit liquid crystalline properties. These "hybrids" show the same mesophases characteristic of ordinary liquid crystals, yet retain many of the useful and versatile properties of polymers.

In order for polymers to display liquid crystalline characteristics, rod-like or disk-like elements (called mesogens) must be incorporated into their chains. The placement of the mesogens plays a large role in determining the type of LCP that is formed. Main-chain liquid crystalline polymers, or MC-LCPs, are formed when the mesogens are themselves part of the main chain of a polymer. Conversely, side chain liquid crystalline polymers, or SC-LCPs, are formed when the mesogens are connected as side chains to the polymer by a flexible "bridge" (called the spacer). Figure 1.3(a) shows the mesogens and polymer arrangements in MC-LCP and SC-LCP. Figure 1.3(b) is a typical repeating unit in a side chain liquid crystalline polymer. Note the spacer of methylene units and the mesogen of aromatic rings.

Other factors influencing the mesomorphic behavior of polymers include the presence of long flexible spacers, molecular weight, and regular alternation of rigid and flexible units along the main chain.

1.3 Applications

Liquid crystalline (LC) materials were discovered more than one hundred years ago, but the scientific principles that govern their transport and elasto-magneto-optical

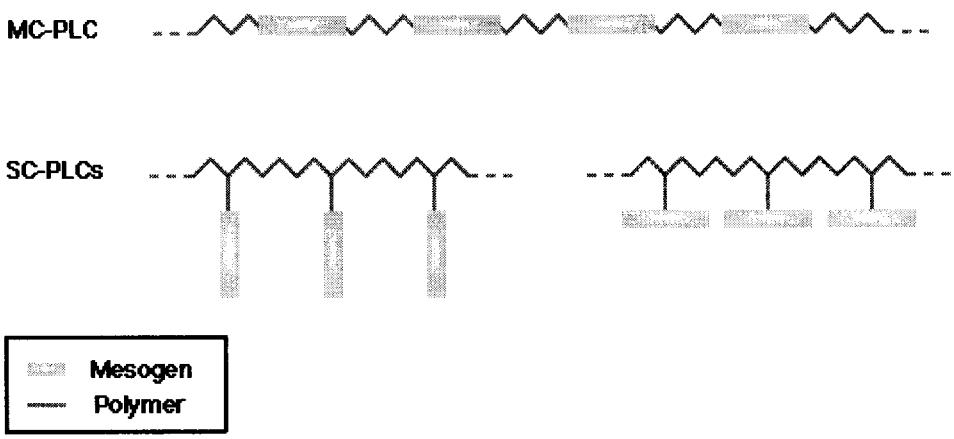

(a) Cartoon of main chain and side chain LCP

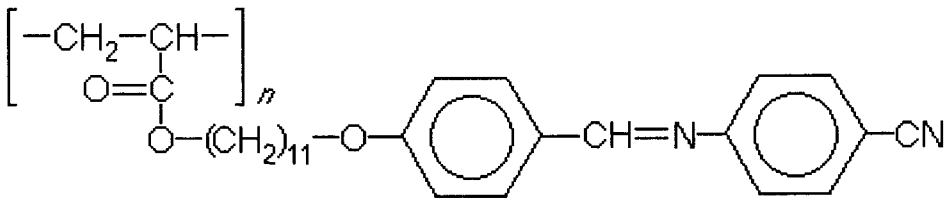

(b) Repeating unit in a side chain LCP

Fig 1.3: Liquid Crystalline Polymers.

properties were established only recently. These materials have a wide array of technological applications, such as electro-optical displays (low molecular mass liquid crystals) and high performance fibers (liquid crystalline polymers). Thermotropic liquid crystalline polymers (TLCPs) have great potential as structural materials; they have high strength and stiffness in the direction of molecular alignment and their low melt viscosity facilitates processing. A potential application of side chain TLCPs is in optical data storage systems. Liquid crystalline substances also have the ability to detect extremely small changes in temperature, mechanical stress, electromagnetic radiation, and chemical environment.

1.3.1 High-Strength Fibers

An application of liquid crystalline polymers that has been successfully developed for industry is the area of high strength fibers. Kevlar, which is used to make such things as helmets and bulletproof vests, is just one example of the use of lyotropic liquid crystalline polymers in applications calling for strong, lightweight materials.

Thermotropic main chain liquid crystalline polymers are also well suited to ordering processes. For example, the polymer can be oriented in the desired liquid crystal phase and then quenched to create a highly ordered, strong solid. It has not been possible to develop molding technologies that maintain nematic order in TLCPs over distances greater than about 10 micrometers, however.

1.3.2 Optical Applications

The use of liquid crystalline polymers in the display industry is an exciting area of research. At this time, LCPs demonstrate relatively slow response times to electric fields.

That is, when a field is applied, the molecules take a long time to align. This is not a good property for use in displays where the screen must be able to change rapidly from one view to another.

In applications for which response time is not a factor, a twisted nematic liquid crystalline polymer cell can be used to make energy efficient displays. A laser is used to selectively melt portions of the display into the liquid crystal phase. The orientation of the cell is then fixed by application of a field, just as in an ordinary twisted nematic liquid crystal cell. When the polymer cools down and hardens into a glass, the mesogens will be locked into that configuration and the field can be turned off.

Side chain liquid crystalline polymers exhibit good properties for applications in optically nonlinear devices, including optical waveguides and electro-optic modulators in poled polymeric slab waveguides. More devices are expected to be fabricated from LCPs in the future: optically addressed spatial light modulators, tunable notch filters, optical amplifiers, and laser beam deflectors. The properties of ferroelectric chiral smectic C phases make this material useful for films with applications in nonlinear optics.

1.4 Organization of Thesis

The focus of this thesis is investigating the interfacial effects in blends with a liquid crystalline dispersed phase as probed by rheometry, tensiometry and dielectric spectroscopy.

In *chapter 2*, the controlled stress rheometry of low molar mass liquid crystals is presented. The theory for dynamic measurements on a cone-and-plate rheometer is developed. The effects of fluid inertia and the moment of inertia of the rotating fixture of the rheometer are discussed.

In *chapter 3*, the pendant drop tensiometry of the liquid crystal – silicone oil interface is described. In contrast to the usual temperature dependence, the interfacial tensions of 5CB and 8CB against silicone oil are increasing functions of temperature in the nematic phase, show a small decrease in passing through the bulk nematic-isotropic transition, and are again increasing functions of temperature in the isotropic phase. This observation is rationalized on the basis of recent molecular simulations and optical observations.

Chapter 4 is devoted to the dielectric spectroscopy of 5CB and 8CB dispersions in silicone oil. The spectra of the dispersions exhibit a temperature-dependent dielectric relaxation in the range from 100 to 1,000 Hz, with relaxation times that depend strongly on whether the dispersed phase is isotropic, nematic, or smectic. The dielectric relaxation time also depends on the viscosity of the matrix fluid and the droplet size. These results suggest a coupling between the electric field and the mechanics of the interface that affects the spectrum of the dispersed phase and shifts the Maxwell-Wagner interfacial polarization peak.

Chapter 5 deals with the coupling of liquid crystal dynamics at the interface with the applied alternating electric field. In the first part, the deformation of a planar interface is evaluated theoretically. The deformation of the interface seems to be too small to affect dielectric measurements, probably because of the absence of curvature effects. In the second part, the director fluctuations in a radial nematic droplet are examined.

Chapter 6 concludes this work and suggests directions for future work.

Chapter 2

RHEOMETRY of LOW VISCOSITY FLUIDS

Rheology is the study of the flow and deformation of matter. In its widest sense, rheology includes classical fluid mechanics, which treats the flow of Newtonian liquids such as water, and linear elasticity, which treats small deformations of hard solids, such as wood and steel. In a gross sense, a rheological measurement tells one how "hard" or "soft" a material is, and it indicates how "fluid-like" or "solid-like" a material is. These characteristics of a material depend on the time scale at which the material is probed. For example, a ball of "silly putty" will bounce like an elastic solid if suddenly dropped, but it will flow like honey if left to rest on a table top. A rheometer measures the rheological properties of a complex fluid as a function of rate or frequency of deformation.

The liquid crystal dispersions of interest in this work are low-viscosity, relatively inelastic materials. Rheological measurement for such materials presents particular difficulties, which are illustrated in this chapter.

2.1 THEORY

There are various kinds of viscometric flows, as discussed in Bird *et al.* (1987), that can be utilized for measuring material functions. Here we will be concerned with only two: flow between two parallel disks, and flow between a cone (with very small angle) and a plate. With either of these geometries we can either impose a steady shear flow or a small amplitude oscillatory flow.

In steady isothermal shearing flow of an incompressible fluid in which the velocity vector is $(\dot{\gamma}\ y,\ 0,\ 0)$, the viscometric functions τ, N_1, and N_2 are given in terms of the stress components τ_{ij}:

$$\tau = \tau_{xy} \tag{2.1a}$$

$$N_1 = \tau_{xx} - \tau_{yy} \tag{2.1b}$$

$$N_2 = \tau_{yy} - \tau_{zz} \tag{2.1c}$$

In the cone and plate geometry, the shear stress τ, the first normal stress difference N_1, the second normal stress difference N_2, and the shear rate $\dot{\gamma}$ are given by (Keentok and Tanner, 1982)

$$\tau = 3M/2\pi R^3 \tag{2.2a}$$

$$N_1 = 2F/\pi R^2 \tag{2.2b}$$

$$N_1 + 2N_2 = \partial \sigma_{\theta\theta} / \partial \ln r \tag{2.2c}$$

$$\dot{\gamma} = \Omega/\beta \tag{2.2d}$$

where M is the torque, R is the radius of the plate, F is the vertical force, Ω is the angular velocity of the cone relative to the plate, $\sigma_{\theta\theta}$ is the pressure measured by flush-mounted pressure transducers located on the plate, and β is the cone angle.

The derivation of these equations requires the following assumptions:

1. Liquid inertia is neglected;
2. The cone angle β is small;
3. The free surface of the liquid is spherical, with radius R; and
4. The surface tension and edge effects are negligible.

In the parallel plate geometry the shear stress, normal stress $N_1 - N_2$, and the shear rate are evaluated at the rim, and the relevant equations are (Macosko, 1994)

$$\tau_R = \frac{M}{2\pi R^3}\left(3 + \frac{d \ln M}{d \ln \dot{\gamma}_R}\right) \tag{2.3a}$$

$$(N_1 - N_2)_R = \frac{F}{\pi R^2}\left(2 + \frac{d \ln F}{d \ln \dot{\gamma}_R}\right) \tag{2.3b}$$

$$\dot{\gamma}_R = \Omega R/h \tag{2.3c}$$

where h is the gap between the plates. The assumptions are

1. The liquid inertia is neglected;
2. The free surface is cylindrical, with radius R; and
3. Edge effects and surface tension are neglected.

The complex dynamic viscosity (η^*), associated with a small amplitude oscillatory shear flow with frequency ω, is defined as

$$\eta^* = \eta' - i\frac{G'}{\omega} \tag{2.4}$$

where η' is the dynamic viscosity and G' the dynamic rigidity. The small amplitude oscillatory shear experiment involves measurement of the unsteady response of a sample that is contained between two planes. In the case of two parallel planes, the upper one of which undergoes small-amplitude sinusoidal oscillations in its own plane with frequency ω, the shear strain between times 0 and t, defined by $\gamma_{yx}(0,t) = \int_0^t \dot{\gamma}_{yx}(t')dt'$, is given as:

$$\gamma_{yx}(0,t) = \gamma^0 \sin \omega\ t$$

The shear rate at time t in the fluid is given by

$$\dot{\gamma}_{yx}(t) = \omega\gamma^0 \cos \omega\ t$$

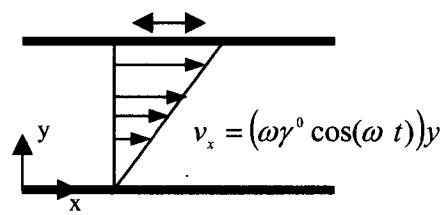

For a purely viscous liquid, stress (τ) is directly proportional to rate of strain ($\dot{\gamma}$), while for a purely elastic solid, stress is directly proportional to strain (γ). Most materials

are viscoelastic, having the properties of both an elastic solid and a viscous liquid. For a viscoelastic material, the most general linear response is represented as

$$\tau_{yx} = \eta'(\omega)\omega\gamma^0 \cos\omega\ t + G'(\omega)\gamma^0 \sin\omega\ t \tag{2.5}$$

i.e.,

$$\tau_{yx} = \eta'(\omega) \times shear\quad rate + G'(\omega) \times shear\quad strain \tag{2.6}$$

All the other possible (linear) descriptions of material behavior can be determined from η' and G' by means of well-defined mathematical procedures. We can conclude from Eq. (2.6) that η' is the measure of the dynamic viscosity of the material and G' the measure of the elastic modulus of the material.

With the same assumptions as outlined earlier for a parallel plate geometry in a small amplitude oscillatory shear flow with frequency ω, the dynamic material functions are

$$\eta' = \frac{M_0 \sin p}{\chi_1} \frac{2h}{\pi R^4 \omega} \tag{2.7a}$$

$$G' = \left(\frac{M_0 \cos p}{\chi_1} + I\omega^2 \right) \frac{2h}{\pi R^4} \tag{2.7b}$$

where M_0 is the amplitude of the applied torque, p is the phase lag of the output displacement waveform behind the input torque, χ_1 is the amplitude of the angular displacement of the fluid, and I is the moment of inertia of the rotating part of the rheometer (= geometry inertia + motor inertia). In the cone-and-plate geometry (Jones *et al.*, 1984)

$$\eta' = \frac{3M_0 \sin p}{2R^3 \pi\omega\chi_1} \beta \tag{2.8a}$$

$$G' = \frac{3\left(\frac{M_0 \cos p}{\chi_1} + I\omega^2\right)}{2\pi R^3}\beta \qquad (2.8b)$$

2.2 SOURCES OF ERROR

1. Edge Effects: Griffiths and Walters (1970) have investigated the importance of edge effects in rheological measurements. They conclude that in rheogoniometric situations with gap angles less than 4°, the state of flow predicted using the infinite cone and plate assumption is valid over most of the flow field, and edge effects give rise to only small errors. The same conclusion is also valid for the parallel plate case. Paddon and Walters (1979) summarize that the edge effects are significantly enhanced by variable viscosity behavior. However, the predicted departure from the constant shear rate normally assumed is still insignificant for the gap angles usually employed in cone-and-plate rheometers ($\leq 4°$). Keentok and Xue (1999) have discussed edge fracture in cone-and-plate and parallel plate flows. It is unlikely to be an important issue in our experiments.
2. Surface Tension and Gravity: The effect of surface tension and gravity on the torque is negligible, but could be significant on the normal forces acting on the plates. Since η' and G' are computed from torque and phase lag, surface tension and gravity are insignificant in the complex dynamic viscosity measurement. Olangunju (1993) has obtained the expressions for various corrections due to surface tension and gravity in parallel plate flow.
3. Fluid Inertia, Secondary Flow and Stability: Extensive work on the effects of fluid inertia in rheometry has been done by Walters (1975), Walters and Waters (1968), and Walters and Kemp (1968a,b). Heuser and Krause (1979), Jones *et al.* (1987),

Olangunju (1993), Olangunju (1997), and Renardy and Olangunju (1998) have discussed the effects of fluid inertia on secondary flow and stability of flow in cone-and-plate and parallel plate rheometers. Jones *et al.* (1987) have shown that inertial effects are very small for both the cone-and-plate and the parallel plate geometries available on controlled stress rheometers. Renardy and Olangunju (1998) have shown that in general, when the cone angle is small, the stability characteristics of the flow do not change much with inertia, indicating that the creeping flow model is indeed a very good approximation in such cases.

2.3 EXPERIMENT

The TA Instruments AR 1000 controlled stress rheometer has a fixed lower plate, while the upper fixture is free to rotate under an applied stress. The upper fixture, which is attached to the draw rod, can either be a plate or a cone. The fixtures are fabricated from stainless steel. A cone of gap angle 2^{o} and radius 20-mm was used to carry out the experiments reported here. Once the initial truncated gap between the cone and the plate is set, which is 45 micron for this case, the computer control system automatically lowers the upper fixture (cone) to the predetermined level. For parallel plates, we set the gap between the plates and the control system automatically lowers the upper plate to this predetermined value. The computer is also used to control the operating temperature. We have used Peltier Plate heating in our experiments. The range of frequencies accessible to this apparatus is from 0.0001 to 100 Hz.

2.3.1 Materials

Low molar mass nematic liquid crystals 5CB (4'-Pentyl-4-biphenylcarbonitrile) and 8CB (4'-Octyl-4-biphenylcarbonitrile) were purchased from Sigma-Aldrich and used

as received. Their molecular formulae are $CH_3(CH_2)_4C_6H_4C_6H_4CN$ and $CH_3(CH_2)_7C_6H_4C_6H_4CN$, respectively. The nematic-isotropic transition temperature was found to be 35 °C for 5CB, and 41 °C for 8CB. Two grades of poly(dimethylsiloxane) 200® fluid were purchased from Sigma-Aldrich and were used without further purification. One grade had a density of 960 kg/m^3 and viscosity 50 mPa-s at 20 °C while the other had a density of 950 kg/m^3 and viscosity 25 mPa-s at 25 °C. These two grades were mixed to obtain a mixture of desired viscosity.

2.3.2 Method

The software rotates the air bearing at a fixed speed, monitoring the torque required to maintain this speed through a full 360° of rotation. Due to the micron tolerances needed to make an air bearing work, any bearing will have some variations in behavior around one revolution in the shaft. These small variations are then stored in the memory of the instrument. This procedure is called mapping. The instrument was mapped each day before loading the sample but after measuring the instrument inertia and geometry inertia. We used precision mapping six times to minimize any oscillation in the torque delivered by the motor. After calibrating the zero gap, the sample was placed on the lower plate. The upper fixture was then lowered to a predetermined value. Edges were trimmed with a spatula to remove any extra material on and around the geometry. The sample was then left at the desired temperature for one-half hour to ensure that temperature was uniform throughout the sample. After this preparation, measurements were made.

2.4 RESULTS and DISCUSSION

The steady shear rheology of low molar mass liquid crystals (*LMMLC*s) has been studied, but small-amplitude oscillatory data are unavailable. There is a summary of LC rheology in Larson (1999), and the most complete study relevant to our work is Gu and Jamieson (1994). The nematic-isotropic transition in 5CB at about 35 °C can be seen in the discontinuity of $G'' = \omega\eta'$ data in Fig. 2.1(a); by controlling the temperature it is possible to obtain the same shear viscosity with both nematic and isotropic phases of 5CB.

Figure 2.1(b) shows G' data for nematic 5CB at 26 °C as a function of frequency. The stresses are well above the resolution level of the instrument. These data are remarkable in that G' is negative. There is a thermodynamic proof that viscosity cannot be negative, but there is no thermodynamic proof that G' cannot be negative. Negative values of G' have been reported in parallel superposition at finite shear rates for solutions of flexible polymers (MacDonald, 1973), and from very limited calculations for simple rheological models they appear to be associated with the energetics of polymer that has been oriented by shear. Negative G' has never, to our knowledge, been observed in a quiescent liquid. It is possible that the nematic alignment, which is present in the 5CB even at rest, plays a role analogous to the structure induced in the flexible polymer by shearing. The available analysis for small-amplitude oscillatory flow of a Leslie-Ericksen fluid, which is the best representation of LMMLC rheology, does not seem to permit negative G', but only a limited range of orientations has been studied [Burghardt (1991); a finite-amplitude solution by Krekhov and coworkers (1993) is not carried through sufficiently to permit evaluation of rheological functions]. The linear viscoelastic

behavior of 5CB or 8CB, or any other liquid crystal with similar viscosity, has never been reported.

Figure 2.2(a) shows G' and G'' of 5CB over two decades of frequency at 26 °C, which is in the nematic regime. For all practical purposes, G' is zero in this range, while G'' is linear in ω. This means that 5CB is a Newtonian viscous fluid in this frequency range with a constant viscosity of 0.03 Pa-s. Figure 2.2(b) is the strain sweep experiment of 5CB at 1 rad/s while ascending and descending in strain. This shows that 5CB is, indeed, a linear material over a wide range of strain with no elasticity. G' is practically zero at all strains. However, a peak in G'' is pronounced at smaller strains. We have observed this peak both while ascending strain and descending in strain. This peak is unusual. We may recall that in a frequency sweep experiment at a constant torque, strains are higher towards lower frequencies and lower towards higher frequencies. We have observed negative G' at higher frequencies in Fig. 2.1(b), which corresponds to smaller strains. A likely explanation of this unexpected behavior is that our measurements have been done on a controlled stress rheometer that might have inaccuracies when measuring small strains.

5CB and 8CB are the members of same homologous series of liquid crystals, but 5CB is an "aligning" liquid crystal while 8CB is a "tumbling" liquid crystal. Figure 2.3 (a) is a plot of the magnitude of the complex viscosity of 8CB at 35 °C (in its nematic phase) as a function of angular velocity. All experiments (frequency sweep experiments) for this plot have been obtained by decreasing frequency from 60 rad/s to 0.1 rad/s. A strain sweep experiment confirmed that we are in a linear regime at 50 $\mu N - m$ torque and away from excessive signal noise regime. All data agree well at low frequencies, but

at higher frequencies there is large variation. All the curves in this plot are very unusual above the angular frequency of 1 rad/s. This behavior might be due to the liquid crystallinity of 8CB, but it is more likely to be an instrument artifact. To investigate the second possibility, we have done a series of experiments with a mixture of PDMS oils. The two PDMS oils have been mixed in such a way to make the viscosity of the final mixture close to the viscosity of 8CB. The two grades of PDMS oils that have been used are completely miscible. Figure 2.3 (b) is the plot of the magnitude of the complex viscosity of a PDMS mixture, containing 67.25% by mass of 20 cSt PDMS, at precisely the same conditions as the experiment in Fig. 2.3(a). There is a gradual rise in the viscosity of this mixture beyond 10 rad/s, which is not acceptable. This makes us believe that there may be some instrument artifact. As discussed subsequently, one possible explanation of this phenomenon is that this is an inertial effect that is not compensated for adequately in the instrument software.

Figure 2.4(a) shows G' and G'' of this PDMS mixture at two different torques, measured on two different days. While G'' remains unaltered, there is a drastic change in G'. At one torque (50 $\mu N-m$), G' is positive during the entire course of experiment, while it is negative at another torque (500 $\mu N-m$). A strain sweep experiment has confirmed that both of these operating torques are well within the linear viscoelastic regime. Nothing unusual happens in the steady shear experiment; over three decades of shear rate (Fig. 2.4(b)), the viscosity behaves in the expected manner.

This strange behavior of 5CB (negative G') and 8CB (unusual $|\eta^*|$ variation), together with the measurement on the PDMS mixture (rising $|\eta^*|$, negative G'), suggest that there might be something wrong with the software of the rheometer. Hence, it is

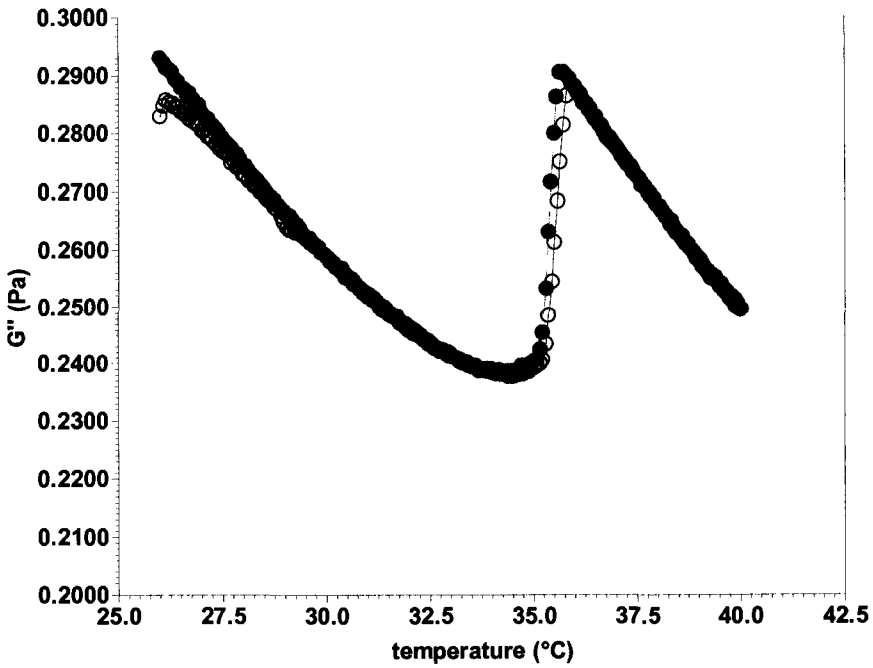

(a) G'' of 5CB as a function of temperature, ω = 10 rad/s and torque = 500 μN-m. Open circles (o) are while increasing temperature and closed circles (•) are during decreasing temperature

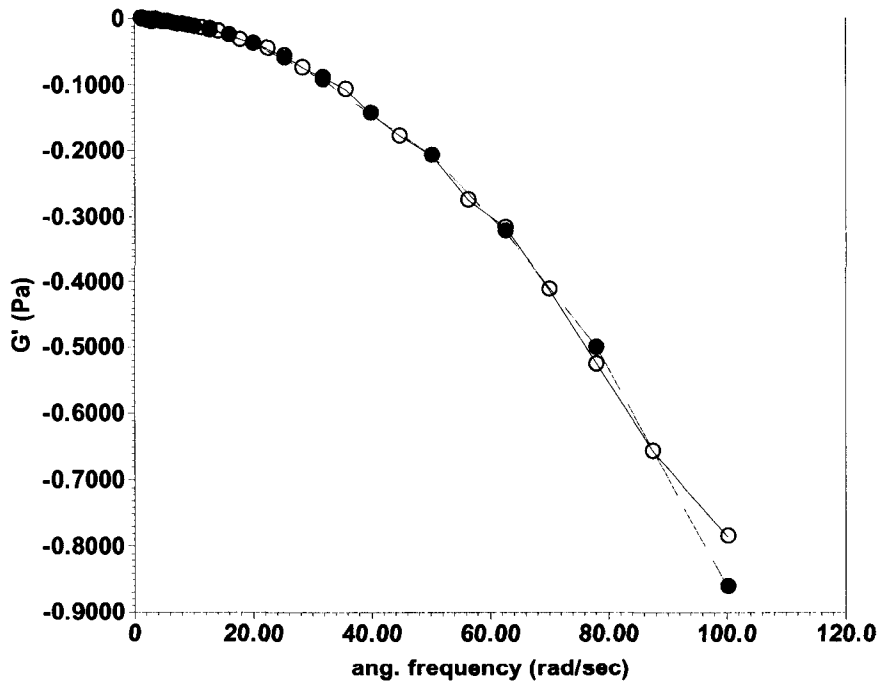

(b) G' of 5CB as a function of frequency, T = 26 °C and torque = 500 μN-m. Open circles (o) are while increasing frequency and closed circles (•) are during decreasing frequency

Fig 2.1: G' and G'' of 5CB

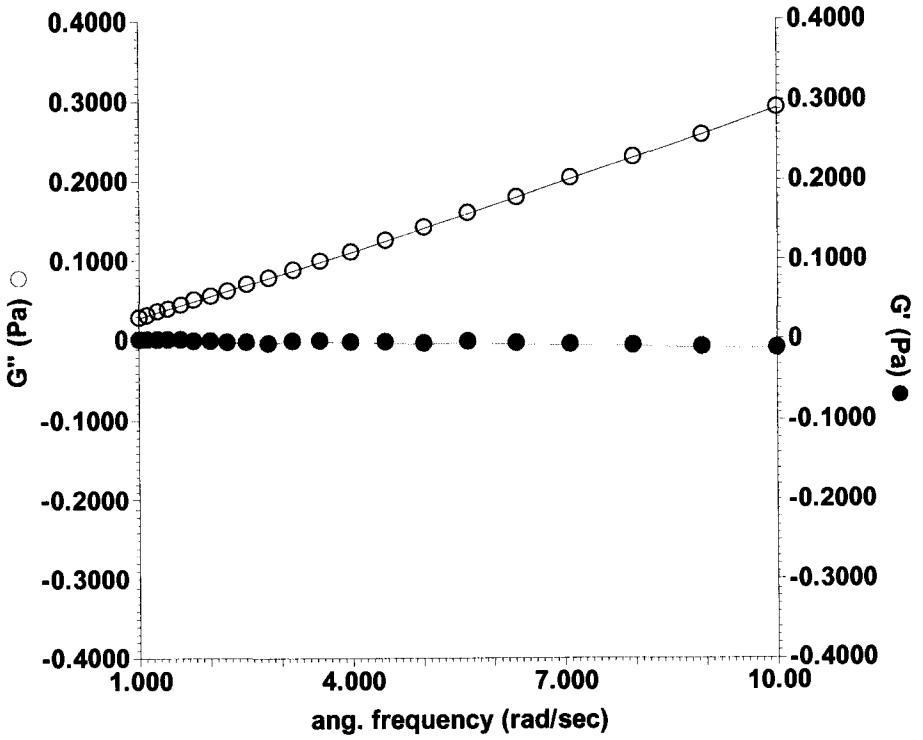

(a) G' and G'' of 5CB as a function of ω, 26 °C, 500 $\mu N - m$

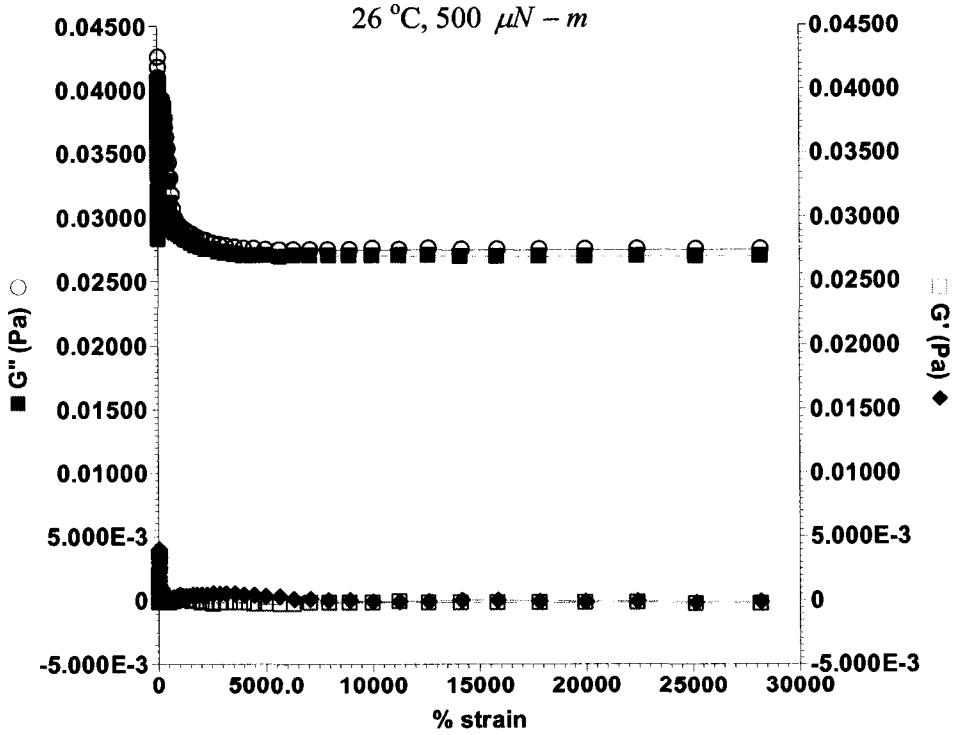

(b) G' and G'' of 5CB as a function of % strain at 26 °C, ω = 1 rad/s while increasing strain (o, ♦) and decreasing strain (■,□)

Fig 2.2: 5CB in frequency sweep and strain sweep experiments

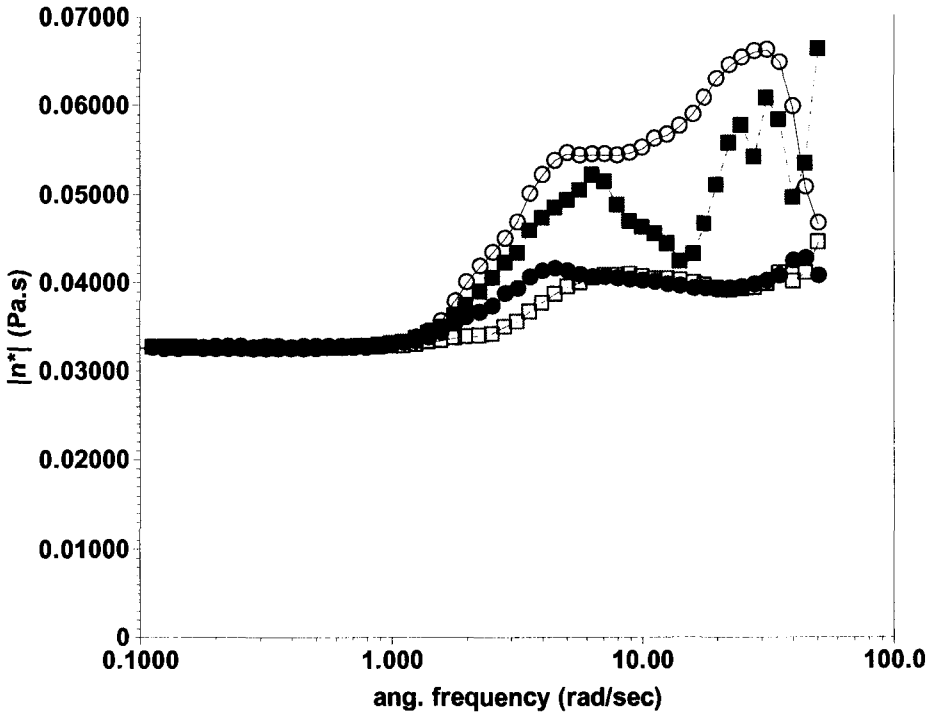

(a) 8CB at 35 °C, torque = 50 $\mu N - m$; after equilibration (o), after preshear (•), after rest (■), and immediately after the preceding experiment. (□).

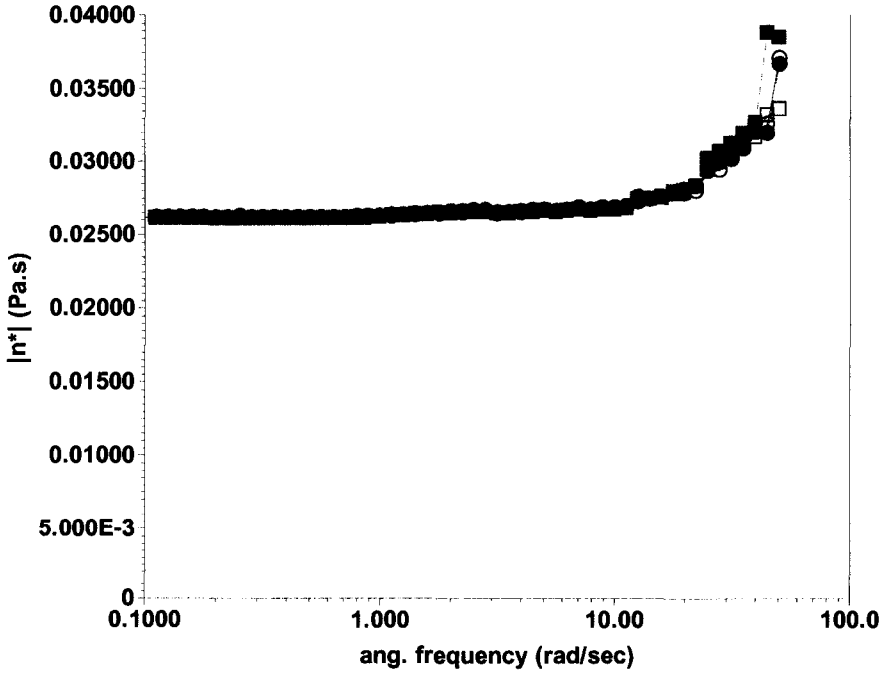

(b) A PDMS mixture at 35 °C, torque = 50 $\mu N - m$; legends identical to figure (a).

Fig 2.3: $|\eta^*|$ of 8CB and a PDMS mixture.

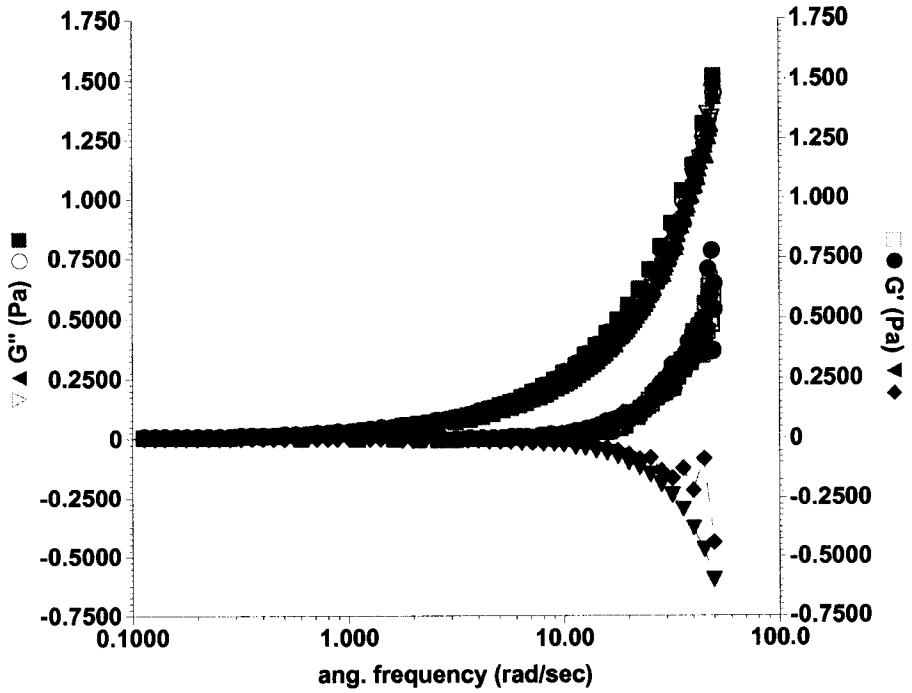

(a) A PDMS mixture in oscillatory experiment at two different torques. While G'' (uppermost curve) remains same at both the torques, G' is positive at 50 $\mu N-m$ (●,□), but negative at 500 $\mu N-m$ (♦,▼)

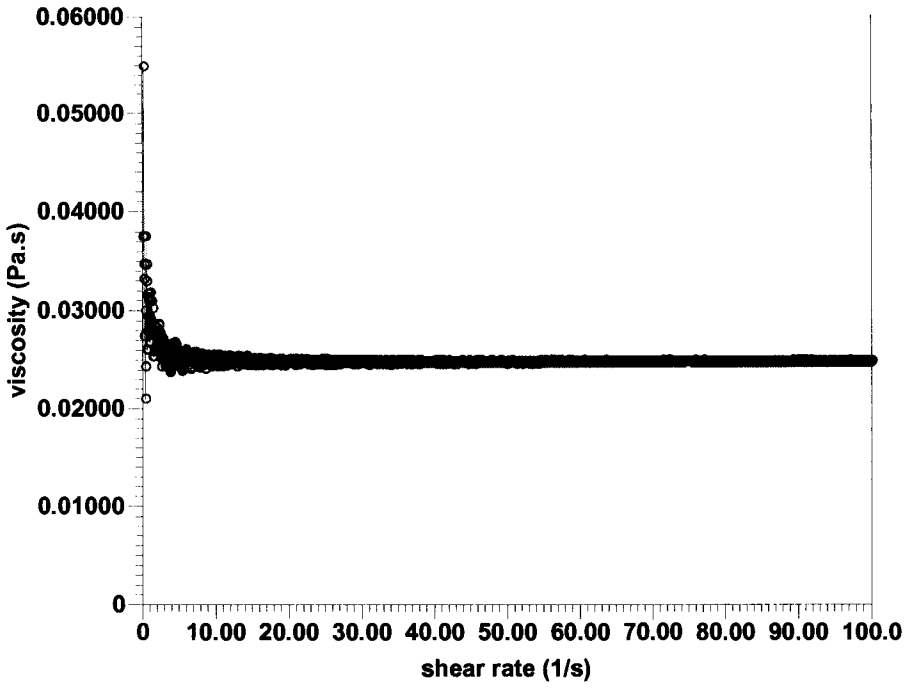

(b) The PDMS mixture in steady shear experiment

Fig 2.4: The PDMS mixture in dynamic and steady mode at 35 °C

necessary to investigate the theory for the rheometry. Appendix A describes the theory for linear viscoelastic measurements on a controlled stress rheometer using a cone-and-plate geometry.

2.5 Comparison with Theory

Most of the theories assume that the material is highly viscous, and hence inertial forces can be safely neglected. This assumption is true for viscous polymer melts, such as the liquid crystalline polyester Vectra-A ($|\eta^*| \approx 10^4$ Pas), but it is certainly not true for 5CB or 8CB, or for any other material with a viscosity of the order of 25-30 mPas. The Reynolds number based on the cone radius ($\beta R^2 \Omega \rho / |\eta^*|$) for the PDMS mixture is roughly 25, which is substantially greater than unity. The solution of the equation of motion for the cone-and-plate geometry with finite fluid inertia is given by Walters (1963) and Maude and Walters (1964), and is represented in Eq. (A4).

The base solution ($\rho = 0$) for the cone and plate geometry is derived in Eq. (A18):

$$\eta' = \frac{M_0 \sin p}{59.94 w \chi_1 R^3}, \tag{2.9a}$$

$$G' = \frac{\dfrac{M_0 \cos p}{\chi_1} + I\omega^2}{59.94 R^3} \tag{2.9b}$$

2.5.1 First Order Inertial correction: With a first order inertial correction to the base solution, η' and G' are expressed as

$$\eta' = \frac{M_0 \sin p}{59.94 w \chi_1 R^3}, \tag{2.10a}$$

$$G' = \frac{\dfrac{M_0 \cos p}{\chi_1} + I\omega^2}{59.94 R^3} + 2.437 \times 10^{-4} \rho \omega^2 R^2 \tag{2.10b}$$

as derived in Appendix A in Eq. (A19).

We have also derived a second order inertial correction to η' and G'. Before presenting the second order correction in inertia, let us see how our first order correction, Eq. (2.10), applies to the data in Figs. 2.1(b), 2.3(a), 2.3(b) and 2.4(a).

In order to use Eq. (2.10), we need torque (M_0), phase lag (p), amplitude of angular displacement of the fluid (χ_1), and angular velocity (ω) for each data point. I, ρ, and R are constants. In these experiments we have kept torque constant. All the experiments discussed here are frequency sweep experiments. This leaves us with two measured variables, p and χ_1. We have used p and χ_1 as measured by the instrument for each ω in the calculations.

Figure 2.5 compares the measured G' of 5CB with the prediction of Eq. (2.10b). The agreement is generally good, except at a few points towards the higher frequencies. The open circles (o) of Fig. 2.1(b) are open circles (o) here also. The closed diamonds (♦) are the predictions of Eq. (2.10b). It seems that the discrepancies in a few data points are because of the smoothing of data by the instrument.

Figure 2.6 shows the magnitude of the complex viscosity of 8CB plotted along with the theoretical prediction of Eq. (2.10). The experimental data points are open circles (o) of Fig. 2.3(a), plotted here also as open circles (o). The closed diamonds (♦) are predictions of Eq. (2.10). The agreement is excellent at all frequencies.

Figure 2.7 shows the magnitude of complex viscosity of PDMS as open circles (o) from Fig. 2.3(b) compared with the prediction of Eq. (2.10). The closed diamonds (♦) are predictions of Eq. (2.10b). The agreement is very good in the entire frequency range.

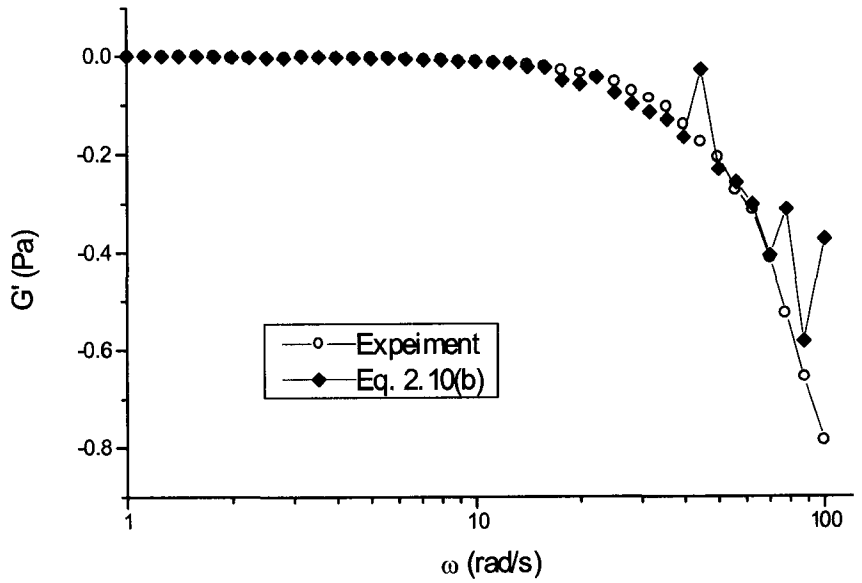

Fig 2.5: G' of 5CB: Open circles (o) of Fig. 2.1(b) against theoretical prediction of Eq. 2.10(b) as closed diamonds (♦).

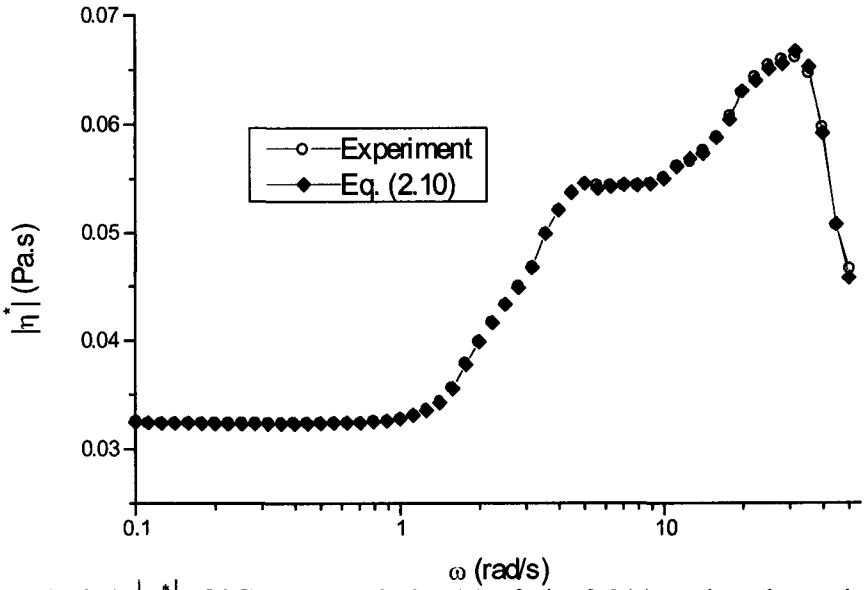

Fig 2.6: $|\eta^*|$ of 8CB: Open circles (o) of Fig. 2.3(a) against theoretical prediction of Eq. 2.10 as closed diamonds (♦).

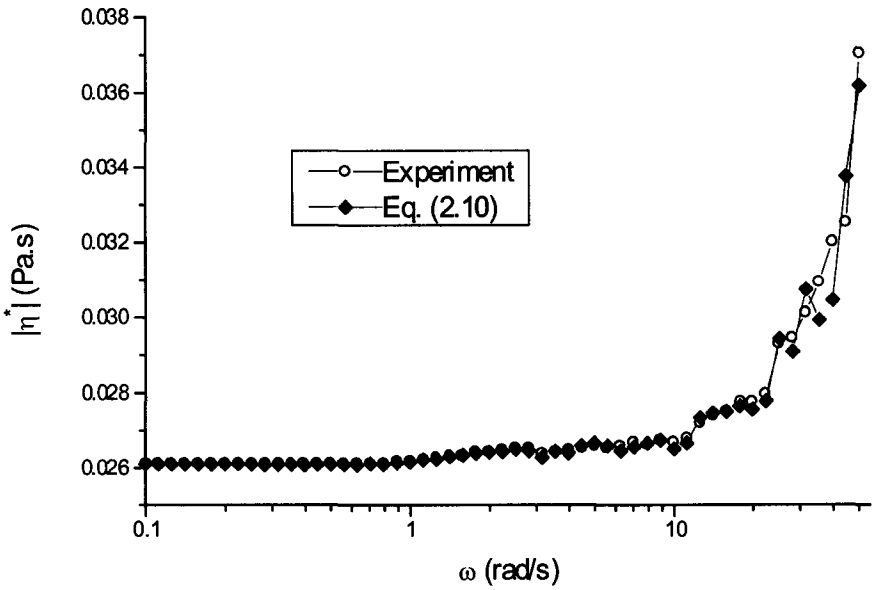

Fig 2.7: $|\eta^*|$ of the PDMS mixture: Open circles (o) of Fig. 2.3(b) against theoretical prediction of Eq. 2.10 as closed diamonds (♦).

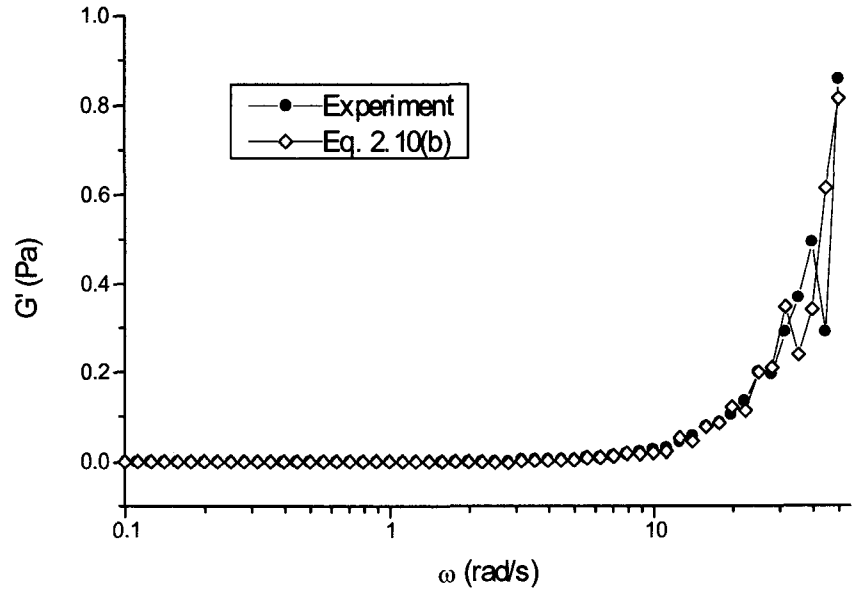

Fig 2.8(a): G' of the PDMS mixture: Closed circles (•) of Fig. 2.4(a) against theoretical prediction of Eq. 2.10(b) as open diamonds (◊).

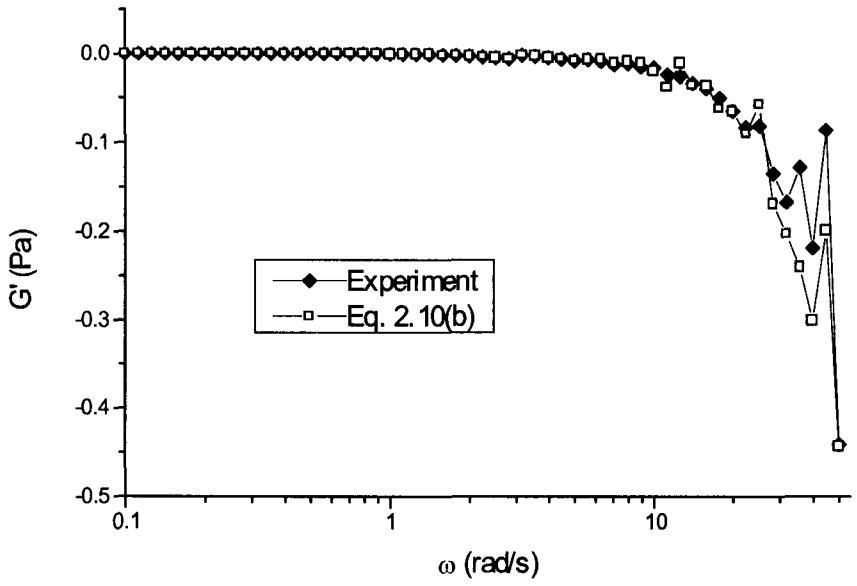

Fig 2.8(b): G' of the PDMS mixture: Closed diamonds (♦) of Fig. 2.4(a) against theoretical prediction of Eq. 2.10(b) as open rectangles (□).

Figures 2.8(a) and 2.8(b) show G' of PDMS of Fig. 2.5(a) compared with the prediction of Eq. (2.10b). The closed circles (•) and closed diamonds (♦) are from Fig. 2.5(b). The open diamonds (◊) and open rectangles (□) are predictions of Eq. (2.10b). The theoretical prediction of Eq. (2.10b) accurately captures the behavior of G'. The positive and negative variations of G' have been clearly and accurately predicted by Eq. (2.10b).

Figures 2.5 to 2.8 demonstrate that the instrument software is making the inertial correction up to the first order, and the form of this inertial correction is the same as that in Eq (2.10). However, this very close agreement of experimental data with Eq. (2.10) does not resolve our initial concerns about the unusual G' and $|\eta^*|$ behavior. Therefore, we will evaluate the second order inertial correction.

2.5.2 Second Order Inertial correction: Using Eqs. (A8), (A10) and (A17):

$$M_0 e^{ip} + I\omega^2\chi_1 = 59.94\mathrm{R}^3\eta^* i\omega\chi_1 - 0.01461\rho\omega^2 R^5\chi_1 + i8.508\times10^{-7}\frac{\rho^2\omega^3 R^7\chi_1}{\eta^*} \qquad (2.11)$$

where $\eta^* = \eta' - i\dfrac{G'}{\omega}$.

It is not easy to solve Eq. (2.11) for η' and G' explicitly because of the presence of η^* in both the numerator and the denominator. We can either write a code to solve Eq. (2.11) for η' and G' at each data point, or we can simply use Newton's iteration scheme, where the base solution will provide the initial guesses. With the second approach, it is straightforward to evaluate the iteration scheme for η' and G' from Eq. (2.11) as follows:

$$\eta'_{i+1} = \frac{M_0 \sin p}{59.94 w\chi_1 R^3} - 1.42\times10^{-8}\frac{\rho^2\omega^2 R^4\eta'_i}{(\eta'_i)^2 + (G'_i/\omega)^2}, \qquad (2.12a)$$

$$G'_{i+1} = \frac{\dfrac{M_0 \cos p}{\chi_1} + I\omega^2}{59.94R^3} + 2.437\times10^{-4}\,\rho\omega^2R^2 + 1.42\times10^{-8}\,\frac{\rho^2\omega^2R^4G'_i}{(\eta'_i)^2 + (G'_i/\omega)^2} \qquad (2.12b)$$

The second order correction is too small to provide any significant contribution to the solution. A rough estimate of the second order correction in η' for 5CB at 100 rad/s is

$$\frac{1.42\times10^{-8}\times(1000)^2\times(100)^2\times(0.02)^4\times0.03958}{(0.03958)^2+(-0.7851)^2} = 1.45\times10^{-6},$$

which is far smaller than $\eta' = 0.03958$. In the same way, a rough estimate of the second order correction for G' is

$$\frac{1.42\times10^{-8}\times(1000)^2\times(100)^2\times(0.02)^4\times(-0.7851)}{(0.03958)^2+(-0.7851)^2} = -2.89\times10^{-5}$$

which is not only much smaller that $G' = -0.07851$, but is also negative. That means the second order correction makes a negative G' more negative. All the numbers used here for calculations are in SI units and are from an actual data point for 5CB at 100 rad/s.

2.6 EFFECT OF THE MOMENT OF INERTIA OF THE ROTOR

In last section we showed that inadequate compensation for fluid inertia in the rheometer software is not an explanation for the observed anomaly in the experimental data. Since the moment of inertia of the rotor, I, is post multiplied by ω^2 in its only appearance in the expression for G', we expect that the G' measurement will be highly sensitive to the estimated moment of inertia of the rotor, especially at higher frequencies. We have investigated the effect of I in the G' calculation by varying it slightly in either direction. Changing it by even one percent drastically affects the results. Figure 2.9 shows the effect of I in the G' calculation. In Fig. 2.9(a), decreasing I by 0.73% brings

all positive G' data points to come zero, while all the data points close to zero remain zero. Increasing I by 0.24% in Fig. 2.9(b) makes all the data points positive.

2.7 MEASUREMENT ON A CONTROLLED-STRAIN RHEOMETER

We repeated some of our experiments on a Rheometrics Fluid Spectrometer RFS II at ExxonMobil Research and Engineering Co., Annandale, NJ. This instrument is a controlled strain rheometer. We used a couette geometry with a bob diameter of 16.52 mm, a bob length of 13.1 mm, and a cup diameter of 17.02 mm.

In Fig. 2.10 we show the frequency sweep experiment of 5CB at 250% strain. This strain seems to be a bit high, but it lies well within the linear viscoelastic regime of 5CB as confirmed by a strain sweep experiment. Such a high strain is necessary to make the torque level large enough to be within the transducer's resolution limit. While we had observed negative G' in Fig. 2.1(b), no such behavior is observed here. Here G' is positive for all the frequencies. We do not attach much significance to these G' numbers, and regard G' to be essentially zero at all frequencies for all practical purposes. This is because the phase angle is close to 90^{o} at all frequencies, and the G' measurement is subject to large noise when the phase angle is close to 90^{o}. In this experiment G'' is linear in ω with a constant slope, giving a viscosity of 0.03 Pa-s.

Figure 2.11 shows the magnitude of complex viscosity of 8CB at 34.6 ($\pm$ 0.1 ^{o}C) as a function of angular velocity. This experiment has been done at a strain of 200%. Unlike Fig. 2.3(a), where we had observed an abnormal rise in the magnitude of the complex viscosity at a frequency of about 2 rad/s, we have not observed any unusual behavior in this measurement. The viscosity shown in Fig. 2.11 is slightly higher than the

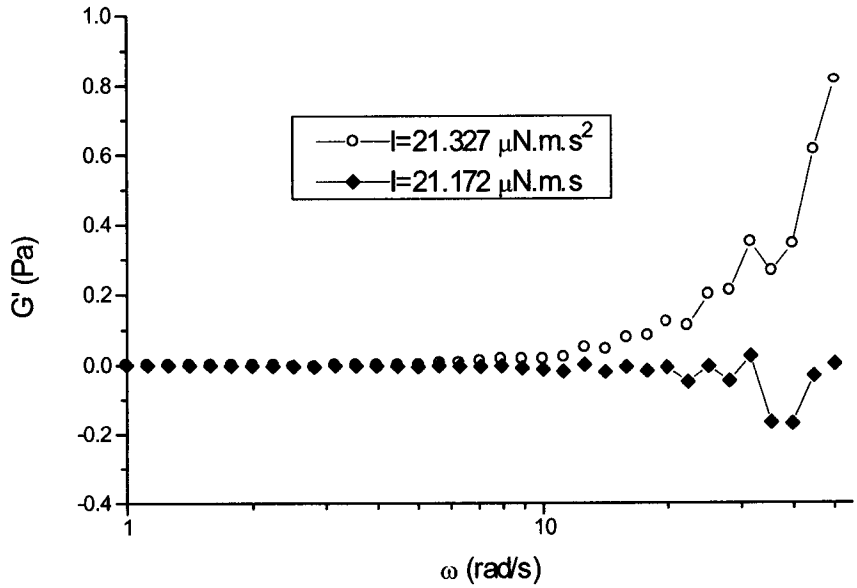

(a) G' of PDMS: Open circles (o) with $I = 21.327 \times 10^{-6}$ Nms^2, and closed diamonds (♦) assuming $I = 21.172 \times 10^{-6}$ Nms^2

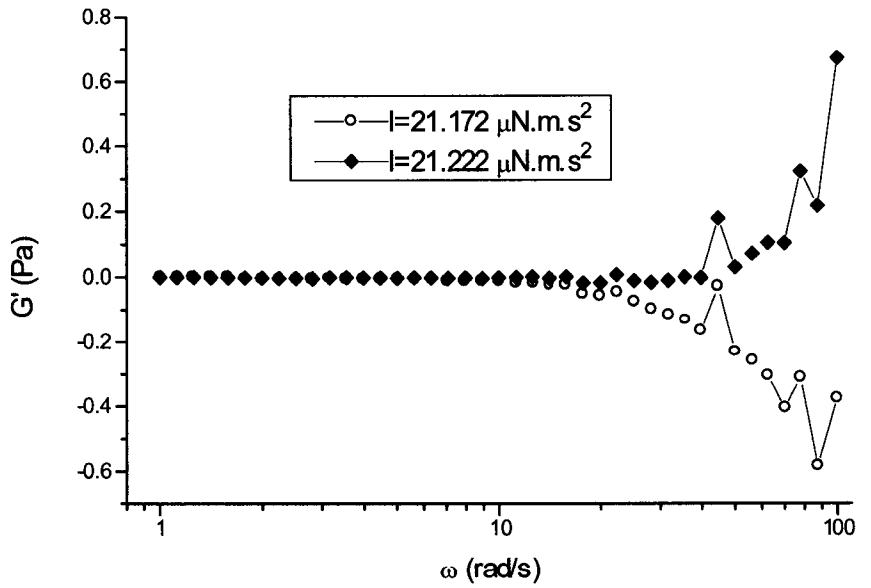

(b) G' of 5CB: Open circles (o) with $I = 21.172 \times 10^{-6}$ Nms^2, and closed diamonds (♦) assuming $I = 21.222 \times 10^{-6}$ Nms^2

Fig 2.9: Effect of I on G'

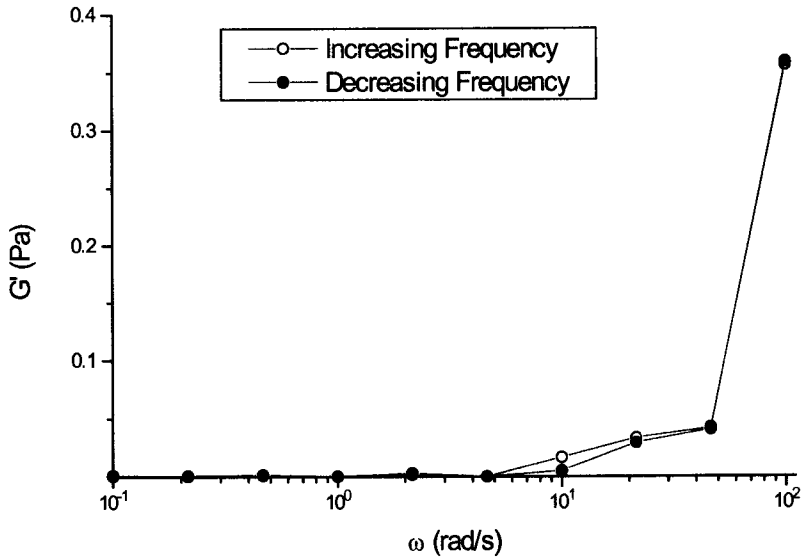

Fig 2.10: G' of 5CB as a function of frequency, T = 26 °C and 250% strain. Open circles (o) are while increasing frequency and closed circles (•) are during decreasing frequency

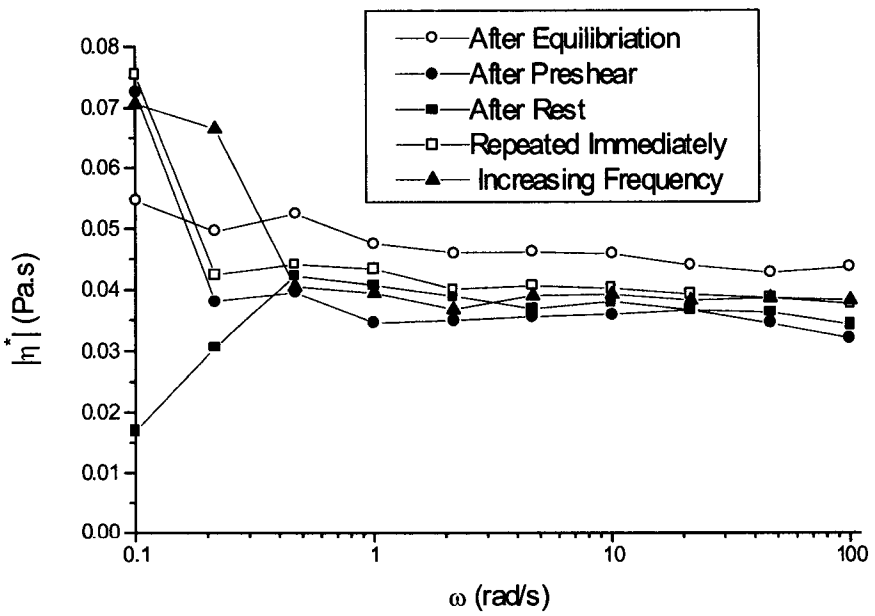

Fig 2.11: 8CB at 200% strain and 34.6 (± 0.1) °C

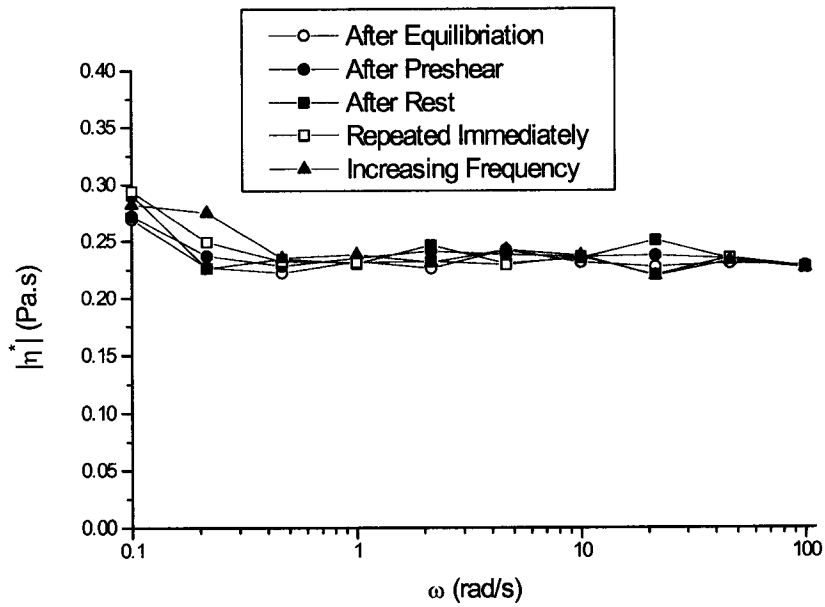

Fig 2.12: PDMS at 200% strain and 34.6 (± 0.1) °C

viscosity shown in Fig. 2.3(a). This is because the temperature is slightly lower in the experiment of Fig. 2.11, and a small temperature change can potentially cause a large change in viscosity, especially near the smectic-nematic transition temperature. G'' is linear in ω in this experiment, with the slope changing slightly from data set to data set, depending on preconditioning of the sample. The elastic modulus is zero at all frequencies in all data sets. Hence, 8CB is purely viscous in this frequency range.

Figure 2.12 shows the magnitude of the complex viscosity of a PDMS mixture at 34.6 (± 0.1 °C) as a function of angular velocity. This experiment has been done at a strain of 200%. The viscosity remains constant, independent of preconditioning. Unlike Fig. 2.3(b), no unusual behavior is observed here. G' is zero at all frequencies.

2.8 CONCLUSION

The main conclusions of this chapter are:

1. Steady shear experiments produce acceptable results for the entire shear rate range studied. The results for 5CB are consistent with those of Gu and Jamieson (1994). Oscillations in the measured viscosity are large at low shear rates but smaller at higher shear rates. We have also produced consistent and acceptable results for 8CB and low viscosity PDMS and PDMS mixtures in steady shear experiments.
2. The nematic to isotropic transition temperatures of 5CB and 8CB are confirmed in temperature sweep experiments.
3. Above an angular speed of 10 rad/s we observe unusual behavior for 5CB, 8CB and a PDMS mixture of similar viscosity. The unusual behavior includes, but is not limited to, the observation of negative G'. This result appears to be an experimental artifact.

4. The first order inertial correction applied to the raw data reproduces the experimental measurements. This means that instrument software is performing acceptably. The second order inertial correction is too small to have any effect.
5. The measurement is very sensitive to the estimate of the moment of inertia of the rotating part.
6. Problems with the experimental measurements arise when the raw phase lag is about 3 radians or more, which suggests the possibility of an error in measuring the angular displacement under such conditions.

Chapter 3
INTERFACIAL TENSION OF LIQUID CRYSTALLINE DROPLETS

Dispersions of liquid crystalline droplets in an amorphous liquid matrix are of interest in a variety of applications. Dispersions of low-molar mass liquid crystals are employed in display technology. Polymeric liquid crystalline dispersions may serve as precursors for the formation of polymer-polymer composites. The processing of such dispersions is dependent on the interfacial tension as well as the physical properties of the two phases.

The interfacial tension at the interface between a gas phase and an isotropic liquid, or between two isotropic liquids, is usually a monotonically decreasing function of temperature (Adamson and Gast, 1997). The decrease in interfacial tension with temperature is usually attributed to an excess in disorder at the interface relative to the bulk. Little is known, however, about the temperature dependence of the interfacial tension between a liquid crystal and a chemically dissimilar isotropic liquid. Some measurements exist of the temperature dependence of the surface tension at an air interface of two common low-molar mass biphenylcarbonitriles, 4'-pentyl-4-biphenylcarbonitrile (*5CB*) and 4'-octyl-4-biphenylcarbonitrile (*8CB*), both of which undergo sharp nematic-isotropic (*N-I*) transitions. (8CB also undergoes a transition from a smetic-A phase to a nematic.) Gannon and Faber (1978) measured the surface tension of 5CB and 8CB using the Wilhelmy plate method and found that the surface tension increases with increasing temperature throughout the nematic regime, with an apparent discontinuity at the N-I transition (T_{NI}); they observed a further increase for a few degrees into the isotropic regime, after which the surface tension declines. Pendant drop measurements by Krishnaswamy (1980) on 5CB show the same behavior. Song and

Springer (1997), however, found with the pendant drop method that the surface tension of 5CB decreases with temperature, with a discontinuity at T_{NI}; they did observe an increase in surface tension with increasing temperature in the neighborhood of the N-I transition for other low-molar mass liquid crystals. Tintaru *et al.* (2001), also using a pendant drop method, showed a decreasing dependence of the surface tension on temperature for 5CB both before and after the N-I transition, with a possible very small increase for a few mK just beyond T_{NI}; they found that the surface tension of 8CB was relatively insensitive to temperature, with a small positive slope just prior to T_{NI} and for several degrees thereafter. Wu and Mather (2002), using the thread breakup method, observed a stepwise increase in the interfacial tension between a thermotropic liquid crystalline polymer and polydimethylsiloxane when passing through the N-I transition.

Li and Denn (2002) carried out Monte Carlo calculations of the interfacial tension between a nematic liquid crystalline polymer and a flexible polymer. They found that the interfacial tension is a decreasing function of temperature and an increasing function of the nematic order parameter when the orientation of the nematic phase is parallel to the interface. For an orthogonal (*homeotropic*) orientation they found that the interfacial tension is a decreasing function of both temperature and nematic order parameter. The order parameter undergoes a rapid decrease over a narrow temperature range as the N-I transition is approached from below; hence, the interfacial tension for a polymeric nematic would be expected to decrease near the N-I transition with increasing temperature for a parallel orientation relative to the interface and to increase with increasing temperature for a homeotropic orientation.

3.1 EXPERIMENT

3.1.1 Materials

4'-pentyl-4-biphenylcarbonitrile (5CB) and 4'-octyl-4-biphenylcarbonitrile (8CB) were purchased from Sigma-Aldrich and used as received. 5CB undergoes a crystal-nematic transition at 21 °C and a nematic-isotropic transition at 35 °C; the apparent first-order N-I transition can be seen in Fig. 3.1, which is a plot of the dissipative portion of the complex viscosity (essentially the shear viscosity, since the storage modulus of 5CB is negligible) as a function of temperature, as measured in a TA1000 stress-controlled rheometer. Note that the viscosity increases with temperature in passing from the nematic to the isotropic. The transition is also observed optically in a polarizing microscopic. 8CB undergoes a crystal-smectic-A transition at 22.5 °C, a relatively broad apparent second-order smectic-nematic (*S-N*) transition between 32° and 34 °C, and a N-I transition at 41 °C; the N-I transition can be seen in the viscosity plot in Fig. 3.2, while the S-N transition is shown in the insert.

The suspending fluid was Polydimethylsiloxane 200® fluid (*PDMS*), which was purchased from Sigma-Aldrich and used without further purification. The molecular weight of the PDMS, which is a Newtonian liquid, is about 2500.

3.1.2 Pendant Droplet Method

Interfacial tensions were measured using pendant drop tensiometry enhanced by video-image digitization. A schematic of the experimental set up is shown in Fig. 3.3. The detailed experimental design is described in Lin *et al.* (1990). The technique is based on the analysis of the shape of a pendant droplet of one liquid, formed at and tethered to a needle tip, and immersed in a second immiscible liquid located in a transparent curvette.

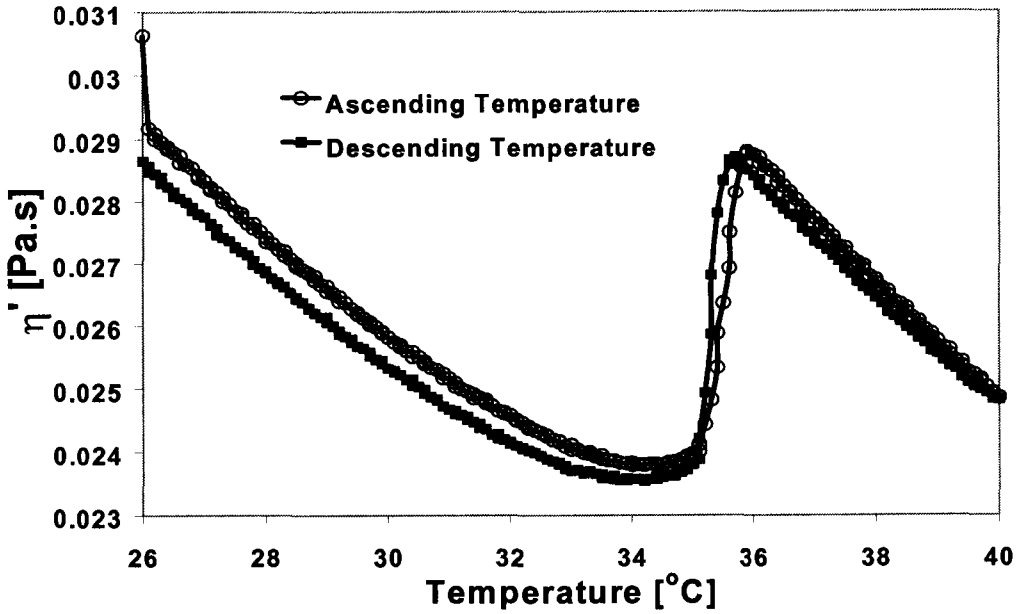

Fig 3.1: Dissipative portion of complex viscosity of 5CB as a function of temperature.

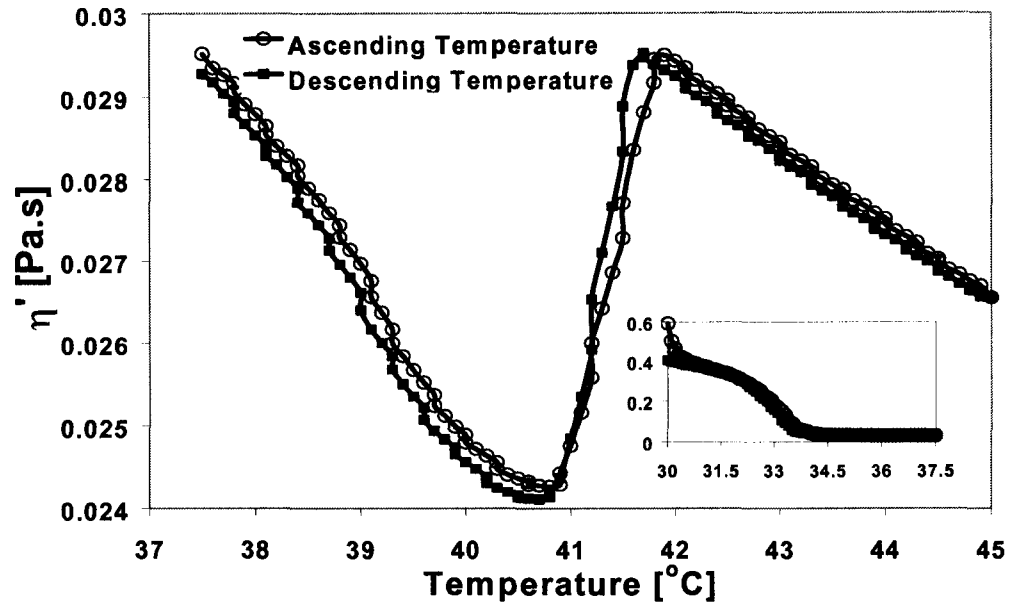

Fig 3.2: Dissipative portion of complex viscosity of 8CB as a function of temperature. The insert shows the neighborhood of the smectic-nematic transition.

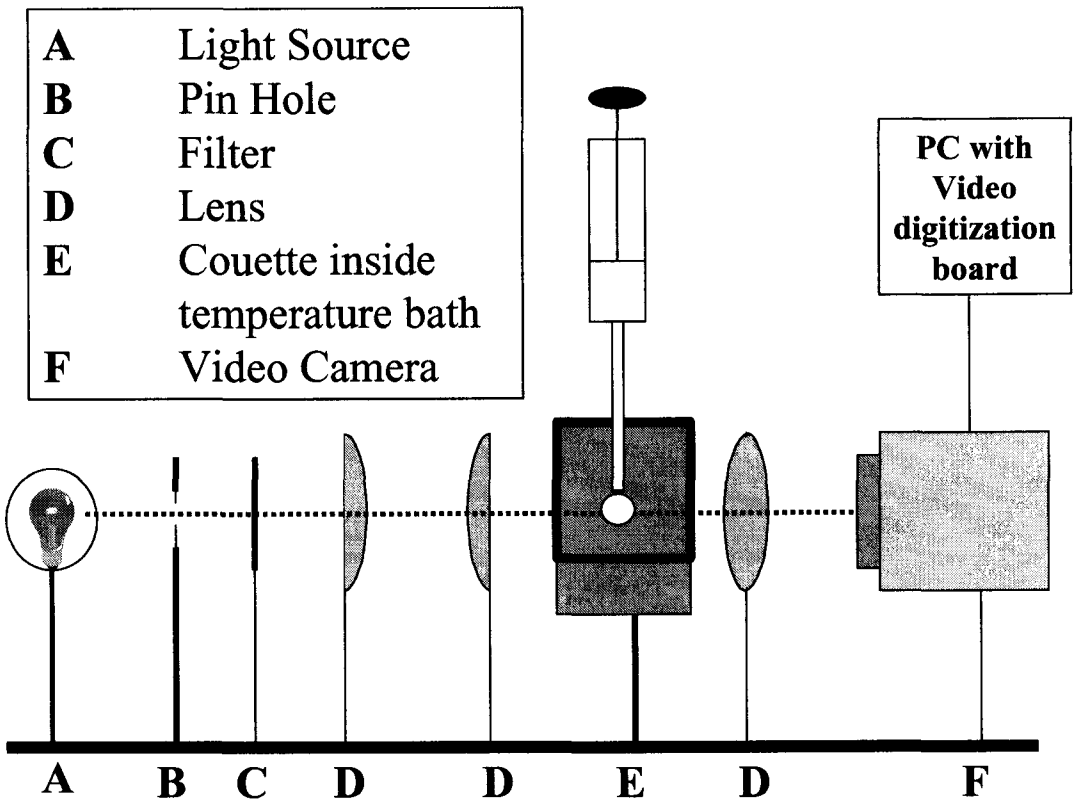

Fig 3.3: Schematic of the Pendant Droplet Tensiometer

Collimated light is passed across the immersed droplet, forming a silhouette of the drop shape that is then imaged onto the active area of a video camera. An edge detection technique is used to construct a numerical locus of the drop shape from digital images of the silhouette. The drop shape is simulated by nondimensional solution of the Young-Laplace equation, which gives the nondimensional interfacial shape (scaled by R_o, the radius of curvature at the drop apex) as a function of the Bond number, $\frac{\Delta\rho g R_o^2}{\gamma}$, where $\Delta\rho$ is the density difference between the two liquids, g is the acceleration due to gravity, and γ is the interfacial tension. The nondimensional simulations are fit to the experimental loci by a least squares minimization, which results in values for the radius of curvature at the apex and the Bond number. The interfacial tension is then determined from the knowledge of the density difference at the temperature of measurement, the Bond number, and the radius of curvature at the apex.

It is important to note that the pendant drop technique is most accurate when the magnitudes of gravitational and surface tension forces are balanced such that the drop contour exhibits a "waist" before attaching to the needle tip; this occurs for Bond numbers smaller than approximately 0.6. There is no waist in the profile for values of the Bond number greater than 0.6, the amount of fluid attached to the needle tip is small, and the fitting is inaccurate. The shape is too spherical, however, for values of the Bond number smaller than approximately 0.1, and the fit is not sensitive to the Bond number. In practice, it has been found for air bubbles in surfactant solutions with surface tensions in the range of approximately 30-70 mN/m that the smallest values of the least squares error are achieved for Bond numbers in the range 0.1 - 0.3. An estimate of the error in the interfacial tension measurement for this range of Bond numbers by Lin *et al.* (1994,

1995) showed an accuracy of better than one percent in the tension measurement, assuming that the density is known exactly. Although the measured interfacial tensions in our experiments are low (2 - 7 mN/m), the density difference is also small, and values of Bond numbers were in the range 0.1 - 0.3, as in the case of air bubbles in water. Hence, the error estimates of Lin *et al.* (1994, 1995) should be applicable. As noted below, however, the probable uncertainty of the density differences is of order 5%, hence we expect about 5% accuracy in the interfacial tension measurements.

In this application of the pendant drop technique, the PDMS was filled into a curvette that was placed in a closed environmental chamber; the chamber is equipped with opposing windows to allow light to pass through, and channels to allow thermostated circulating water to maintain a constant temperature in the chamber. The temperature of the PDMS in the curvette was monitored directly by means of a thermometer (accuracy 0.1°C) placed through a septum into the chamber. A stainless steel 22 gauge needle was inserted through a second septum into the chamber and submerged in the PDMS. The needle was connected to a syringe containing the biphenylcarbonitrile. By depressing the plunger of the syringe, a drop of biphenylcarbonitrile of approximately 2 mm diameter was formed at the tip of the needle. The drop was equilibrated with the surrounding PDMS fluid at the thermostated temperature for one hour before measurements were undertaken. Three different droplets were analyzed at each temperature.

3.1.3 Density Difference

Pendant drop tensiometry requires precise determination of the density difference between the two phases. The temperature dependence of the density of PDMS is provided

by the manufacturer: the density is 960 kg/m^3 at 25 ^{o}C, and the coefficient of volumetric expansion is 0.00104 K^{-1}. The temperature dependence of the density of 5CB has been reported by Gannon and Faber (1978) and by Tintaru *et al.* (2001), and the temperature dependence of the density of 8CB by Tintaru *et al.* (2001) The two reported density measurements for 5CB differ by about 2%; since the densities of 5CB and PDMS are similar, this variation leads to an uncertainty of about 50% in the estimate of the density difference.

We measured the density difference between 5CB and PDMS directly as a function of temperature by measuring the rate of fall of a spherical droplet of 5CB in PDMS, as discussed in the Appendix B. The uncertainty in this measurement is of order 5%. 8CB did not form a spherical droplet in PDMS, and we were unable to measure $\Delta\rho$ directly.

3.2 RESULTS and DISCUSSION

The interfacial tension for the 5CB/PDMS interface is shown as a function of temperature in Fig. 3.4. The solid line passes through the average of three pendant droplet measurements using the measured density difference, as described in the Appendix B. The upper dashed line is computed using the density of 5CB as reported by Tintaru *et al.* (2001), while the lower dotted line is computed using the density data of Gannon and Faber (1978). The interfacial tension for the 8CB/PDMS interface is shown in Fig. 3.5 using the data of Tintaru *et al.* (2001) for the density of 8CB; pendant droplets of 8CB could not be formed in the smectic regime, and droplets in the nematic regime were sometimes unstable.

The interfacial tension is a monotonically increasing function of temperature throughout the nematic regime and in the isotropic phase beyond the N-I transition, with a possible discontinuity at T_{NI}. The general trend of the temperature dependence of the interfacial tension of 5CB is the same whether we use our own density difference measurements or the densities of individual phases as reported in the literature, although the magnitudes differ. The increase with temperature in the nematic phase is consistent with expectations from the calculations of Li and Denn (2002) if 5CB and 8CB are homeotropic at the interface, in which case the loss of nematic order with increasing temperature is the dominant contribution. A homeotropic orientation is consistent with Cognard's (1984) observation of normal alignment of 5CB on a polymethylsiloxane surface, as well as with atomistic simulations by Doerr and Taylor (1999) for the orientation of 5CB at the surface of amorphous polyethylene.

The increase in interfacial tension above T_{NI} suggests residual nematic order in the droplets beyond the bulk transition. A small birefringent ring was observed in the droplets above the bulk transition temperature using a polarizing microscope, indicating induced order at the interface. This appears to be analogous to Kocevar and Musevic's (2001) observation of stable surface-induced order in 5CB at a silanated glass surface at 20 K above T_{NI}. Molecular field theory calculations and Monte Carlo simulations of the N-I transition in surface-aligned nematic films by Lu *et al.* (1993) suggest an order parameter of 0.6 in a surface boundary layer at $1.5T_{NI}$.

Finally, the inability to form an 8CB droplet at temperatures below the S-N transition implies that the interfacial tension is too low to balance the gravitational force at the tip of the needle, and that the interfacial tension increases with temperature in

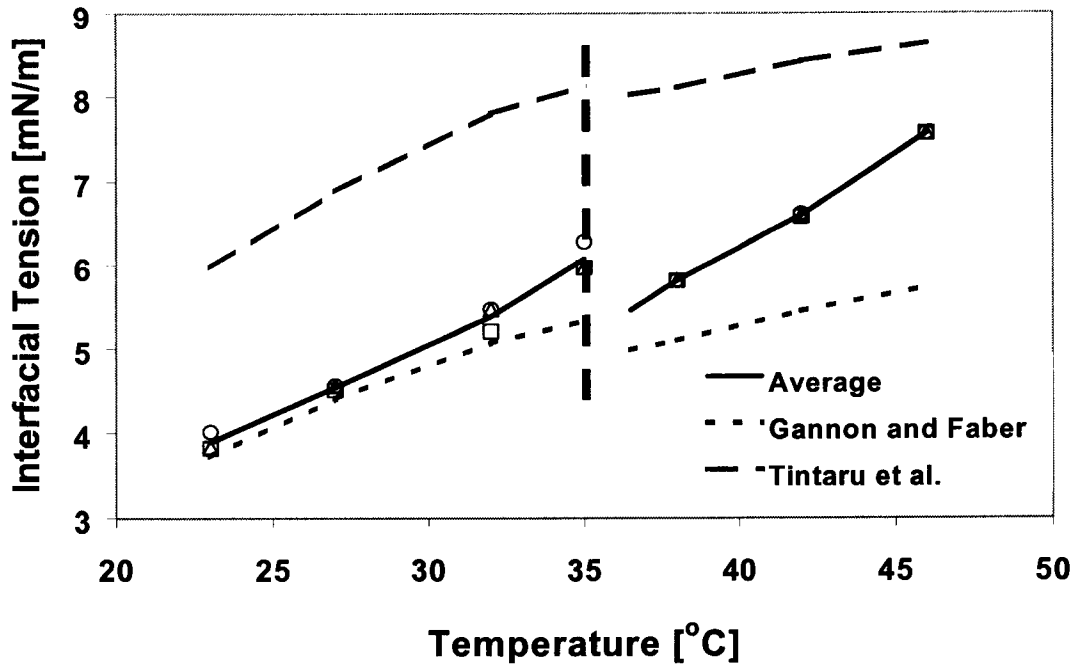

Fig 3.4: Interfacial tension between 5CB and PDMS as a function of temperature. The solid line passes through the average of three data points and uses the measured density difference shown in Fig. B1. The upper dashed line uses the density data of Tintaru *et al.*(2001) for 5CB, while the lower dotted line uses the density data of Gannon and Faber (1978). The dashed vertical line shows the bulk N-I transition temperature.

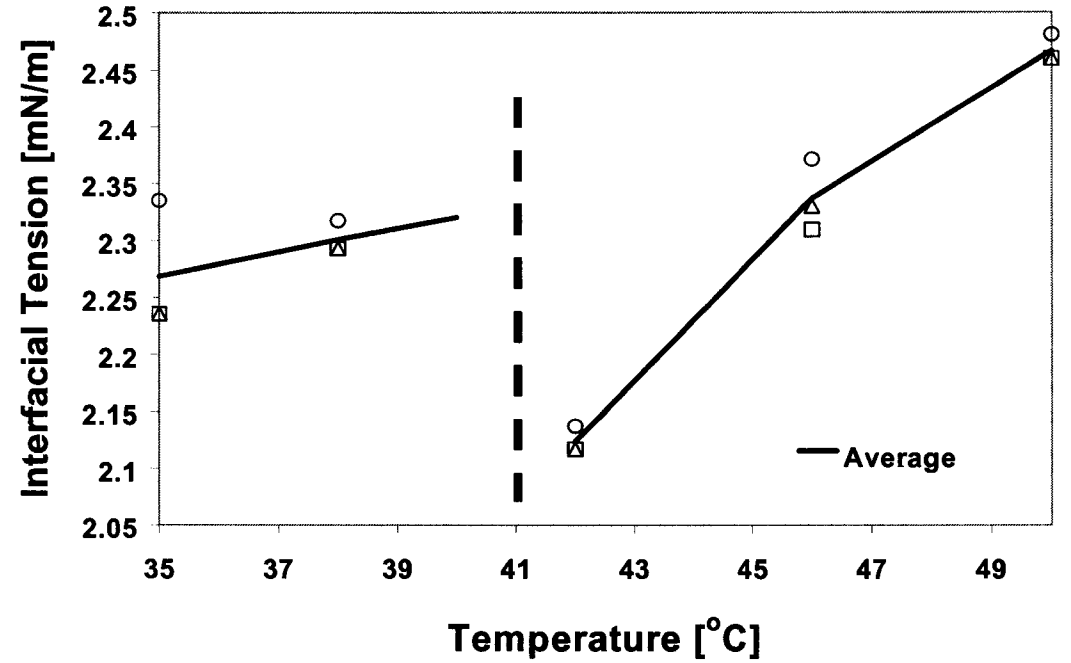

Fig 3.5: Interfacial tension between 8CB and PDMS as a function of temperature. The solid line passes through the average of three data points using the density data of Tintaru *et al.* (2001) for 8CB. The dashed vertical line shows the bulk N-I transition temperature.

passing from the smectic to the nematic.

3.3 CONCLUSIONS

The unusual temperature dependence of the interfacial tension between a thermotropic low-molar mass nematic liquid crystal and an amorphous liquid, in which the interfacial tension is an increasing function of temperature, is probably a consequence of homeotropic orientation at the interface and the loss of nematic order with increasing temperature. That the increase of interfacial tension with temperature extends well above the bulk N-I transition is apparently because of the residual nematic order at the interface that is observed by optical microscopy. The interfacial tension in the smectic-A phase appears to be even less than that in the nematic, but direct measurements cannot be made.

Chapter 4

DIELECTRIC SPECTROSCOPY OF LIQUID CRYSTALLINE DISPERSIONS

Dispersions of liquid crystalline droplets in an amorphous liquid matrix are of interest in a variety of applications, including display technology and as precursors for self-reinforced polymer composites, and the interface between a structured fluid and one without structure is itself of considerable inherent interest. Broadband dielectric relaxation spectroscopy (DRS), with a frequency range that can reach eighteen decades, is potentially a powerful technique for characterizing the dynamical processes in these multiphase systems, where the dynamics of the dispersed phase include molecular motions ranging from local processes to cooperative molecular rearrangements.

Strong orientation-dependent forces between the constituent molecules govern the characteristic behavior of liquid crystals. As a consequence of these forces the molecules in a liquid crystal mesophase tend to lie with their long axes parallel to a particular direction, called the director. The reorientational process in such a system therefore differs from that in an isotropic medium by the presence of torques that favor molecular alignment parallel to the director. Dielectric relaxation spectroscopy provides one of the most direct methods for investigating the consequences of an orientation-dependent torque in liquid crystals. Dielectric spectroscopy has been applied to liquid crystals in a number of studies (Rondelez *et al.*, 1971; Bose *et al.*, 1987; Kreul *et al.*, 1992; Carius *et al.*, 1996; Sinha and Aliev, 1998; Frunza *et al.*, 1999; Mijovic and Sy, 2000; Itatani and Shikata, 2001; Drozd-Rzodska and Rzoska, 2002), and the theory of the dielectric response of monodomain and polydomain liquid crystals is addressed in Kozak *et al.* (1991) and Williams (1994). Most studies have addressed bulk liquid crystalline phases.

Carius and coworkers (1996) measured the dielectric response of blends of polymer liquid crystals with polycarbonate. The studies most relevant to the work described here are those of Sinha and Aliev (1998) and Frunza and coworkers (1999), who studied the dielectric response of molecular liquid crystals in highly confined environments, the former in porous glass matrices and the latter in molecular sieves. Both found a strong effect of confinement on the dielectric response of the liquid crystals.

We report here on the dielectric response of dispersions of two biphenylcarbonitriles ("5CB" and "8CB") that exhibit isotropic and liquid crystalline phases in a polydimethylsiloxane matrix. The interfacial tensions between these carbonitriles and polydimethylsiloxane have the unusual property of increasing with temperature (Rai *et al.*, 2003) because of coupling between the structure and the interface.

4.1 Dielectric Relaxation

The amount of charge that builds up in a material in response to an imposed electric potential is time dependent. The speed of polarization depends on the rate of electronic and atomic polarization and permanent dipole orientation. For electronic or atomic polarization, this speed corresponds to the electronic and atomic vibration and is very rapid. These rapid polarizations are termed *instantaneous polarization.* In the case of dipole-orientation polarization, however, since reorientation of molecules or molecular segments is involved, the process is slowed by friction from the surrounding molecules, and equilibrium is reached only in relatively long time. When the field is removed, it again takes a long time for polarization to disappear. This phenomenon is called *dielectric relaxation.*

When a static electric field is imposed on a dielectric material, polarization follows accompanying dielectric relaxation of the dipoles. Under ac conditions, where the electric field changes sign sinusoidally, the time-delayed response of the dipoles gives rise to dielectric loss. This loss is in addition to the conduction loss due to the presence of charge carriers. When a time-harmonic electric field is applied, the polarization dipoles flip constantly back and forth. Since the charge carriers have a finite mass, the field must do work to move them and the response may not be instantaneous. Hence, the polarization vector may lag behind the applied electric field, which is noticeable especially at higher frequencies.

The dielectric response of materials with non-zero dc conductivity to a small amplitude alternating current voltage at a frequency f measured in Hz is usually described in terms of the Debye equation, as follows:

$$\varepsilon^* = \varepsilon_\infty + \frac{\varepsilon_S - \varepsilon_\infty}{1 + 2\pi j f \tau} - j\frac{\sigma_0}{2\pi\varepsilon_0 f} \tag{4.1}$$

or, equivalently,

$$\varepsilon' = \varepsilon_\infty + \frac{\varepsilon_S - \varepsilon_\infty}{1 + 4\pi^2 f^2 \tau^2} \tag{4.2a}$$

$$\varepsilon'' = 2\pi f \tau \frac{\varepsilon_S - \varepsilon_\infty}{1 + 4\pi^2 f^2 \tau^2} + \frac{\sigma_0}{2\pi\varepsilon_0 f} \tag{4.2b}$$

The frequency dependent real and imaginary parts of the complex relative permittivity ε^* are known as the capacitive dielectric constant (ε') and the dielectric loss factor (ε''), respectively. ε_∞ and ε_S are the relative permittivities of the material at infinite and zero frequencies, respectively, τ is a relaxation time, σ_0 is the static (dc) conductivity, and ε_0 is the permittivity of free space. We use this formalism as a frame

of reference in this study. From the Debye model represented by Eq. (4.2), the asymptotic limits of ε' and ε'' are

$$\omega \to 0: \qquad \varepsilon' \to \varepsilon_0; \qquad \varepsilon'' \to \infty \tag{4.3a}$$

$$\omega \to \infty: \qquad \varepsilon' \to \varepsilon_\infty; \qquad \varepsilon'' \to 0 \tag{4.3b}$$

ε'' diverges as $\omega \to 0$ because of the non-zero σ_0. ε_∞ is associated with electronic and atomic polarization (Weingartner, 2001). Also,

$$\omega \to 0: \qquad \omega\varepsilon_0\varepsilon' \to 0; \qquad \omega\varepsilon_0\varepsilon'' \to \sigma_0 \tag{4.3c}$$

$$\omega \to \infty: \qquad \omega\varepsilon_0\varepsilon' \to \infty; \qquad \omega\varepsilon_0\varepsilon'' \to \sigma_0 + \frac{\varepsilon_0\left(\varepsilon_S - \varepsilon_\infty\right)}{\tau} \tag{4.3d}$$

These asymptotic limits of ε' and ε'' are helpful in determining the model parameters. The constancy of $\varepsilon'' \times \omega$ at low frequencies for poorly conducting media provides one of the best methods of evaluating their dc conductance (Hill *et al.*, 1969), as the constancy of this factor ensures that spurious electrode and other effects are eliminated.

4.2 EXPERIMENT

4.2.1 Materials

4'-pentyl-4-biphenylcarbonitrile (*5CB*) and 4'-octyl-4-biphenylcarbonitrile (*8CB*) were purchased from Sigma-Aldrich and used as received. 5CB undergoes a crystal-to-nematic transition at 21°C and a first order nematic-to-isotropic transition at 35°C. 8CB undergoes a crystal-to-smectic-A transition at 22.5°C, a relatively broad apparent second-order smectic-to-nematic transition between 32°C and 34°C, and a first order nematic-to-isotropic transition at 41°C. The matrix fluid for most experiments was 60 cSt polydimethylsiloxane 200 fluid (*PDMS*), which was purchased from Sigma-Aldrich and

used without further purification. The molecular weight of PDMS 200 is about 2500. High viscosity PDMS was used in some experiments to study the effect of suspending fluid viscosity. The number-average molecular weight of the 30,000 cSt PDMS used is 67,700, while that of the 60,000 cSt PDMS is 116,500.

4.2.2 Sample Preparation

The dispersion was prepared by adding a measured amount of 5CB or 8CB to the PDMS and stirring by hand with a spatula. Droplet size distributions were not obtained because of the opacity of bulk samples, but typical droplet sizes observed in the optical microscope were of order 20 μm. Most experiments reported here were for dispersions containing 6.2% 5CB or 5% 8CB by weight. The dispersion was then allowed to rest for a few hours in a dry environment in order to expel entrapped air bubbles, after which the sample was loaded in the dielectric sample cell. The dispersed phase and PDMS 200 are density matched, hence no settling or creaming of the dispersion occurred over periods much longer than the time from sample preparation to completion of an experiment. We assume throughout that the structural states of the biphenylcarbonitriles in the droplets are the same as in the bulk, but we do note that a small birefringent ring was observed in the 5CB droplets above the bulk isotropic transition temperature, indicating induced nematic order at the interface. This order appears to be analogous to Kocevar and Musevic's (2001) observation of stable surface-induced order in 5CB at a silanated glass surface at 20°C above the bulk nematic-to-isotropic transition. Molecular field theory calculations and Monte Carlo simulations of the nematic-to-isotropic transition in surface-aligned nematic films by Lu *et al.* (1993) suggest an order parameter of 0.6 in a surface boundary layer at temperatures considerably above the bulk transition.

4.2.3 Dielectric Relaxation Spectroscopy

The dielectric relaxation spectroscopy (DRS) experiments were carried out on a commercial broadband dielectric spectrometer (BDS-80) from Novocontrol GmbH, using a cylindrical sample cell having a diameter of 19.21 mm and a gap of 0.27 mm between the plates. A photograph of the BDS-80 is shown in Fig. 4.1. The reported temperature resolution of the Quatro temperature controller is 0.01°C, with a range from –196°C (liquid Nitrogen temperature) to 400°C. The accessible impedance range for the Alpha High Resolution Dielectric and Impedance Analyzer is from 0.01 to 10^{14} Ω, with a reported tan (δ) accuracy of 3 x 10^{-5}. The root-mean-square voltage used in all experiments was 1.00 V.

All the BDS-80 parts are interfaced to a computer via an IEEE488 connection. The WinDETA data acquisition software available with the Alpha impedance analyzer provides the user interface to the spectrometer. WinDETA automatically performs the sample cell calibration with the only input of sample cell dimensions, and can do dielectric and impedance measurements as functions of frequency, temperature, time, ac voltage, dc-bias, or any multi dimensional combination of four functionalities.

4.3 RESULTS

4.3.1 Pure Components

The capacitive dielectric constant, ε', and the dielectric loss factor, ε'', of 5CB are shown as functions of frequency with temperature as a parameter in Figs. 4.2a and 4.2b, respectively. The corresponding data for 8CB are shown in Figs. 4.3a and 4.3b. The qualitative behavior is the same for both materials. With the exception of the gradual decrease in ε' at lower frequencies, which may be due to convection, the behavior can

be described by single-mode Debye relaxation with dc conductivity included (Eqs. 4.2a and 4.2b). The high-frequency (~10^7 Hz) peak in ε'' and the corresponding gradual decrease in ε' correspond to reorientation of the molecules around the short axis of the molecule in the applied alternating electric field. ε'' is more sensitive to temperature than ε'.

The capacitive dielectric constant, ε', and the dielectric loss factor, ε'', of the PDMS 200 at different temperatures are shown in Figs. 4.4a and 4.4b, respectively. Both spectra are insensitive to temperature. The fluctuation in ε'' at around 3 x 10^6 Hz appears to be a systematic error in this frequency range at small values (~10^{-3}) of ε''.

4.3.2 Spectra of Dispersions

Figure 4.5 shows the dielectric spectrum of a dispersion containing 6.2% 5CB in PDMS 200 at temperatures in both the isotropic and nematic phases. These five spectra are representative of data at more then twenty temperatures. The positive slope in ε'' at high frequencies corresponds to the peak at around 10^7 Hz in the pure component that is associated with reorientation around the short axis. There is a new temperature-dependent peak in ε'', and a corresponding shoulder in ε', at around 1000 Hz; the region around the peak is shown on a larger scale in Fig. 4.6. This peak decreases in magnitude and moves to higher frequencies with increasing temperature. The same behavior is observed for a dispersion containing 5% 8CB in PDMS 200 in the smectic, nematic, and isotropic regimes of the dispersed phase. Figure 4.7 shows an enlarged view of the region around the dielectric loss peak for the 5% 8CB dispersion in PDMS 200. There is no qualitative change in the behavior of dielectric spectra as the dispersed phase passes from smectic to nematic to isotropic state.

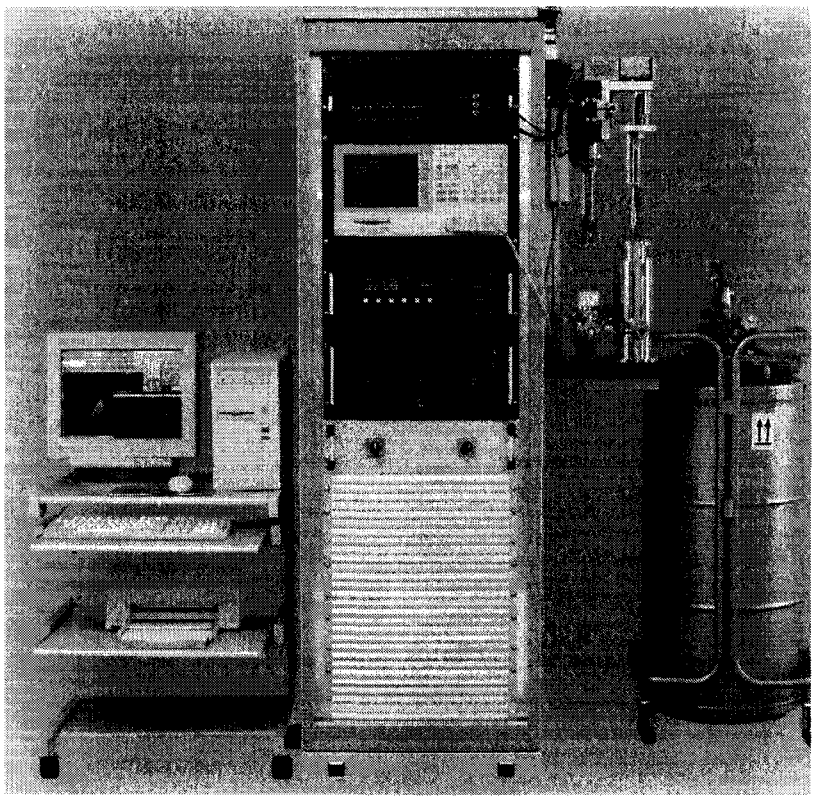

Fig 4.1: A Photograph of the Dielectric Spectrometer

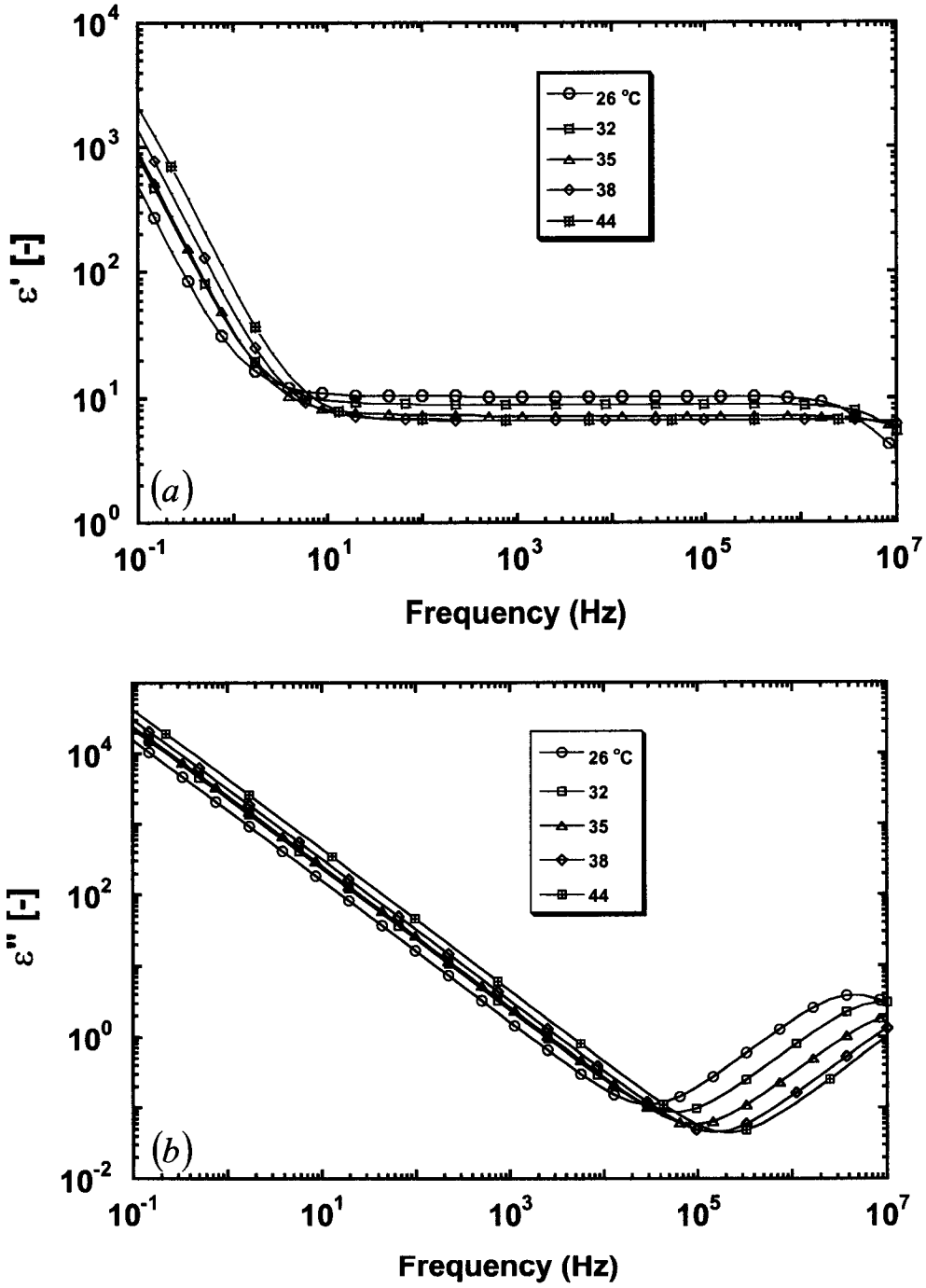

Fig 4.2: Frequency-dependent (a) capacitive spectrum $\varepsilon'(\omega)$ and (b) loss spectrum $\varepsilon''(\omega)$ of 5CB at different temperatures.

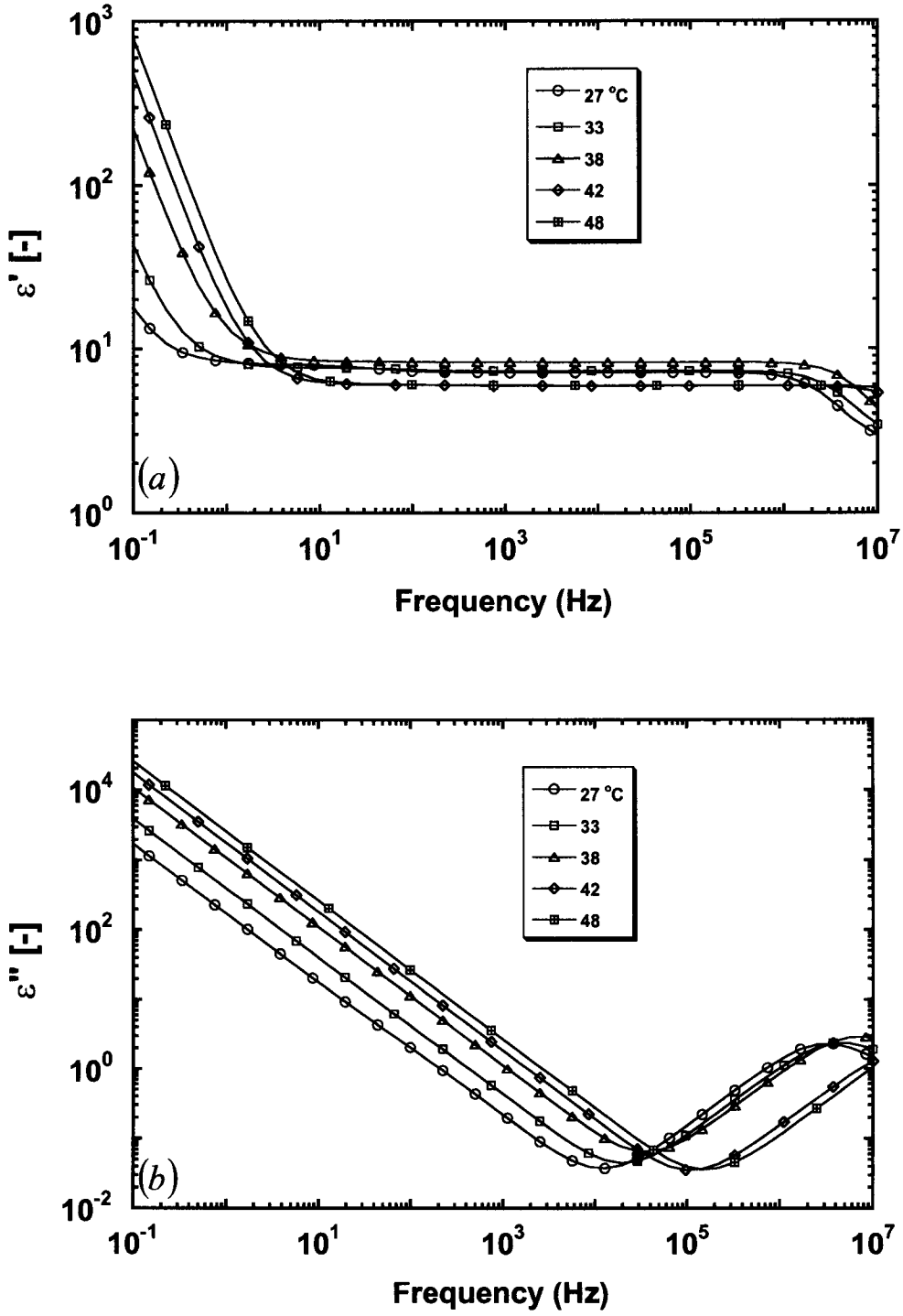

Fig 4.3: Frequency-dependent (a) capacitive spectrum $\varepsilon'(\omega)$ and (b) loss spectrum $\varepsilon''(\omega)$ of 8CB at different temperatures.

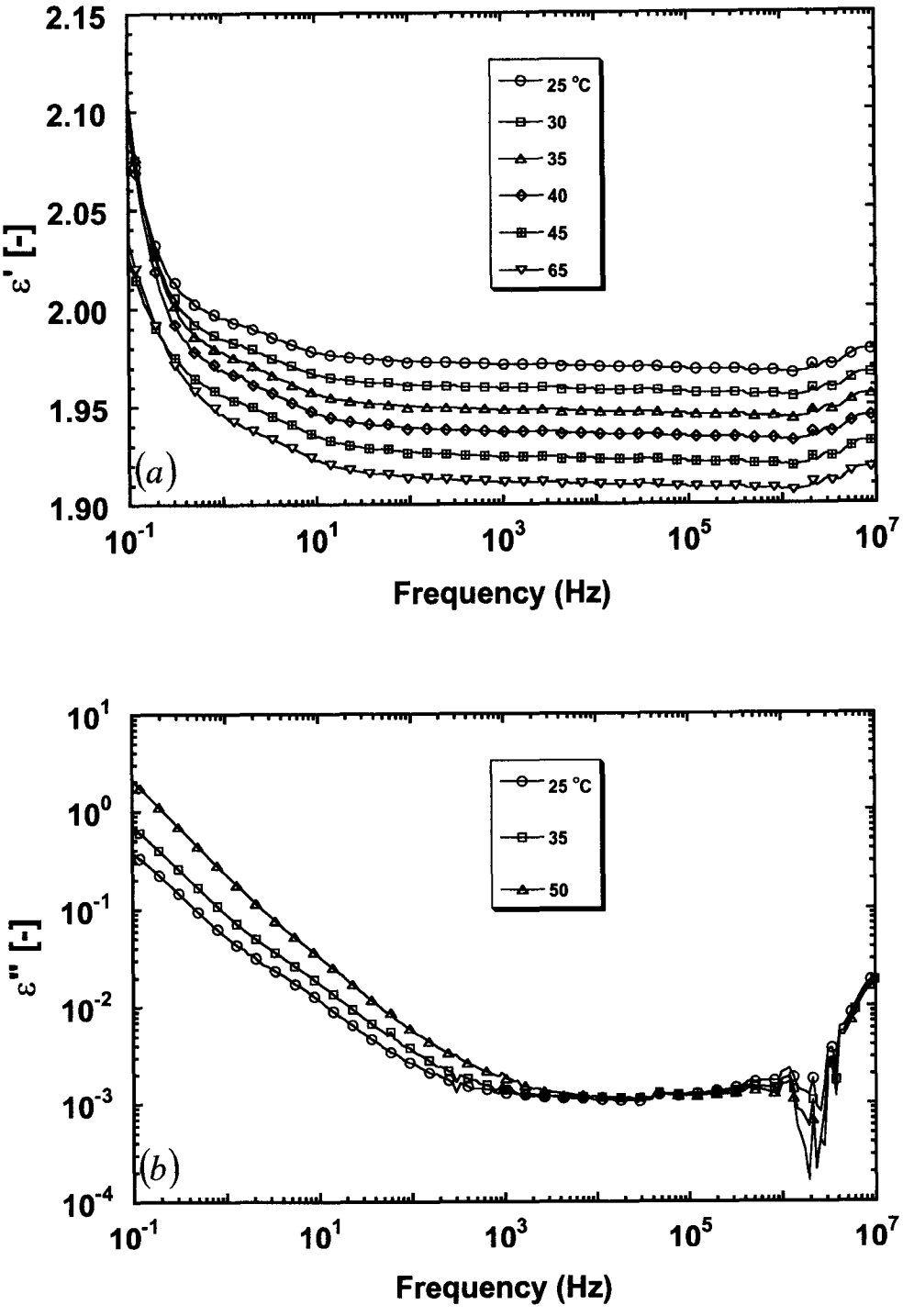

Fig 4.4: Frequency-dependent (a) capacitive spectrum $\varepsilon'(\omega)$ and (b) loss spectrum $\varepsilon''(\omega)$ of PDMS 200 at different temperatures.

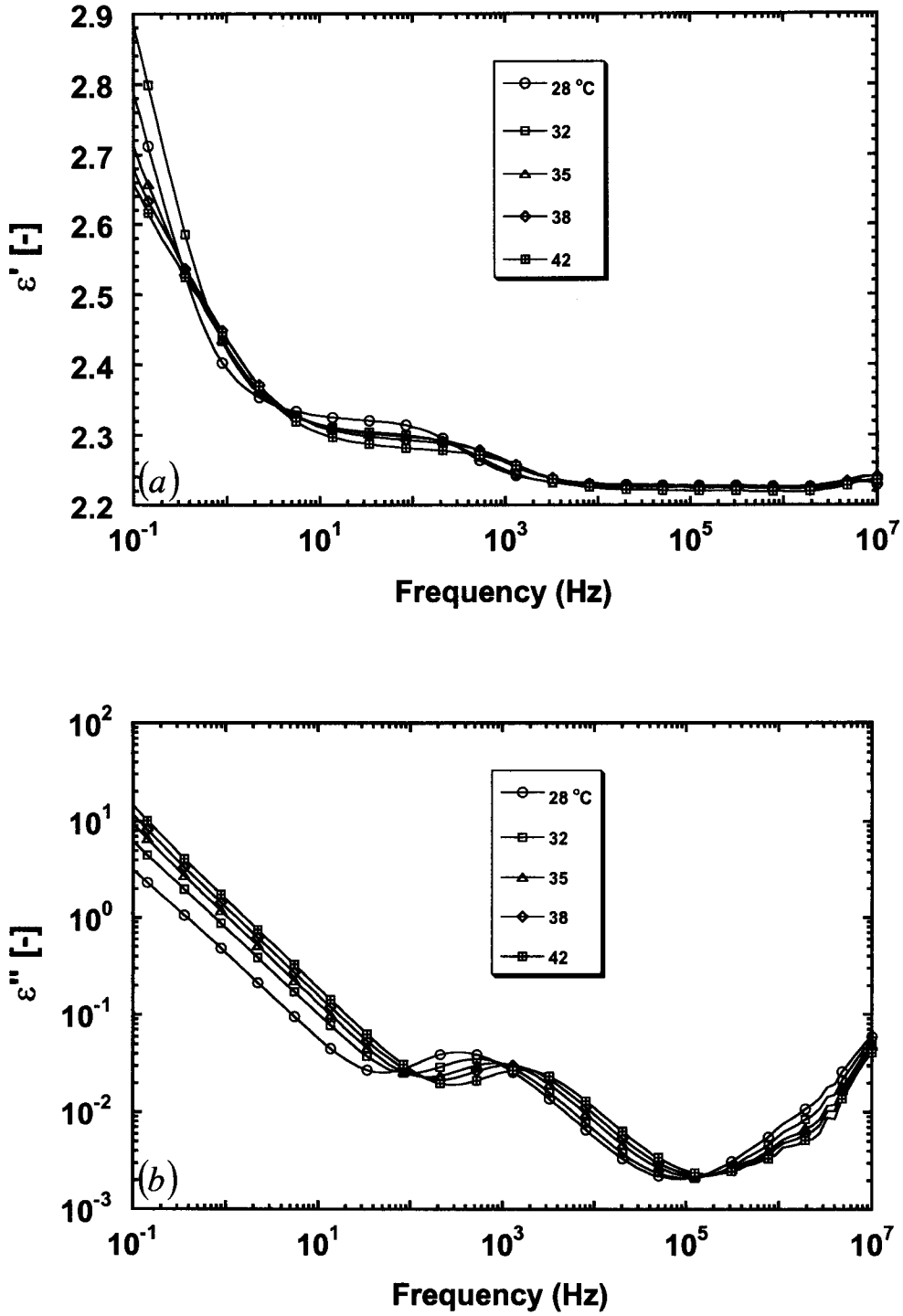

Fig 4.5: Frequency-dependent (a) capacitive spectrum $\varepsilon'(\omega)$ and (b) loss spectrum $\varepsilon''(\omega)$ of a 6.2 % dispersion of 5CB in PDMS 200 at different temperatures.

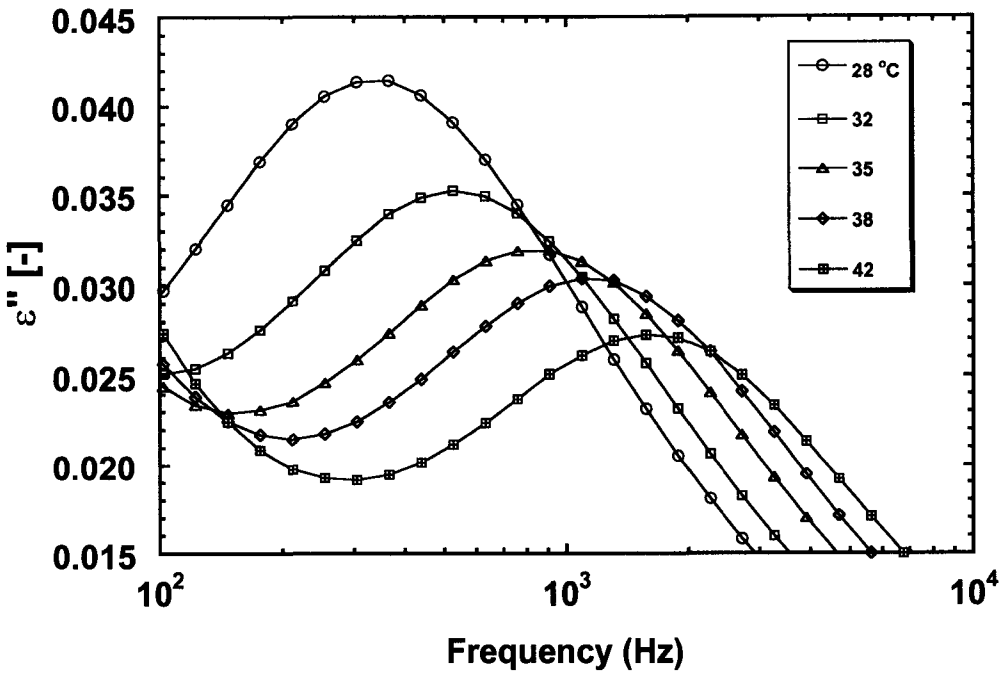

Fig 4.6: Enlarged view of frequency-dependent loss peak spectrum of a 6.2 % dispersion of 5CB in PDMS 200 at different temperatures.

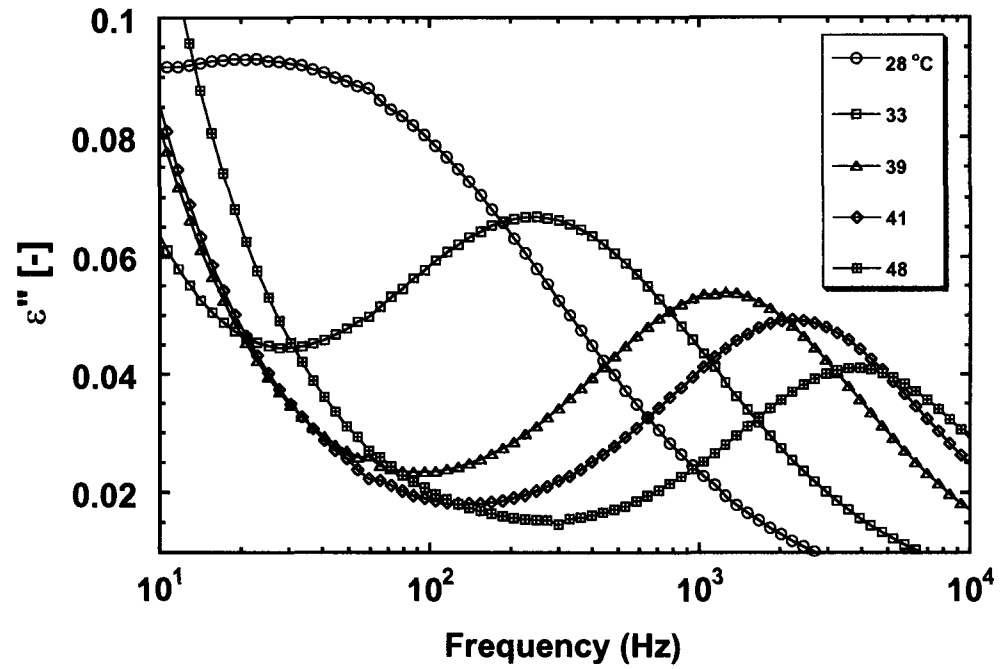

Fig 4.7: Enlarged view of frequency-dependent loss peak spectrum of a 5 % dispersion of 8CB in PDMS 200 at different temperatures.

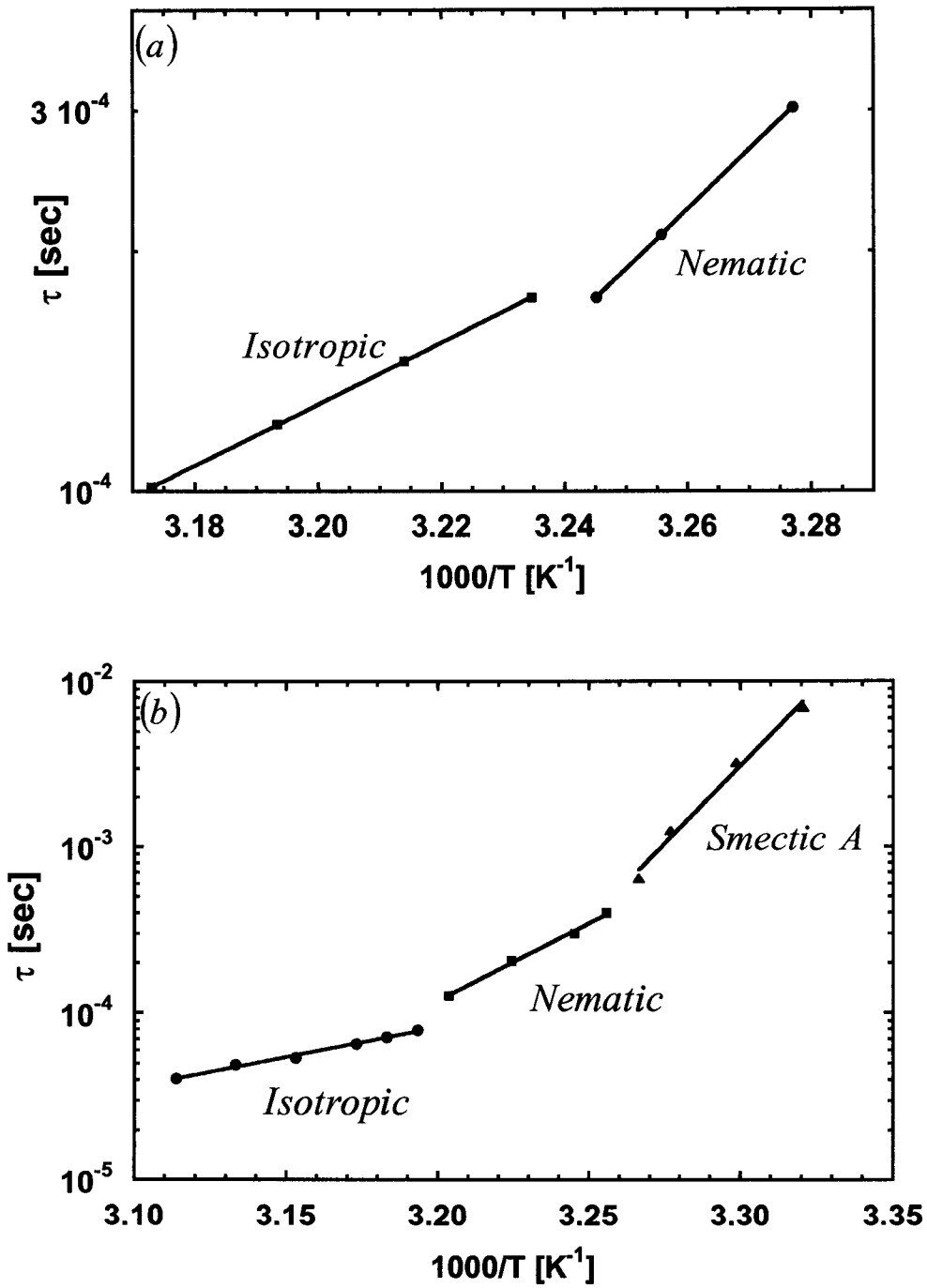

Fig 4.8: Characteristic relaxation times of (a) a 6.2% dispersion of 5CB in PDMS 200 and (b) a 5% dispersion of 8CB in PDMS 200 plotted versus reciprocal temperature.

The peak in the dielectric loss factor characterizes a new dynamic process that is associated with the presence of the biphenylcarbonitrile droplets in the PDMS matrix. The relaxation time, τ, is defined as $1/(2\pi f_{max})$, where f_{max} is the frequency in Hz at which the maximum occurs. The relaxation time is plotted versus reciprocal temperature in Figs. 4.8a and 4.8b for the 5CB and 8CB blends, respectively. The data can be fit in each structural regime of the dispersed phase with a Van't Hoff (or Arrhenius) temperature dependence of the form $\exp(E_a/T)$, with a substantial change in slope at the phase transitions. The values of E_a in the isotropic phase are 3,900 K for the 5CB dispersion and 3,600 for the 8CB dispersion; in the nematic phase they are 7,400 K for 5CB and 9,300 K for 8CB. E_a is 21,000 for the 8CB blend in the smectic phase. Hence, the relaxation process is highly dependent on the structure of the dispersed phase: smectic, nematic, or isotropic.

4.3.3 Effect of Matrix Viscosity

The strong sensitivity of the activation energy associated with the intermediate peak to the structure of the dispersed phase (i.e., smectic, nematic, or isotropic), particularly the extremely high activation energy in the constrained smectic state, suggests that resistance to deformation may play a role in the dielectric response, in which case the viscosity ratio between dispersed and matrix phases would be important. High molecular weight PDMS has a sufficiently different density from the biphenylcarbonitriles that sedimentation is a problem, and data could be obtained only for a single temperature per run and in a limited temperature range. Spectra for dispersions of 6.2% 5CB in the two high viscosity PDMS matrices at 30°C are shown in Fig. 4.9. The

peaks in ε'' move to lower frequencies and higher magnitudes relative to the PDMS 200 suspension.

4.3.4 Effect of Droplet Concentration

Dielectric spectra for 4%, 6.2%, and 9% dispersions of nematic 5CB in PDMS 200 at 30°C are shown in Fig. 4.10. The observed droplet sizes are insensitive to the 5CB concentration. The intermediate peak in the loss spectrum occurs at essentially the same frequency for both 6.2% and 9% dispersions, although there is a change in the magnitude. The peak is not observed in the 4% dispersion. A similar result is obtained at 40°C, where bulk 5CB is isotropic.

4.3.5 Effect of Droplet Size

A sample of a 6.2% dispersion of 5CB in PDMS 200 was sonicated for two hours prior to measurement of the dielectric spectrum. Sonication reduced the typical droplet size as observed in the optical microscope to about 1 μm. Spectra at 30°C are shown in Fig. 4.11. The effect of reducing the droplet size by an order of magnitude is to move the intermediate peak to a four-fold higher frequency, with little or no change to the loss spectrum at low and high frequencies.

4.3.6 Effect of Water Solubility in PDMS

The -C≡N end group on the aromatic dibenzene backbone could be sensitive to water. Hence, one series of controlled experiments was carried out to determine the possible effect of trace amounts of water in the PDMS that might have migrated to the interface. A 5CB dispersion prepared in the usual manner was divided into three parts. The first was kept in a desiccator under vacuum for 144 hours. The second was left open

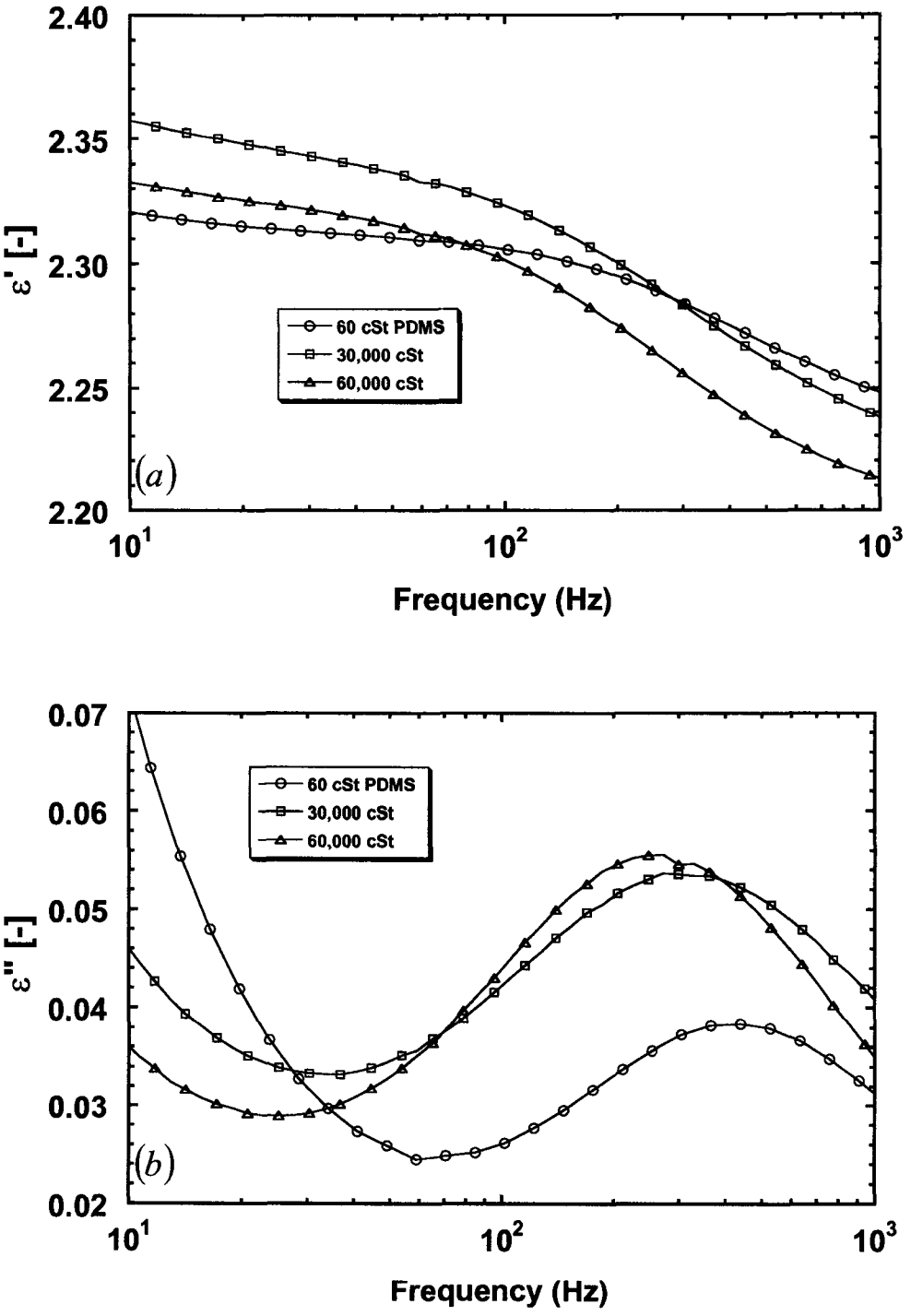

Fig 4.9: Frequency-dependent (a) capacitive spectrum $\varepsilon'(\omega)$ and (b) loss spectrum $\varepsilon''(\omega)$ of 6.2 % dispersions of 5CB in three polydimethylsiloxanes of different viscosities at 30°C.

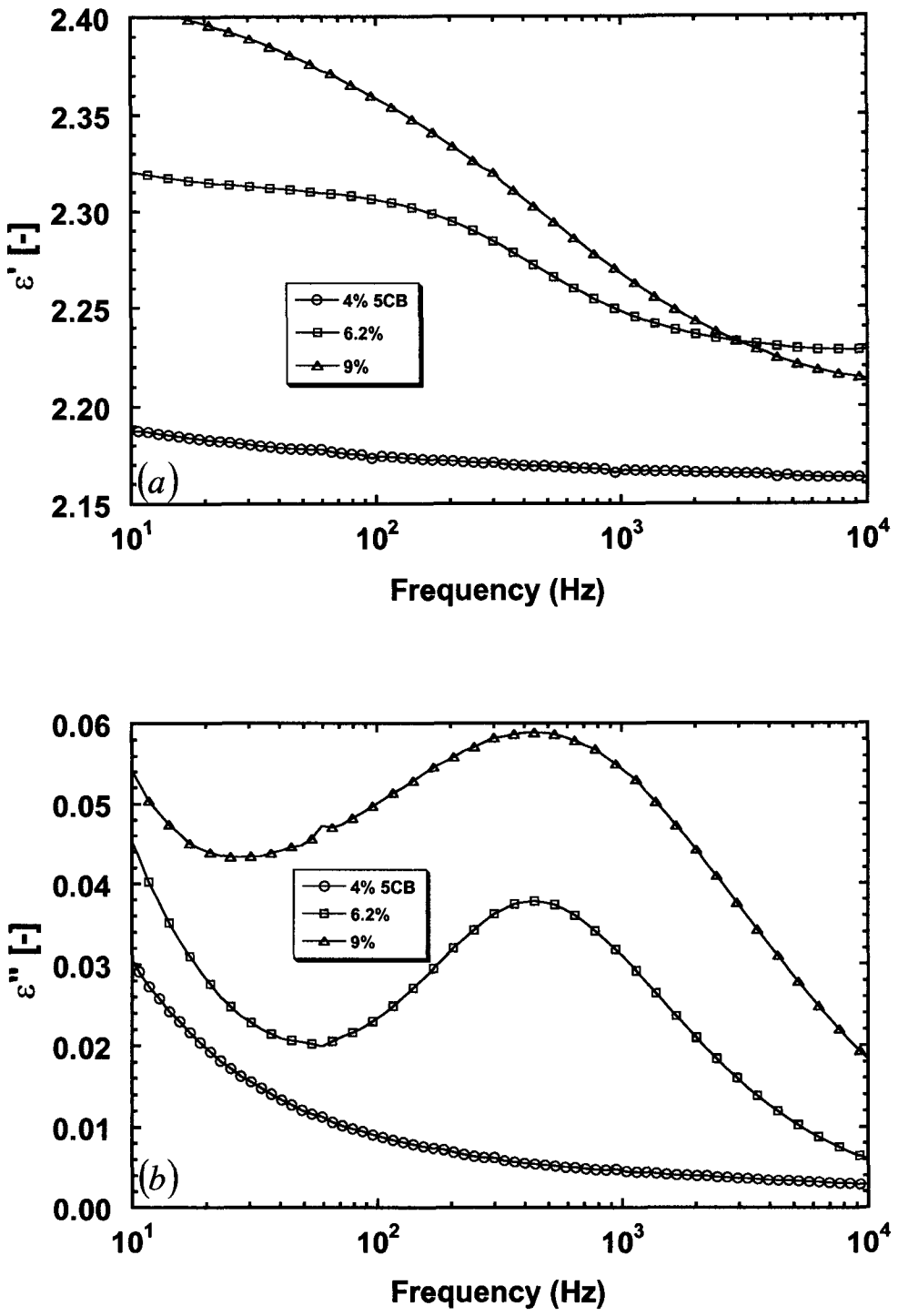

Fig 4.10: Frequency-dependent (a) capacitive spectrum $\varepsilon'(\omega)$ and (b) loss spectrum $\varepsilon''(\omega)$ of dispersions having different 5CB concentrations in PDMS 200 at 30°C.

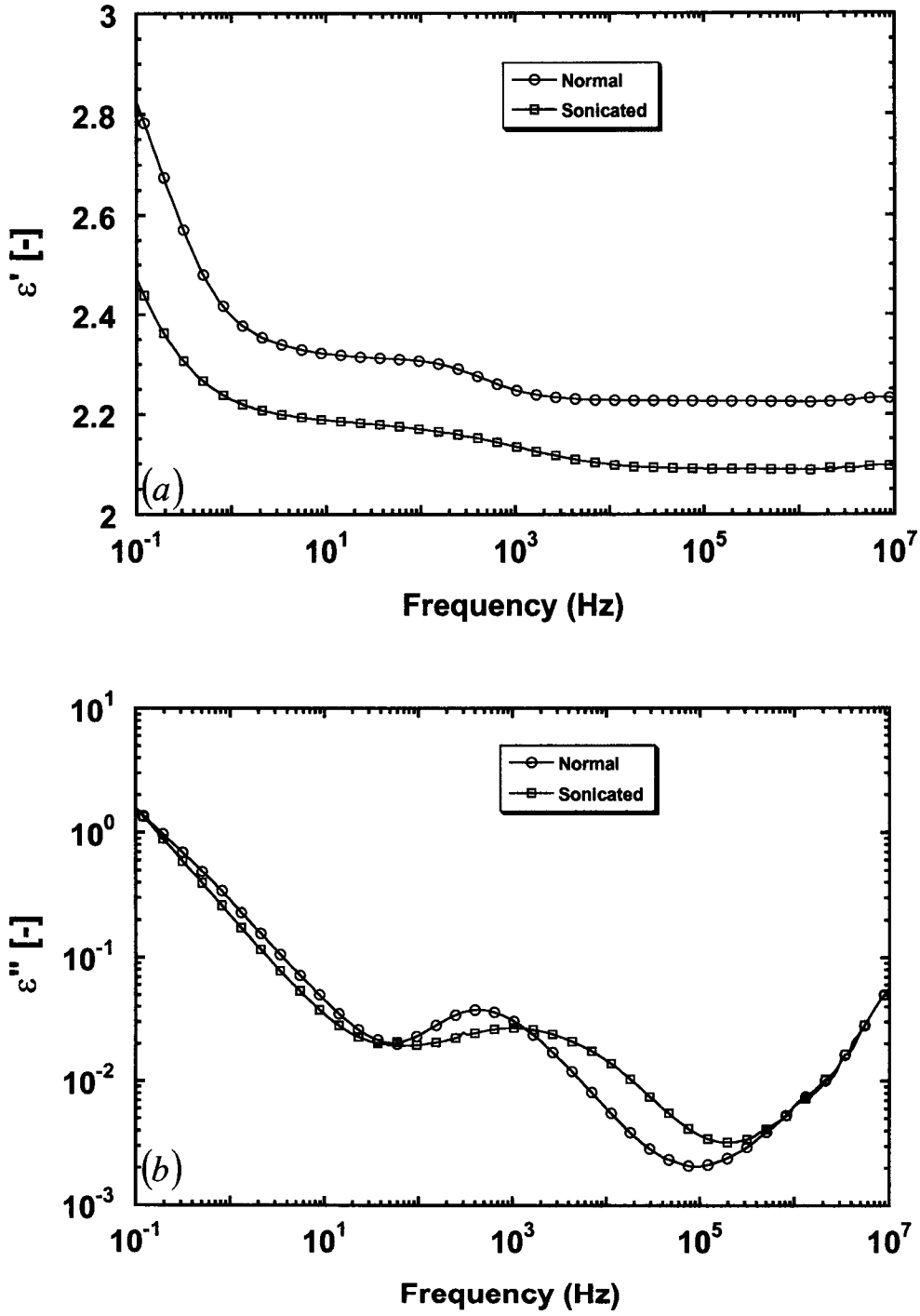

Fig 4.11: Frequency-dependent (a) capacitive spectrum $\varepsilon'(\omega)$ and (b) loss spectrum $\varepsilon''(\omega)$ of unsonicted and sonicated 6.2 % dispersions of 5CB in PDMS 200 at 30°C.

in the air for 144 hours. The third was kept in a tightly capped vial. The dielectric spectra at 33°C were essentially the same in the three cases, and the results are shown in Appendix C.

4.4 Maxwell-Wagner Polarization

Maxwell-Wagner interfacial polarization occurs in multiphase systems with unequal dielectric properties. The Maxwell-Wagner model for a random distribution of noninteracting isotropic homogeneous spheres with complex permittivity ε_D^* in an isotropic matrix with complex permittivity ε_M^* leads to an effective medium theory (*EMT*), or a mixing rule, for the complex permittivity ε_B^* of the blend:

$$\varepsilon_B^* = \varepsilon_M^* \frac{\varepsilon_D^* + 2\varepsilon_M^* - \phi(\varepsilon_D^* - \varepsilon_M^*)}{\varepsilon_D^* + 2\varepsilon_M^* + 2\phi(\varepsilon_D^* - \varepsilon_M^*)} \tag{4.4}$$

Figure 4.12 compares the experimental data for the 6.2% 5CB dispersion at 32°C to the EMT calculation using the pure component spectra. The EMT does show an intermediate peak in ε'' and an intermediate shoulder in ε', but the peak location is displaced to lower frequencies than the experimental peaks and the magnitude is larger. The location and magnitude of the experimental and EMT peaks for the 5CB blend are shown as functions of temperature in Fig. 4.13. The difference between the EMT and experiment is well outside the range of experimental uncertainty and increases with increasing temperature. Similar behavior is observed for the 8CB dispersion, as shown in Fig. 4.14. It is notable that the closest agreement between experimental and EMT peaks is in the highly constrained smectic regime of 8CB.

The dispersion also shows a higher steady-state conductivity than would be predicted from the pure component data, possibly because of the migration of trace

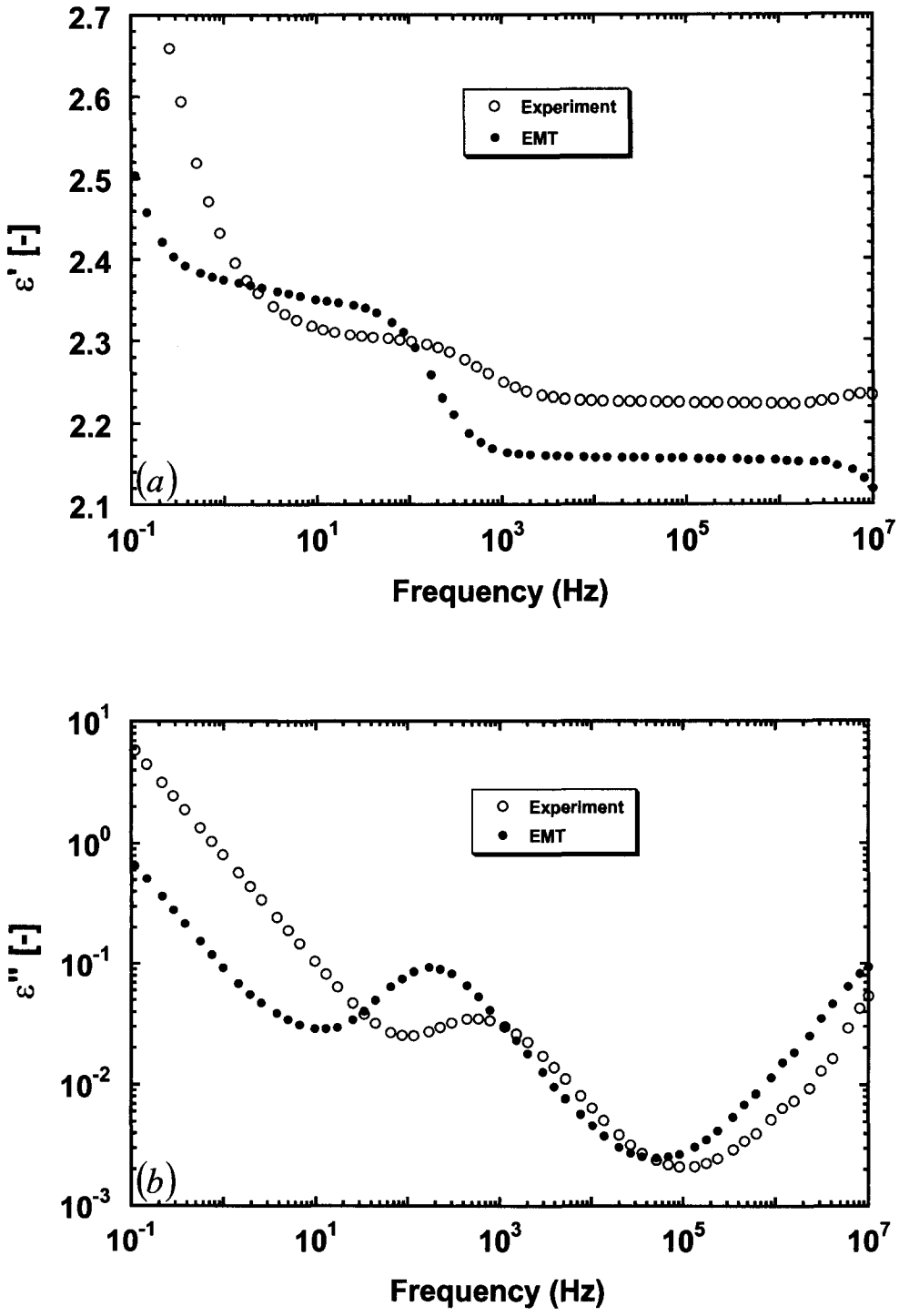

Fig 4.12: Comparison of Effective Medium Theory prediction of (a) capacitive spectrum $\varepsilon'(\omega)$ and (b) loss spectrum $\varepsilon''(\omega)$ with dielectric experiments for a 6.2% dispersion of 5CB in PDMS 200 at 32 °C.

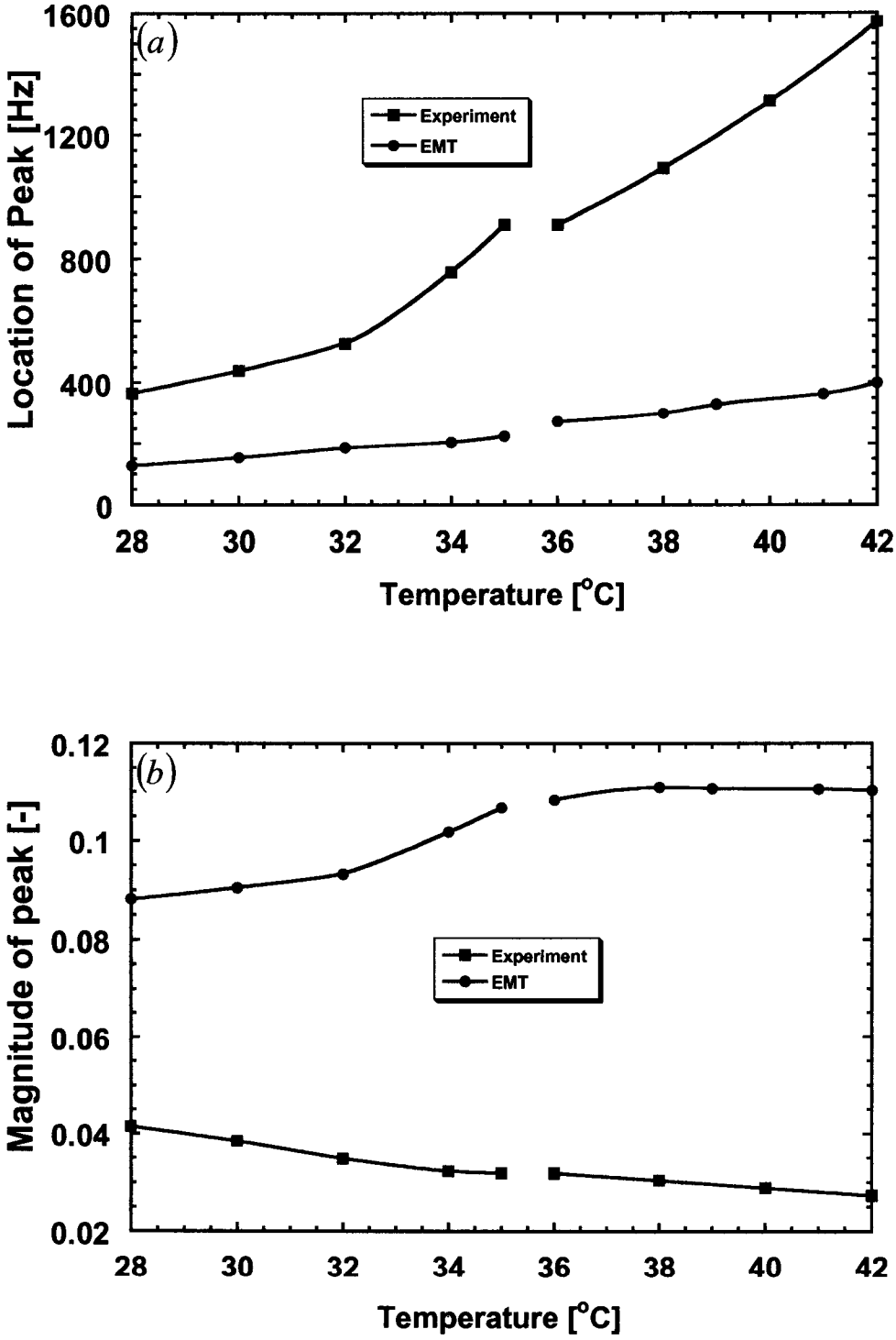

Fig 4.13: Comparison of (a) location and (b) magnitude of effective medium theory with experimental peaks for a 6.2% dispersion of 5CB in PDMS 200.

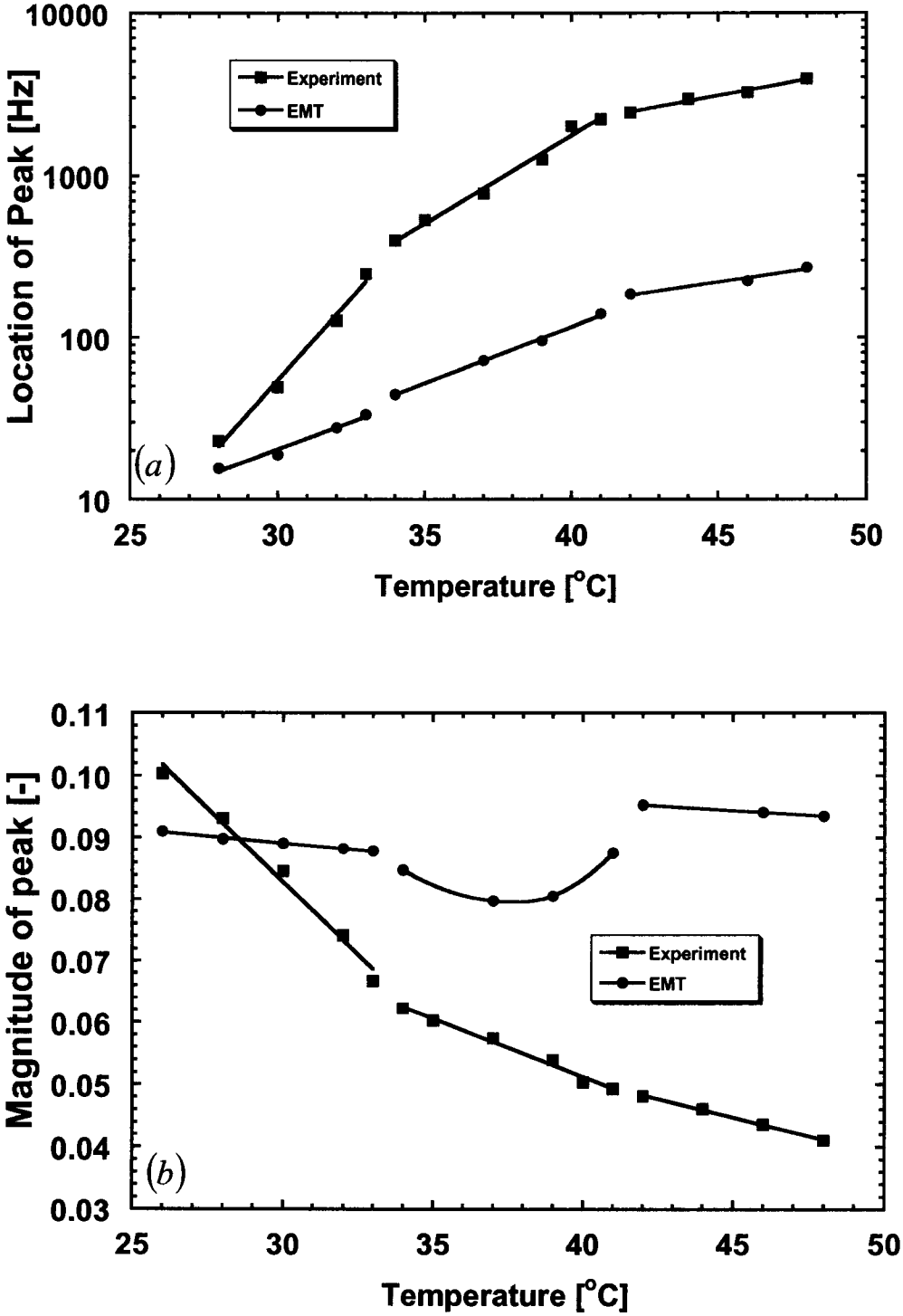

Fig 4.14: Comparison of (a) location and (b) magnitude of effective medium theory with experimental peaks for a 5% dispersion of 8CB in PDMS 200.

amounts of impurities. The EMT calculation in the region of the peak is unaffected by the value of the steady-state conductivity, which can be adjusted so that the EMT and experimental blend data agree at frequencies below 10 Hz. Similarly, the presence of adsorbed water or other surface effects at the droplet interface could cause tangential surface conductivity, which would increase the effective dielectric loss of the dispersed phase. Increasing the dielectric loss of the droplet phase by 30%, however, does not change the predicted EMT loss peak by any significant amount, as discussed in Appendix C. Finally, we considered the possible existence of an outer droplet layer with dielectric properties different from the inner core, using the formalism of Jones (1995) for different shell thicknesses. Unacceptable values of the dielectric properties of the shell region (negative ε'', for example) were always required in order to bring the EMT and experimental peaks together. The analysis of layered spherical model for the droplet and its implications in dielectric measurement is given Appendix C.

4.5 INTERFACE DEFORMATION

The strong sensitivity of the activation energy associated with the intermediate peak to the structure of the dispersed phase (i.e., smectic, nematic, or isotropic), particularly the extremely high activation energy in the constrained smectic state, and the sensitivity of the peak to the viscosity ratio and droplet size, suggest that droplet deformation may play a role in the dielectric response. There is a characteristic frequency regime in which a droplet interface is sensitive to an imposed mechanical deformation, with a corresponding relaxation time given by Palierne (1990) as

$$\tau_M = \frac{R\eta_M f\left(\frac{\eta_D}{\eta_M}\right)}{\gamma} \tag{4.5}$$

R is the droplet radius, η_M the viscosity of the matrix phase, η_D the viscosity of the dispersed phase, and γ interfacial tension. $f(\eta_D/\eta_M)$ is a known function of the viscosity ratio for isotropic Newtonian fluid droplets in a Newtonian fluid matrix, and we use the Newtonian fluid relation here. The shear viscosities of the biphenylcarbonitriles and the interfacial tensions between the biphenylcarbonitriles and PDMS are reported in Rai *et al.* (2003).

The mechanical relaxation times for the standard dispersions in PDMS 200 are shown in Fig. 4.15, together with the experimental relaxation times corresponding to the dielectric peaks. (There are no data for the interfacial tension of the 8CB-PDMS system in the smectic regime because the interfacial tensions were too low to measure using pendant-drop tensiometry.) The times are of comparable magnitude, indicating that the response to droplet deformation will occur in the same frequency range as the dielectric response to the applied field.

The notion that liquid droplets are deformable if external forces operate against the effect of interfacial tension in sufficient strength is essentially true only for the structure-less isotropic droplets. Orientation-dependent forces between the constituent molecules could significantly govern the characteristic behavior of structured anisotropic droplets. Liquid crystal molecules inside a spherical droplet dispersed in a flexible matrix and subjected to a far-field electric field are under the influence of four kinds of forces:

1. Frank elastic force, which tends to align nematogens parallel to one another.
2. Anchoring force at the interface, which tends to align nearby nematogens in a given way, say parallel or perpendicular to the interface.

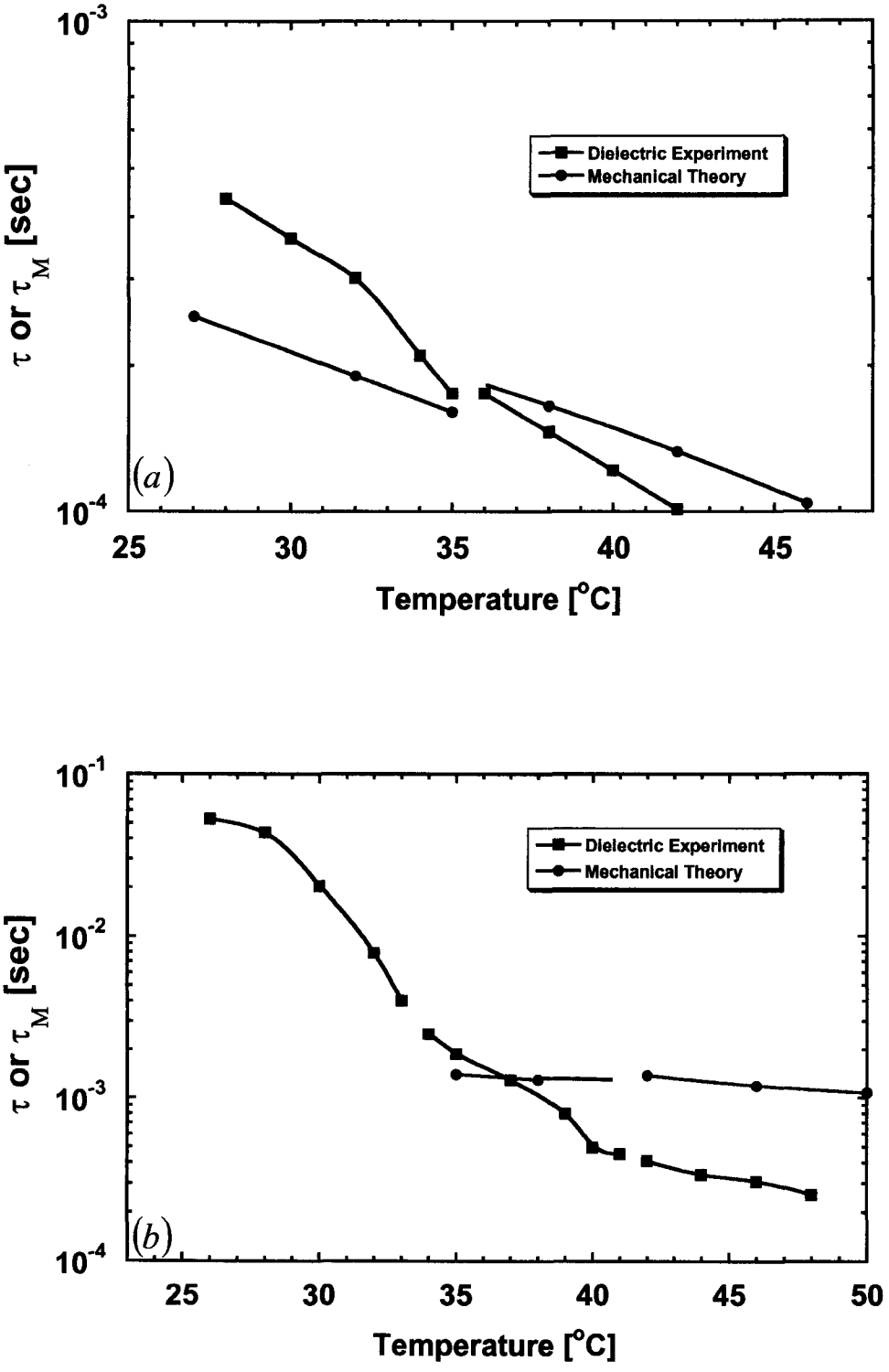

Fig 4.15: Comparison of experimental dielectric relaxation time (■) with predicted mechanical relaxation time (●) for (a) a 6.2% dispersion of 5CB in PDMS 200 and (b) a 5% dispersion of 8CB in PDMS 200 as functions of temperature.

3. Force due to the applied electric field, which tends to align molecular dipoles parallel to electric field lines.
4. Interfacial tension, which resists any deformation of the interface.

An intricate interplay between these four competitive forces determines the equilibrium orientation of the molecules, if there exists one, and the shape of the resulting nematic droplet. A rough estimate of energies due to these forces are: Frank elastic energy = 10^{-6} J/m^2 (Zakharov and Dong, 2001); anchoring energy = $10^{-5} - 10^{-7}$ J/m^2 (Andrienko *et al.*, 1998); electrical energy = 2.5×10^{-3} J/m^{-2}; and surface energy = 3×10^{-3} J/m^2 (Rai *et al.*, 2003). Since the electrical energy is orders of magnitude larger than the anchoring energy and the Frank elastic energy, whether or not the imposed electric field can cause a deformation of the nematic droplet depends on the relative values of the electric pressure and the Laplace pressure, γ/R, where γ is the interfacial tension and R is the radius of the droplet. 5CB and 8CB have permanent dipole moments (Doerr and Taylor, 1999), in which case the electric pressure is of order NpE_0, where N is the number of permanent dipoles per unit volume, p is the dipole moment, and E_0 is the root-mean-square magnitude of the imposed field. The permanent dipole moment of 5CB is 7.1 D (Clark *et al.*, 1997), which gives a ratio NpE_0R/γ of order unity. Alternatively, O'Konski and Harris's (1957) formalism for the mean deformation of a nearly spherical isotropic droplet suspended in a dielectric medium in a constant field, which does *not* include the presence of permanent dipoles, predicts an eccentricity of 0.2% under our experimental conditions; a deformation of this magnitude could be significant. A similar deformation is obtained from the dynamic analysis of Torza *et al.* (1971), although the

latter work predicts a dynamic shape response at twice the input frequency. None of these calculations takes the anisotropy or the entropic (Frank) elasticity of the liquid crystalline state into account.

4.6 DISCUSSION

The dielectric response of the biphenylcarbonitrile dispersions in PDMS exhibits an unusual dielectric relaxation at frequencies in the range 100 – 1,000 Hz that depends strongly on the structural state of the dispersed fluid, whether isotropic, nematic, or smectic. It is tempting to identify this relaxation with Maxwell-Wagner polarization, since an intermediate Maxwell-Wagner peak is predicted by the effective medium theory, Eq. (4.4). This simple explanation is problematic, however; the predicted Maxwell-Wagner relaxation is shifted considerably from the experimentally observed peak.

An alternative explanation is that this intermediate relaxation is associated with the restricted motion of oriented molecules at the interface. This explanation is consistent with Sinha and Aliev's (1998) observation of a relaxation process at frequencies below 10^4 Hz in 5CB and 8CB in porous glass matrices with pores sizes of 10 and 100 nm, and Frunza and coworkers' (1999) observation of a slow relaxation in 5CB and 8CB confined to mesopores with diameters less than 2.5 nm in a molecular sieve, both of which were attributed to confined molecular motion. There are problems with this explanation as well, however. First, it is unlikely that such a relaxation would depend on the viscosity of the matrix fluid. Second, the separation between this peak and the expected Maxwell-Wagner peak is sufficiently large that one would then expect to see the latter peak as well, especially since the predicted Maxwell-Wagner peak has a magnitude that is more

than twice that of the experimentally observed peak; indeed, the experimental peak is not observed at all in the 4% dispersion.

The most likely explanation consistent with the experimental observations is that the effective dielectric response of the dispersed phase is altered because of an interaction with the imposed field that causes a small deformation of the droplets. The observed peak is then the expected Maxwell-Wagner relaxation, but shifted because of the coupling between the dipolar motion and the interfacial mechanics. Interfacial motion would be greatly reduced (and probably eliminated) in the high-viscosity suspending fluids, and droplet deformation would be expected to be least in the smectic phase, and less in the nematic than in the isotropic. The insensitivity of the experimental peak frequency to droplet concentration and the shift to higher frequencies with reduced droplet size are qualitatively consistent with this picture.

4.7 CONCLUSION

The fact that the dielectric response of the 5CB and 8CB dispersions depends strongly on the structural state of the droplets and the viscosity of the suspending PDMS is suggestive of a coupling with the mechanics of the interface that affects the spectrum of the dispersed phase and shifts the Maxwell-Wagner peak. This result is unexpected, but it is the most consistent explanation of the observation of a single relaxation in the 100 – 1,000 Hz range that is displaced from the expected Maxwell-Wagner relaxation. The mechanics of the interaction between an oscillating electric field and a droplet of a material that can undergo a liquid crystalline transition and contains a permanent dipole is an unsolved problem, so our explanation must remain speculative.

Chapter 5

ELECTRODYNAMICS OF NEMATIC-ISOTROPIC INTERFACES

Liquid crystalline phases share with fluids the ability to flow; however, liquid crystals also exhibit anisotropies in their dielectric, magnetic, and optical properties that are reminiscent of crystals. This chapter deals with the dynamics of the nematic phase, which possesses the simplest liquid crystalline order. In this phase, rod-like organic molecules align, on average, parallel to each other, forming a long-range orientational order, but the centers of mass remain disordered, as in a conventional fluid. The mean orientation of the molecules is indicated by a unit vector, the director $\boldsymbol{n}$ (Fig. 5.1). However, $\boldsymbol{n}$ merely characterizes an axis in space, e.g., the optical axis of the birefringent nematic phase. Hence, all physical quantities that we formulate in the following must be invariant under the inversion of the director ($\boldsymbol{n} \rightarrow -\boldsymbol{n}$).

Since the nematic state breaks the continuous rotational symmetry of the isotropic fluid, nematics dynamics are governed by an extension of the Navier-Stokes equations, first formulated by Ericksen (1960, 1961) and Leslie (1966, 1968).

We begin with a phenomenological description of the nematic phase. First, we introduce the total free energy from which a static director configuration is determined by minimization. We then discuss the fluctuations of the hydrodynamic director on the basis of the Leslie-Ericksen equations governing the dynamics of the director. Finally, we apply these governing equations to investigate the mechanics of planar interface and slightly curved interface.

5.1 Free Energy

Thermodynamics tells us that a complete knowledge of a system on a macroscopic level follows from the minimization of an appropriate thermodynamic potential. We use the free energy, which consists of bulk and surface terms, as the relevant potential:

$$W_t = \int_V W dV + \int_S W_S dS \tag{5.1}$$

$$W = W_g + W_e \tag{5.2}$$

W_t denotes the total free energy of the system, where W is the bulk free energy density of the system and W_S is the surface free energy density. V is the volume and S is the surface area. W is made up of two components: W_g, the elastic free energy density; and W_e, the electrical free energy density. It is straightforward to include any other bulk free energy term, like magnetic free energy or energy due to distribution of electric charges, in Eq. (5.2).

5.1.1 Elastic Free Energy Density

In the absence of any external field and surface effects, the energetic ground state of a nematic liquid crystal is a spatially uniform director field; any deviation from uniformity costs elastic energy. The Frank long-range elastic free energy density function is (de Gennes, 1993):

$$\begin{aligned} 2W_g &= K_1(\nabla.\boldsymbol{n})^2 + K_2(\boldsymbol{n}.\nabla\times\boldsymbol{n})^2 + K_3|\boldsymbol{n}\times(\nabla\times\boldsymbol{n})|^2 \\ &= K_1(\nabla.\boldsymbol{n})^2 + K_2(\boldsymbol{n}.\nabla\times\boldsymbol{n})^2 + K_3(\boldsymbol{n}.\nabla)\boldsymbol{n}.(\boldsymbol{n}.\nabla)\boldsymbol{n} \end{aligned} \tag{5.3}$$

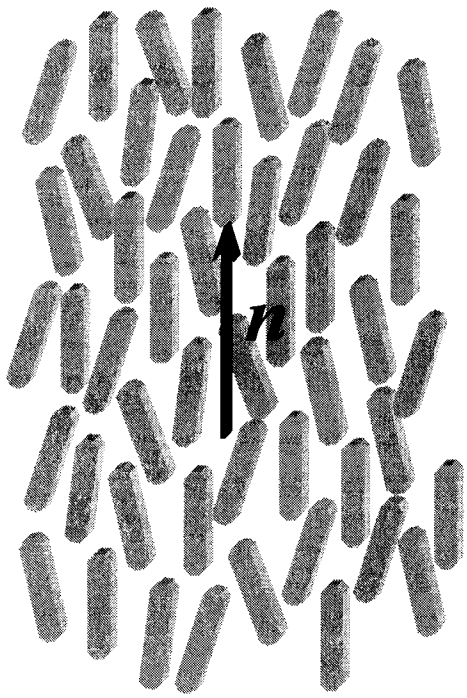

Fig 5.1: The nematic director ***n***

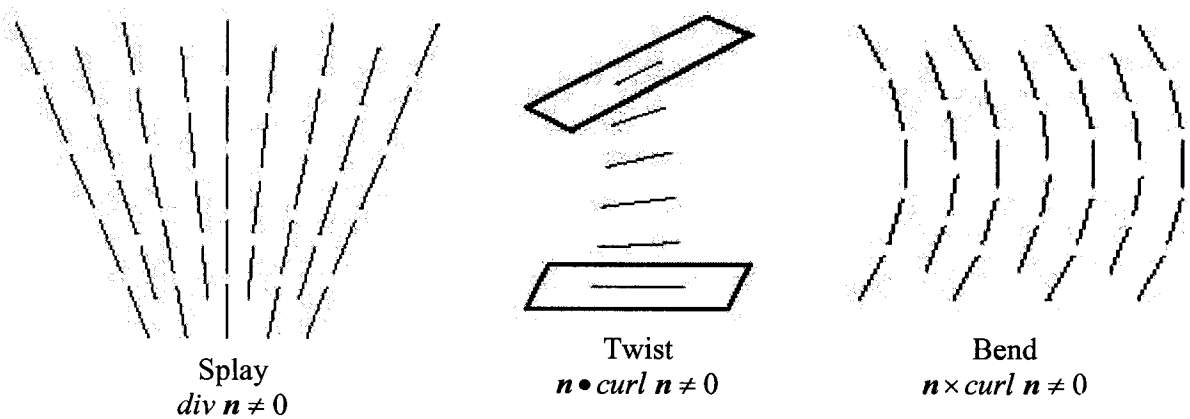

Fig. 5.2: Schematic of the three elastic modes (a) Splay (K_1), (b) twist (K_2), and (c) bend (K_3).

where K_1, K_2 and K_3 denote the *splay*, *twist* and *bend* Frank elastic constants (Fig. 5.2), respectively:

K_1: conformations with $div\,\boldsymbol{n} \neq 0$ $\quad (Splay)$
K_2: conformations with $\boldsymbol{n}.curl\,\boldsymbol{n} \neq 0$ $\quad (Twist)$
K_3: conformations with $\boldsymbol{n} \times curl\,\boldsymbol{n} \neq 0$ $\quad (Bend)$

5.1.2 Electric Free Energy Density

Electric fields polarize matter in two ways: by orienting molecules with permanent dipoles and by deforming electron clouds within individual atoms and molecules. The permanent dipole polarization vector, $\boldsymbol{P}$, is related to characteristics of individual dipoles by $\boldsymbol{P} = N\boldsymbol{p}$. Here, N represents the number of dipoles per unit volume and $\boldsymbol{p}$ is the individual dipole moment. The dipole polarization vector is directed towards the director of nematics, and therefore $\boldsymbol{P} = -P\boldsymbol{n}$, where P is the magnitude of permanent polarization vector. The dipole polarization vector contributes to the total electric free energy density as (Feynman *et al.*, 1964)

$$W_{dipole} = -\boldsymbol{P}.\boldsymbol{E} = -P\boldsymbol{n}.\boldsymbol{E} \tag{5.4}$$

The spontaneous polarization of molecules upon application of a field gives an added contribution to the total free energy density as given by (Self *et al.*, 2002)

$$W_{induced} = -\frac{1}{2}\varepsilon_0\varepsilon_\perp \boldsymbol{E}.\boldsymbol{E} - \frac{1}{2}\varepsilon_0\varepsilon_a(\boldsymbol{n}.\boldsymbol{E})^2 \tag{5.5}$$

where $\boldsymbol{E}$ is the local electric field inside the droplet, $\varepsilon_\perp$ is the dielectric permittivity of the nematic normal to the director, ε_0 denotes the permittivity of the vacuum, $\varepsilon_a = \varepsilon_{//} - \varepsilon_\perp$ is the dielectric anisotropy of the nematic, and $\varepsilon_{//}$ denotes the dielectric permittivity of the nematic along the director.

The combined contribution of permanent dipoles and induced dipoles to electric free energy density, W_e, of the nematics is given by

$$W_e = -\frac{1}{2}\boldsymbol{D}.\boldsymbol{E} = -\frac{1}{2}\varepsilon_0\varepsilon_\perp \boldsymbol{E}.\boldsymbol{E} - \frac{1}{2}\varepsilon_0\varepsilon_a(\boldsymbol{n}.\boldsymbol{E})^2 - P\boldsymbol{n}.\boldsymbol{E} \tag{5.6}$$

The electric displacement vector $\boldsymbol{D}$ is related to the local field $\boldsymbol{E}$ by $D_i = \varepsilon_{ij}E_j + P_i$, and it includes the effect of the induced polarization as well as the permanent polarization of the material. The fact that, for transversely isotropic materials, the permittivity tensor ε_{ij} has only two distinct eigenvalues $\varepsilon_{\|}$ and $\varepsilon_\perp$ representing the permittivity parallel and perpendicular to the director has been utilized in obtaining Eqs. (5.5) and (5.6).

5.2 Static Director Field

The director field $\boldsymbol{n}$ in a given geometry follows from a minimization of the total free energy W_t under the constraint that $\boldsymbol{n}$ is a unit vector:

$$\delta W_t = 0 \qquad \text{with} \qquad \boldsymbol{n}\bullet\boldsymbol{n} = 1 \tag{5.7}$$

Even in the one-constant approximation ($K_1 = K_2 = K_3 = K$) and under the assumption of rigid anchoring of the director at the boundaries, this is a difficult problem to solve because of the additional constraint of unit length of the director. Typically, full analytical solutions exist only for one-dimensional problems [e.g., for the description of the Freedericksz transition, in which the director responds to a field that is orthogonal to the direction of surface anchoring (Chandrasekhar, 1992)], or in two dimensions when certain symmetries are assumed (Lubensky *et al.*, 1998). To handle the constraint, one can use a Lagrange multiplier or express the director in terms of tilt (Θ) and twist (Φ) angles so that the director in the local coordinate basis takes the form

$$\boldsymbol{n} = (\sin\Theta\cos\Phi, \sin\Theta\sin\Phi, \cos\Theta) \tag{5.8}$$

5.3 Hydrodynamic Equations

In the last section we concentrated on the static properties of the director field. In this section we review a set of dynamical equations coupling the flow of the liquid crystal to the dynamics of the nematic director. The dynamic state of the nematic is specified by the coupling between two vector fields, the velocity $\mathbf{v}$ and the director $\boldsymbol{n}$. This coupling requires a generalization of the Navier-Stokes equations for the fluid velocity $\mathbf{v}$ to uniaxial media and a dynamic equation for the director $\boldsymbol{n}$. We will not provide a detailed derivation of these equations, rather we will concentrate on the explanation of their meaning. In the following, we review the Leslie-Ericksen (LE) equations.

The *equation of continuity* (mass balance) for incompressible fluids is

$$\nabla \bullet \mathbf{v} = 0 \tag{5.9}$$

The *linear momentum balance* equation takes the following form:

$$\rho \dot{\mathbf{v}} = \nabla \bullet \boldsymbol{T} \tag{5.10}$$

where ρ is the fluid density and $\boldsymbol{T}$ is the total stress tensor.

The kinematic measures are:

$$2\boldsymbol{A} = \nabla \mathbf{v} + \nabla \mathbf{v}^T \tag{5.11}$$

$$2\boldsymbol{\omega} = \nabla \mathbf{v} - \nabla \mathbf{v}^T \tag{5.12}$$

$$\boldsymbol{N} = \dot{\boldsymbol{n}} - \boldsymbol{\omega} \bullet \boldsymbol{n} \tag{5.13}$$

where $\boldsymbol{A}$ and $\boldsymbol{\omega}$ are the rate of deformation tensor and the spin tensor, respectively, and $\boldsymbol{N}$ is the angular velocity of the director relative to fluid.

The stress tensor is a sum of two primary contributions: viscous and elastic. The LE constitutive equations for the stress tensor are given in terms of objective linear functions of $\boldsymbol{N}$ and $\boldsymbol{A}$. Expanding in these variables and using transversely isotropic

tensor coefficients that reflect the material symmetry, the following stress tensor is obtained (Rey and Denn, 2002):

$$\boldsymbol{T} = -p\boldsymbol{I} + \boldsymbol{\sigma} \tag{5.14}$$

$$\boldsymbol{\sigma} = \alpha_1 \boldsymbol{nnnn} : \boldsymbol{A} + \alpha_2 \boldsymbol{nN} + \alpha_3 \boldsymbol{Nn} + \alpha_4 \boldsymbol{A} + \alpha_5 \boldsymbol{nn}.\boldsymbol{A} + \alpha_6 \boldsymbol{A}.\boldsymbol{nn} - \frac{\partial W}{\partial \nabla \boldsymbol{n}}.(\nabla \boldsymbol{n})^T \tag{5.15}$$

p is the isotropic pressure; $\boldsymbol{I}$ is the unit tensor; $\{\alpha_i\}$, $i = 1 \cdots 6$, are the six Leslie viscosity coefficients; $\gamma_1 = \alpha_3 - \alpha_2$ is the rotational viscosity; and $\gamma_2 = \alpha_6 - \alpha_5 = \alpha_2 + \alpha_3$ is the irrotational torque coefficient, where the last equality follows from the Onsager reciprocal relations (due to Parodi, 1970). It may be noted that the stress tensor is not symmetric. The nonsymmetric portion of the stress tensor serves to exchange external angular momentum (associated with the flow field) and internal angular momentum (associated with rotational degrees of freedom of the molecules or microstructure).

For a uniaxial nematic liquid crystal an internal (angular) momentum balance equation is required to describe the average macroscopic orientation of the liquid crystal molecules. The *director balance law* is expressed as (Larson, 1999)

$$\gamma_1 \boldsymbol{N} + \gamma_2 (\boldsymbol{n}.\boldsymbol{A} - \boldsymbol{nnn} : \boldsymbol{A}) = \boldsymbol{h} - \boldsymbol{nn}.\boldsymbol{h} \tag{5.16}$$

$$\boldsymbol{h} = \nabla . \left(\frac{\partial W}{\partial \nabla \boldsymbol{n}} \right) - \frac{\partial W}{\partial \boldsymbol{n}} \tag{5.17}$$

This completes the set of three equations, one *scalar* (mass balance equation) and two *vector* equations (equation of motion and angular momentum balance), for the determination of seven variables: pressure, three velocity components and three orientation components.

5.4 Linear Theory

In our dielectric experiment, the orientation of the nematic rods is altered only by the applied electric field. Since the applied electric field itself is a small perturbation around zero, we expect the orientations of the molecules to remain approximately parallel to a given fixed direction (i.e., initial orientation). Therefore, we are interested in the linear version of the above theory. For this purpose, we denote the given fixed direction by $\boldsymbol{n^0}$ and let $\boldsymbol{u}$ represent a small perturbation of the director around $\boldsymbol{n^0}$. $\boldsymbol{u}$ is orthogonal to $\boldsymbol{n^0}$ to first order because of the constraint of the unit length of the director.

$$\boldsymbol{n} = \boldsymbol{n}^0 + \boldsymbol{u} \qquad \boldsymbol{n}^0 \bullet \boldsymbol{u} = \boldsymbol{0} \tag{5.18}$$

We assume that the velocity and orientational and thermal variations are sufficiently small to permit their products to be neglected, as well as products involving their derivatives; denoting the i^{th} position coordinate by x_i, this means that $u_i u_j$, $\frac{\partial u_i}{\partial x_j}\frac{\partial u_k}{\partial x_l}$, and $u_i \frac{\partial u_j}{\partial x_k}$ are zero for all i, j, k, l.

In order to be able to linearize the equation of motion and the director balance law (DBL), we must be able to find two derivatives of the bulk free energy density, $\frac{\partial W}{\partial \nabla \boldsymbol{n}}$ and $\frac{\partial W}{\partial \boldsymbol{n}}$. Manipulations are carried out in a Cartesian coordinate frame. Notations to be used frequently are $\boldsymbol{\delta}$, the *Kronecker delta*; $\boldsymbol{\varepsilon}$, the alternating unit tensor; and $n_{i,k} = \frac{\partial n_i}{\partial x_k}$.

Using the following simplifications,

$$\frac{\partial\left(\frac{\partial n_a}{\partial x_b}\right)}{\partial\left(\frac{\partial n_i}{\partial x_j}\right)} = \delta_{ai}\delta_{bj}; \quad \frac{\partial n_a}{\partial\left(\frac{\partial n_i}{\partial x_j}\right)} = 0 = \frac{\partial\left(\frac{\partial n_a}{\partial x_b}\right)}{\partial n_i}; \quad \frac{\partial n_a}{\partial n_i} = \delta_{ai} \tag{5.19}$$

we obtain

$$\frac{\partial W}{\partial n_{k,i}} = K_1(n_{a,a})\delta_{ki} + K_2\varepsilon_{abc}\varepsilon_{mik}n_m n_a n_{c,b} + K_3\left(n_i n_b n_{k,b}\right) \tag{5.20}$$

$$\frac{\partial W}{\partial n_i} = K_2\varepsilon_{abc}\varepsilon_{imp}n_{p,m}n_a n_{c,b} + K_3\left(n_{a,i}n_c n_{a,c}\right) - \varepsilon_0\varepsilon_a(n_p E_p)E_i - PE_i \tag{5.21}$$

It may be noted that the electric field does not affect the stress tensor explicitly, but gives an added contribution to the DBL through the term $-\varepsilon_0\varepsilon_a\left(n_p E_p\right)E_i - PE_i$ in $\partial W/\partial n_i$. The dimensions of $K_3 n_c^0 n_{a,c}^0 n_{a,i}^0$ and $\varepsilon_0\varepsilon_a n_p E_p E_i$ are that of pressure:

$$[K_3 n_c^0 n_{a,c}^0 n_{a,i}^0] = [N][-][\frac{1}{m}][\frac{1}{m}] = [\frac{N}{m^2}] = [\text{Pressure}]$$

$$[\varepsilon_0\varepsilon_a n_p E_p E_i] = [\frac{C^2}{Nm^2}][-][-][\frac{N}{C}][\frac{N}{C}] = [\frac{N}{m^2}] = [\text{Pressure}]$$

The linearized forms of the required terms are

$$\begin{aligned}\frac{\partial W}{\partial n_{k,i}} &= K_1 n_{a,a}^0\delta_{ki} + K_2\varepsilon_{abc}\varepsilon_{mik}n_m^0 n_a^0 n_{c,b}^0 + K_3 n_i^0 n_b^0 n_{k,b}^0 \\ &+ K_1 u_{a,a}\delta_{ki} + K_2\varepsilon_{abc}\varepsilon_{mik}\left(n_m^0 n_a^0 u_{c,b} + n_m^0 n_{c,b}^0 u_a + n_a^0 n_{c,b}^0 u_m\right) \\ &+ K_3\left(n_i^0 n_b^0 u_{k,b} + n_i^0 n_{k,b}^0 u_b + n_b^0 n_{k,b}^0 u_i\right)\end{aligned} \tag{5.22}$$

$$\begin{aligned}\left(\frac{\partial W}{\partial n_{k,i}}\right)n_{k,j} &= K_1 n_{a,a}^0\delta_{ki}n_{k,j}^0 + K_2\varepsilon_{abc}\varepsilon_{mik}n_m^0 n_a^0 n_{c,b}^0 n_{k,j}^0 + K_3 n_i^0 n_b^0 n_{k,b}^0 n_{k,j}^0 \\ &+ K_2\varepsilon_{abc}\varepsilon_{mik}\left(n_m^0 n_a^0 u_{c,b} + n_m^0 n_{c,b}^0 u_a + n_a^0 n_{c,b}^0 u_m\right)n_{k,j}^0 \\ &+ K_1 u_{a,a}\delta_{ki}n_{k,j}^0 + K_3\left(n_i^0 n_b^0 u_{k,b} + n_i^0 n_{k,b}^0 u_b + n_b^0 n_{k,b}^0 u_i\right)n_{k,j}^0 \\ &+ \left(K_1 n_{a,a}^0\delta_{ki} + K_2\varepsilon_{abc}\varepsilon_{mik}n_m^0 n_a^0 n_{c,b}^0 + K_3 n_i^0 n_b^0 n_{k,b}^0\right)u_{k,j}\end{aligned} \tag{5.23}$$

$$\frac{\partial W}{\partial n_i} = K_2 \varepsilon_{abc} \varepsilon_{imp} n_a^0 n_{c,b}^0 n_{p,m}^0 + K_3 n_c^0 n_{a,c}^0 n_{a,i}^0 - \varepsilon_0 \varepsilon_a (n_p E_p) E_i - P E_i$$
$$+ K_3 (n_c^0 n_{a,c}^0 u_{a,i} + n_c^0 n_{a,i}^0 u_{a,c} + n_{a,c}^0 n_{a,i}^0 u_c) \qquad (5.24)$$
$$+ K_2 \varepsilon_{abc} \varepsilon_{imp} (n_a^0 n_{c,b}^0 u_{p,m} + n_a^0 n_{p,m}^0 u_{c,b} + n_{c,b}^0 n_{p,m}^0 u_a)$$

It is straightforward to linearize other terms in the equation of motion and DBL, keeping in mind that all $\mathbf{v}$, $\boldsymbol{A}$, and $\boldsymbol{E}$ are small perturbations around zero. The complete linearization of the equation of motion and the DBL law will be presented on a case by case basis.

5.5 Relevance to Dielectric Experiment

In dielectric experiments of liquid crystal blends, the spherical droplets of liquid crystals are subject to perturbative electric fields. The continuous phase remains an isotropic flexible polymer matrix. With the linearized formulation of the Leslie-Ericksen continuum theory for nematic liquid crystals, we attempt to capture the dynamics at the nematic-isotropic (N-I) interface. In physical terms, we wish to calculate the deformation of the interface that comes from an imposed fluid velocity at the interface that results from the effect of the oscillating field on the director. It is speculated that the mechanics of N-I interface will be able to explain some of the differences between our dielectric experiments and Maxwell-Wagner theory (chapter 4), the later of which gives no regard to the presence or mechanics of the (N-I) interface.

In the dielectric experiment, spherical droplets of liquid crystals dispersed dilutely inside the isotropic matrix are subject to a uniform far-field electric field. The first step in tackling this problem is the determination of the local electric field ($\boldsymbol{E}$), which is dependent on $\boldsymbol{n}$ through the polarization vector. $\boldsymbol{n}$, in turn, depends on $\boldsymbol{E}$ and $\mathbf{v}$ (director balance law). Finally, $\mathbf{v}$ depends on $\boldsymbol{n}$ and $\boldsymbol{E}$ (equation of motion). Therefore,

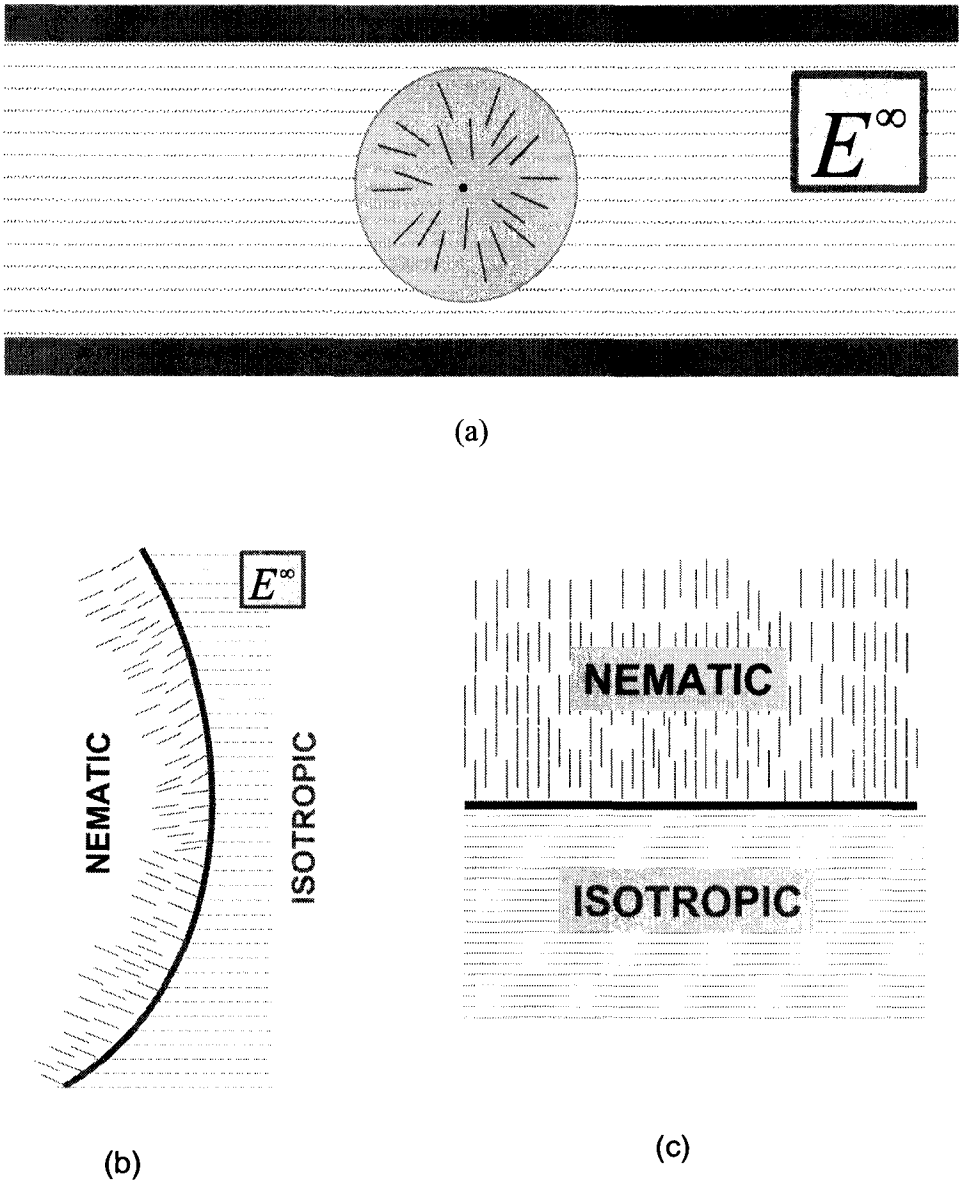

Fig. 5.3: Geometrical simplification of the complete problem. (a) Actual experimental conditions. For a very large radius of the drop, the region of the droplet close to interface (b) can be approximated by a planar geometry (c).

the coupled governing equations must be solved simultaneously for nine variables. It is not possible to solve the complete problem analytically in the most general sense. We will simplify the problem using reasonable and practical assumptions. The first assumption we make relates to the geometry of the problem. We are interested in the region of the droplet close to the interface. For large droplets, it is reasonable to assume that planar coordinates will quite satisfactorily represent the close vicinity of the interface. (See Fig. 5.3.)

5.6 Planar Geometry with Uniform Initial Configuration

Determination of the interfacial strain requires evaluating three interdependent vector fields: the electric field, $\boldsymbol{E}$; the director perturbation, $\boldsymbol{u}$; and the velocity field, $\mathbf{v}$. We will first discuss the governing equations for the electric field, to be followed by the director perturbation calculation and finally by the velocity field. Electric field and velocity field calculations are, of course, relevant to both isotropic and nematic phases, while the director perturbation calculation is relevant only to the liquid crystalline phase.

5.6.1 Electric Field Determination

Since we assume no free charge density in the liquid crystal, the electric field inside the droplet will be obtained from Maxwell's equations for the electric displacement field $\boldsymbol{D}$:

$$\nabla.\boldsymbol{D} = 0 \tag{5.25}$$

For anisotropic materials, the displacement vector $\boldsymbol{D}$ is related to the local field $\boldsymbol{E}$ by $D_i = \varepsilon_{ij} E_j$; for nematics, the permittivity tensor ε_{ij} has only two distinct eigenvalues, ε_{II} and $\varepsilon_{\perp}$, representing the permittivity parallel and perpendicular to the

director (Self *et al.*, 2002). The difference between these two, $\varepsilon_a = \varepsilon_{II} - \varepsilon_\perp$, is called the dielectric anisotropy.

Therefore, including the dc conductivity contribution,

$$\boldsymbol{D} = \varepsilon_\perp \boldsymbol{E}_\perp + \varepsilon_{II} \boldsymbol{E}_{II} + \frac{\sigma}{i\omega}\boldsymbol{E} \tag{5.26}$$

with $\boldsymbol{E}_{II} = \boldsymbol{nn}.\boldsymbol{E}$, $\boldsymbol{D} = \varepsilon_\perp \boldsymbol{E} + \varepsilon_a \boldsymbol{nn}.\boldsymbol{E} + \frac{\sigma}{i\omega}\boldsymbol{E}$. (5.27)

From $\nabla.\boldsymbol{D} = 0$ we obtain $\nabla.\left\{\varepsilon_\perp \boldsymbol{E} + \varepsilon_a \boldsymbol{nn}.\boldsymbol{E} + \frac{\sigma}{i\omega}\boldsymbol{E}\right\} = 0$, (5.28)

or equivalently, $\nabla.\left\{\varepsilon_\perp + \frac{\sigma}{i\omega}\right\}\boldsymbol{E} + \varepsilon_a(\nabla.\boldsymbol{n})(\boldsymbol{n}.\boldsymbol{E}) + \varepsilon_a \boldsymbol{n}.\nabla(\boldsymbol{n}.\boldsymbol{E}) = 0$ (5.29)

$\nabla \times \boldsymbol{E} = 0$ implies that $\boldsymbol{E}(\boldsymbol{r}) = -\nabla\phi(\boldsymbol{r})$, where $\phi(\boldsymbol{r})$ is scalar potential; hence

$$\left(\varepsilon_\perp + \frac{\sigma}{i\omega}\right)\nabla^2\phi(\boldsymbol{r}) + \varepsilon_a(\nabla.\boldsymbol{n})(\boldsymbol{n}.\nabla\phi(\boldsymbol{r})) + \varepsilon_a \boldsymbol{n}.\nabla(\boldsymbol{n}.\nabla\phi(\boldsymbol{r})) = 0 \tag{5.30}$$

$\boldsymbol{n} = \boldsymbol{n}^0 + \boldsymbol{u}$; taking $\boldsymbol{u}$ and $\nabla\phi$ to be small perturbations around zero, the last equation can be linearized as

$$\left(\varepsilon_\perp + \frac{\sigma}{i\omega}\right)\nabla^2\phi + \varepsilon_a(\nabla.\boldsymbol{n}^0)(\boldsymbol{n}^0.\nabla\phi) + \varepsilon_a \boldsymbol{n}^0.\nabla(\boldsymbol{n}^0.\nabla\phi) = 0 \tag{5.31}$$

In this limit, the scalar potential is independent of the infinitesimal director perturbation. Therefore, the electric field can be determined independently of the nematodynamics. For a uniform initial configuration (i.e., $\boldsymbol{n}^0$ independent of position) in a planar geometry,

$$\nabla.\boldsymbol{n}^0 \equiv 0,\ \boldsymbol{n}^0.\nabla(\boldsymbol{n}^0.\nabla\phi) = n_i^0 n_k^0 \frac{\partial^2\phi}{\partial x_i \partial x_k}. \tag{5.32}$$

Equation (5.31) then reduces to

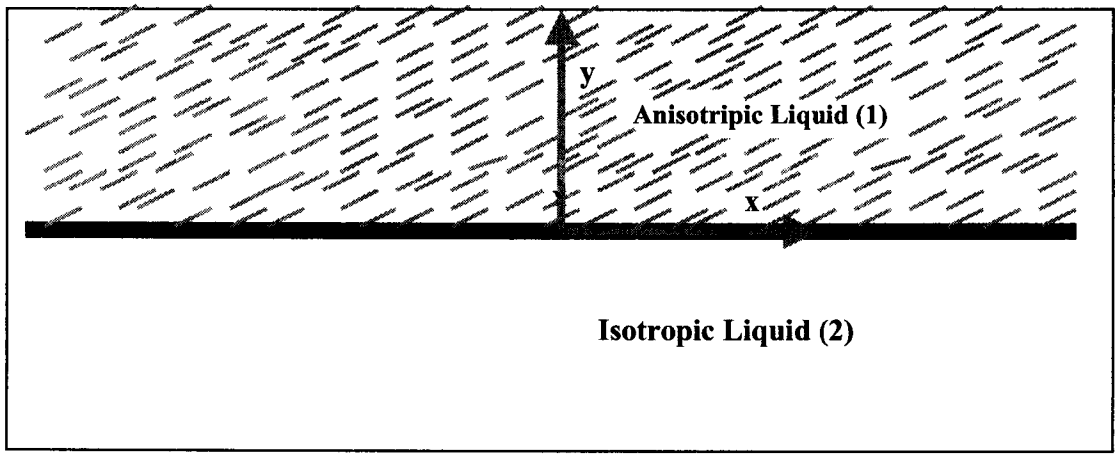

Fig. 5.4: Cartesian coordinate system showing oblique orientation of nematic molecules.

$$\left(\varepsilon_{\perp}+\frac{\sigma}{i\omega}\right)\nabla^2\phi+\varepsilon_a n_i^0 n_k^0\frac{\partial^2\phi}{\partial x_i\partial x_k}=0 \tag{5.33}$$

In the coordinate system shown in Fig. 5.4, the equations for electric potential are as follows:

Nematic phase: $\left(\varepsilon_{\perp}+\frac{\sigma}{i\omega}\right)\nabla^2\phi_1+\varepsilon_a n_x^0 n_y^0\frac{\partial^2\phi_1}{\partial x\partial y}=0$ (5.34)

Isotropic phase: $\nabla^2\phi_2=0$ (5.35)

The solutions of Eqs. (5.34) and (5.35) are:

$$\phi_1=A_1x+B_1y+C_1z+\phi_{10} \tag{5.36}$$

$$\phi_2=A_2x+B_2y+C_2z+\phi_{20} \tag{5.37}$$

with the boundary conditions:

(1) $(\boldsymbol{D}_2-\boldsymbol{D}_1).\boldsymbol{u}_n=0$ [$\boldsymbol{u}_n$ is the unit normal to the interface].

$$\left\{\varepsilon_{\perp}+\frac{\sigma_2}{i\omega}\right\}E_1(y=0)+\varepsilon_a n_y^0\left(\boldsymbol{n}^0.\boldsymbol{E}_1(y=0)\right)=\left\{\varepsilon_1+\frac{\sigma_1}{i\omega}\right\}E_2(y=0) \tag{5.38}$$

(2,3) $(\boldsymbol{E}_2-\boldsymbol{E}_1).\boldsymbol{u}_t=0$ [$\boldsymbol{u}_t$ is the unit tangent to the interface].

$$E_{1x}(y=0)=E_{2x}(y=0)\quad and\quad E_{1z}(y=0)=E_{2z}(y=0) \tag{5.39}$$

(4) $\phi_1(y=0)=\phi_2(y=0)$ (5.40)

(5-10) $as\ \boldsymbol{r}\to\infty,\quad -\nabla\phi_1=\boldsymbol{E}_1^{\infty}$ and $-\nabla\phi_2=\boldsymbol{E}_2^{\infty}$ (5.41)

Therefore, the two potentials are:

$$\phi_1=-E_x^{\infty}x-E_{1y}^{\infty}y-E_z^{\infty}z+\phi_0 \tag{5.42}$$

$$\phi_2=-E_x^{\infty}x-E_{2y}^{\infty}y-E_z^{\infty}z+\phi_0 \tag{5.43}$$

with E_{1y}^{∞} and E_{2y}^{∞} related as:

$$\left\{\varepsilon_{\perp}+\frac{\sigma_2}{i\omega}\right\}E_{1y}^{\infty}+\varepsilon_a n_y^0\left(n_x^0E_x^{\infty}+n_y^0E_{1y}^{\infty}+n_z^0E_z^{\infty}\right)=\left\{\varepsilon_1+\frac{\sigma_1}{i\omega}\right\}E_{2y}^{\infty} \tag{5.44}$$

where $E_x^{\infty}=E_{2x}^{\infty}, E_{2y}^{\infty}$ and $E_z^{\infty}=E_{2z}^{\infty}$ are known quantities. It may be noted that the far-field electric fields are different for the two phases.

5.6.2 Director Perturbation

Assume that the LC molecules are arranged obliquely initially $\left(n_1^0,n_2^0,0\right)$, as shown in fig. 5.4, but the applied electric field $(E_1,E_2,0)$ and associated flow field perturbs them. The governing equations for the director perturbation $(u_1,u_2,0)$ are obtained by inserting Eqs. (5.24), (5.23) and (5.17) in Eq. (5.16):

$$\gamma_1\frac{\partial u_1}{\partial t}=\left(K_3n_2^0n_2^0+K_1n_1^0n_1^0\right)\frac{\partial^2u_1}{\partial y^2}+PE_1-Pn_1^0\left(n_1^0E_1+n_2^0E_2\right) \tag{5.45}$$

$$\gamma_1\frac{\partial u_2}{\partial t}=\left(K_3n_2^0n_2^0+K_1n_1^0n_1^0\right)\frac{\partial^2u_2}{\partial y^2}+PE_2-Pn_2^0\left(n_1^0E_1+n_2^0E_2\right) \tag{5.46}$$

The facts that $\varepsilon_0\varepsilon_a\left(n_pE_p\right)E_i<<PE_i$ as E itself is a very small number, and $\left(\gamma_1+\gamma_2\right)A_{21}<<PE$ (to be justified letter) have been utilized in formulating Eqs. (5.45) and (5.46). The second assumption decouples director perturbation from the flow field. Since there is no forcing field in the third direction, u_3 is identically zero. The form of forcing field,

$$E_i(y,t)=E_{i0}(y)e^{i\omega t} \qquad (i=1,2) \tag{5.47}$$

suggests a solution of the form

$$u_i(y,t)=u_{i0}(y)e^{i\omega t} \qquad (i=1,2) \tag{5.48}$$

Using the boundary conditions that $u_{10}(y=0)=0=u_{20}(y=0)$ and $u_{10}(y)$ and $u_{20}(y)$ are finite as $y\to\infty$, the solutions of Eqs. (5.45) and (5.46) are

$$u_1(y,t)=\frac{PE_{10}-Pn_1^0\left(n_1^0E_{10}+n_2^0E_{20}\right)}{\gamma_1 i\omega}\left(1-e^{-\vartheta(1+i)y}\right)e^{i\omega t} \tag{5.49}$$

$$u_2(y,t)=\frac{PE_{20}-Pn_2^0\left(n_1^0E_{10}+n_2^0E_{20}\right)}{\gamma_1 i\omega}\left(1-e^{-\vartheta(1+i)y}\right)e^{i\omega t} \tag{5.50}$$

where, $\vartheta=\sqrt{\dfrac{\gamma_1\omega}{2\left(K_3n_2^0n_2^0+K_1n_1^0n_1^0\right)}}$ is the inverse nematic orientation length scale. One important observation from Eqs. (5.49) and (5.50) is that u_1 is identically zero when $n_1^0=1$, and u_2 is identically zero when $n_2^0=1$. This is merely a consequence of the constraint given by Eq. (5.18). The above solution is valid everywhere provided $\boldsymbol{u}.\boldsymbol{u}<<1$. Close to the interface, the strong anchoring boundary condition assures that $\boldsymbol{u}.\boldsymbol{u}<<1$ is always satisfied. Away from the interface, however, only the electric field is dominant, as the effect of anchoring cannot be felt far away from the interface. When the frequency of the applied field is very small, deformations in the liquid crystalline phase away from the boundary tend to be large. This means that there is a range of frequencies where the solutions given by Eqs. (5.49) and (5.50) are not applicable.

To determine the frequency range for the applicability of Eqs. (5.49) and (5.50), let us consider a 1-D problem with initial configulation $(0,1,0)$ and applied electric field $(E_0,0,0)$. Far from the interface, only the electric field is relevant, since the surface effects cannot be felt. For this case, the real part of the far-field director perturbation is given by Eq. (5.49) as

$$u_\infty(t)=\frac{PE_0}{\gamma_1}\frac{\sin\omega t}{\omega} \tag{5.51}$$

The mean square value of far field director perturbation is

$$\left\langle u_\infty^2(t)\right\rangle=\frac{P^2E_0^2}{\gamma_1^2}\left\langle\frac{\sin^2\omega t}{\omega^2}\right\rangle=\frac{P^2E_0^2}{\gamma_1^2}\frac{\int_0^{2\pi/\omega}\frac{\sin^2\omega t}{\omega^2}dt}{2\pi/\omega}=\frac{P^2E_0^2}{2\gamma_1^2}\frac{1}{\omega^2} \tag{5.52}$$

For our solution to be valid, the mean square perturbation must be much less than unity; i.e.,

$$\left\langle u_\infty^2(t)\right\rangle<<1\Rightarrow\frac{P^2E_0^2}{2\gamma_1^2}\frac{1}{\omega^2}<<1\Rightarrow\omega^2>>\frac{P^2E_0^2}{2\gamma_1^2}\Rightarrow\omega>>\frac{PE_0}{\sqrt{2}\,\gamma_1} \tag{5.53}$$

Therefore, the solution of the director perturbation, given by Eqs. (5.49) and (5.50), is valid only when

$$\omega>>\frac{PE_0}{\sqrt{2}\,\gamma_1}. \tag{5.54}$$

5.6.3 Flow field

To determine the flow field, let us assume that the planar interface has a velocity $v_0e^{i\omega t}$ that is unknown. The only non-zero component of velocity is v_1, with a governing equation

$$\frac{\partial}{\partial t}\left(\alpha_3 n_1^0\frac{\partial u_2}{\partial y}+\alpha_2 n_2^0\frac{\partial u_1}{\partial y}\right)+\alpha\frac{\partial^2 v_1}{\partial y^2}=\rho\frac{\partial v_1}{\partial t} \tag{5.55}$$

where $\alpha=2\alpha_1 n_1^0 n_1^0 n_2^0 n_2^0+(\alpha_5-\alpha_2)n_2^0 n_2^0+(\alpha_3+\alpha_6)n_1^0 n_1^0+\alpha_4$ (5.56)

Substituting $v_1(y,t) = v_{10}(y)e^{i\omega t}$, and solving by the method of a homogenous solution and a particular solution, we obtain

$$v_{10}(y) = Be^{-\zeta y}(\cos\zeta y - i\sin\zeta y) - \frac{(1+i)\Pi}{\vartheta^2 - \zeta^2}\frac{\vartheta\omega}{2\alpha}e^{-\vartheta y}(\cos\vartheta y - i\sin\vartheta y) \tag{5.57}$$

$$\text{with } \zeta = \sqrt{\frac{\rho\omega}{2\alpha}} \text{ and } \Pi = \frac{P}{\gamma_1 i\omega}\left(n_1^0 E_{20} - n_2^0 E_{10}\right)\left(\alpha_3 n_1^0 n_1^0 - \alpha_2 n_2^0 n_2^0\right) \tag{5.58}$$

The no slip boundary condition at the interface, $v_{10}(y=0) = v_0$, gives

$$B = v_0 + \frac{(1+i)\Pi}{\vartheta^2 - \zeta^2}\frac{\vartheta\omega}{2\alpha} \tag{5.59}$$

5.6.4 Flow and orientation length scales

The values of physical parameters for 5CB are

$\gamma_1 = 0.081\ Pa.s$ (Skarp *et* al., 1980).

$p = 7.1\ D = 2.37x10^{-29}\ Cm$ (Clarke *et al.*, 1997)

$P = Np = 0.057591\,\text{C/m}^2$ (Calculation)

$E_0 = 3700\ V/m$ (Experimental)

$\alpha_1 = -0.111\,P \quad \alpha_2 = -0.939\,P \quad \alpha_3 = -0.129\,P$
$\alpha_4 = 0.748\,P \quad \alpha_5 = 0.906\,P \quad \alpha_6 = -0.162\,P$ (Stark, 1999)

$K_1 = 15\ pN \quad K_2 = 10\ pN \quad K_3 = 65\ pN$ (Zakharov and Dong, 2001)

Our solution for director perturbation and flow field is therefore valid for frequencies larger than $PE_0/(\sqrt{2}\,\gamma_1) = 1860$ rad/s = 296 Hz, which is within the range of experimental interest.

For $n_1^0 = n_2^0 = 1/\sqrt{2}$, these parameters give

$$\alpha = 2\left(2\alpha_1 n_1^0 n_1^0 n_2^0 n_2^0 + (\alpha_5 - \alpha_2) n_2^0 n_2^0 + (\alpha_3 + \alpha_6) n_1^0 n_1^0 + \alpha_4\right) = 0.34565 \ Pa.s$$

$$\zeta = \sqrt{\frac{\rho\omega}{\alpha}} = \sqrt{\frac{1008\ kg/m^3 \text{ x } 1860\ rad/s}{0.34565\ Pa.s}} = 2525 \frac{1}{\text{m}}$$

$$\vartheta = \sqrt{\frac{0.081\ Pa.s \text{ x } 1860\ rad/s}{2\left(65x10^{-12} x0.5 + 15x10^{-12} x0.5\right)N}} = 1372315 \frac{1}{\text{m}}$$

The flow length scale is $\zeta^{-1} \sim 396\ \mu m$, while the orientation length scale is $\vartheta^{-1} \sim 728\ nm$. The values of both length scales are in the expected range.

5.6.5 Stresses at the boundary:

The kinematic variables of this problem are

$$A_{21}\big|_{y=0} = \left.\frac{\partial v_1}{\partial y}\right|_{y=0} \tag{5.60}$$

$$N_1^0\big|_{y=0} = \left.\frac{\partial u_1}{\partial t}\right|_{y=0} - n_2^0 A_{21}\big|_{y=0} = 0 - n_2^0 A_{21}\big|_{y=0} \tag{5.61}$$

$$N_2^0\big|_{y=0} = \left.\frac{\partial u_2}{\partial t}\right|_{y=0} + n_1^0 A_{21}\big|_{y=0} = 0 + n_1^0 A_{21}\big|_{y=0} \tag{5.62}$$

$$N_3^0 = \frac{\partial u_3}{\partial t} = 0 \tag{5.63}$$

The components of the stress tensor at the interface ($y = 0$) calculated from Eq. (5.15) and expressed in terms of kinematic variable are

$$\begin{aligned}
\sigma_{11} &= 2\alpha_1 n_1^0 n_2^0 A_{21} n_1^0 n_1^0 + (\alpha_2 + \alpha_3) N_1^0 n_1^0 + \alpha_5 n_1^0 n_2^0 A_{21} + \alpha_6 n_1^0 n_2^0 A_{21} \\
\sigma_{21} &= 2\alpha_1 n_1^0 n_2^0 A_{21} n_2^0 n_1^0 + \alpha_2 n_2^0 N_1^0 + \alpha_3 N_2^0 n_1^0 + \alpha_4 A_{21} + \alpha_5 n_2^0 n_2^0 A_{21} + \alpha_6 n_1^0 n_1^0 A_{12} \\
\sigma_{12} &= 2\alpha_1 n_1^0 n_2^0 A_{21} n_1^0 n_2^0 + \alpha_2 n_1^0 N_2^0 + \alpha_3 N_1^0 n_2^0 + \alpha_4 A_{21} + \alpha_5 n_1^0 n_1^0 A_{12} + \alpha_6 n_2^0 n_2^0 A_{21} \\
\sigma_{22} &= 2\alpha_1 n_1^0 n_2^0 A_{21} n_2^0 n_2^0 + (\alpha_2 + \alpha_3) N_2^0 n_2^0 + \alpha_5 n_2^0 n_1^0 A_{12} + \alpha_6 n_2^0 n_1^0 A_{12} \\
\sigma_{31} &= \sigma_{32} = \sigma_{13} = \sigma_{23} = \sigma_{33} = 0
\end{aligned} \tag{5.64}$$

Note that both the first and the second normal stress differences are non-zero.

5.6.6 Flow Field in isotropic phase

It must be pointed out that the amplitude of the velocity of the interface, v_0, is still an unknown quantity. In order to calculate the flow-field in the isotropic phase, we must require that the velocity and the shear stress at the interface ($y = 0$) be continuous. The second criterion will give us the interface velocity.

In the coordinate system of Fig. 5.4, the only non-zero component of velocity in either phase is v_x, which is expected to be a function of y and t only:

$$\mathbf{v}(x,\mathrm{t}) = (\mathrm{v}_1(y,t),0,0) \tag{5.65}$$

LC Phase (1):

The velocity in the liquid crystalline phase is given by Eq. (5.57):

$$\mathrm{v}_{10}(y) = Be^{-\zeta(1+i)y} - \frac{(1+i)\Pi}{\vartheta^2 - \zeta^2}\frac{\vartheta\omega}{2\alpha}e^{-\vartheta(1+i)y} \tag{5.66}$$

The corresponding shear rate at the interface is

$$A_{21}(y=0) = \left.\frac{\partial \mathrm{v}_{10}(y)}{\partial y}\right|_{y=0} = v_0(-\zeta)(1+i) + i\frac{\Pi}{\vartheta+\zeta}\frac{\vartheta\omega}{\alpha} \tag{5.67}$$

This gives rise to shear stress at the boundary given by

$$\tau_{1yx}\big|_{y=0} = \alpha A_{21}\big|_{y=0} \tag{5.68}$$

Isotropic Phase (2):

The governing equation for the velocity is

$$\rho\frac{\partial \mathrm{v}_{2x}}{\partial t} = \mu\frac{\partial^2 \mathrm{v}_{2x}}{\partial y^2} \tag{5.69}$$

This gives rise to a solution by the method of separation of variables as

$$v_{2x}(y,t) = Ae^{\sqrt{\frac{\rho_2\omega}{2\mu_2}}(1+i)y} e^{i\omega t} \tag{5.70}$$

Therefore, the shear stress is

$$\tau_{2yx} = \mu_2 \frac{\partial v_x}{\partial y} = \sqrt{\frac{\rho_2\omega}{2\mu_2}}(1+i)\mu_2 Ae^{\sqrt{\frac{\rho_2\omega}{2\mu_2}}(1+i)y} e^{i\omega t} \tag{5.71}$$

Matching the velocity at the interface yields $A = v_0$, and requiring the stress be continuous at the interface provides the unknown velocity of the interface:

$$v_0 = \alpha\left\{\frac{\Pi}{\vartheta+\zeta}\frac{\vartheta\omega}{\alpha}\frac{i}{1+i}\right\}\Bigg/\left\{\mu_2\sqrt{\frac{\rho_2\omega}{2\mu_2}} + \alpha\zeta\right\} \tag{5.72}$$

Note that v_0 is a complex number. For this solution to be correct, we need to justify the earlier assumption that $(\gamma_1+\gamma_2)A_{21} << PE_0$. It is sufficient to show that $(\gamma_1+\gamma_2)|A_{21}|_{\max} << |PE_0|$. The magnitude of shear rate is maximum at $y = 0$. Using Eqs. (5.67) and (5.58)

$$A_{21}(y=0) = v_0(-\zeta)(1+i) + \frac{P}{\gamma_1\omega}\left(n_1^0E_{20} - n_2^0E_{10}\right)\left(\alpha_3 n_1^0 n_1^0 - \alpha_2 n_2^0 n_2^0\right)\frac{1}{\vartheta+\zeta}\frac{\vartheta\omega}{\alpha} \tag{5.73}$$

$$(\gamma_1+\gamma_2)|A_{21}(y=0)| = 1.102 << PE_0 = 213.087$$

Therefore, the assumption of $(\gamma_1+\gamma_2)A_{21} << PE$ in section 5.6.2 is justified.

5.6.7 Decaying Polarization

The assumption of constant polarization throughout the droplet certainly breaks down in the core of the droplet, where molecular dipoles are free to rotate and translate, and therefore the dipoles will always arrange so as to cancel the charge polarization of the individual rods. The macroscopic polarization is then zero. The presence of an

interface, however, serves to reduce the symmetry of a liquid crystal system because the interaction between the interface and liquid crystal molecules near it eliminates the translational and rotational degeneracy of the bulk molecules. The restricted rotation and translation of the liquid crystals in the interfacial region gives rise to a finite macroscopic polarization. The polarization is maximum at the interface and it decays to zero over a certain length scale. When polarization has exponential decay with distance from the interface in the form $P = P_0 e^{-ky}$, where k^{-1} is the characteristic polarization decay length scale, y is the distance from the interface, and P_0 is the value of macroscopic polarization at the interface, the amplitude interface velocity can be easily computed in the foregoing manner to be

$$v_0 = \alpha \left\{ \frac{\Pi_k}{\vartheta + \zeta} \frac{\vartheta \omega}{\alpha} \frac{i}{1+i} + \frac{\Pi_k ki\omega}{\alpha k^2 - \rho i \omega} \left(\zeta - \frac{k}{i+1} \right) \right\} \Bigg/ \left\{ \mu_2 \sqrt{\frac{\rho_2 \omega}{2\mu_2}} + \alpha \zeta \right\} \tag{5.74}$$

$$\text{where, } \Pi_k = \frac{P_0}{\gamma_1 i\omega - k^2 K} \left(n_1^0 E_{20} - n_2^0 E_{10} \right) \left(\alpha_3 n_1^0 n_1^0 - \alpha_2 n_2^0 n_2^0 \right) \tag{5.75}$$

When $k = 0$, Eq. (5.74) reduces to Eq. (5.72) as expected.

5.6.8 Displacement and Strain at the Interface

Displacement is the integral of velocity with respect to time. The integral of the interface velocity is $v_0 e^{i\omega t} / (i\omega)$. From this result, the real part of the displacement and the rms value of the displacement can be easily calculated. This task is straightforward in principle, but algebraically complicated as v_0 is also a complex number. In order to convert displacement to dimensionless strain, we must divide by a length scale. The most relevant length scale for this purpose is the flow length scale, ζ^{-1}; the strain defined in

this way is denoted by γ_1. Alternatively, the velocity gradient at the interface can be divided by frequency to obtain the strain, and the rms value of the real part can be computed. The strain defined in this manner is denoted by γ_2.

5.6.9 Discussion

Figure 5.5 shows the velocity of the interface and the strain at the interface of the droplet for $k = 10000\, m^{-1}$. The magnitude of the interfacial velocity decreases with frequency. Consequently, strain decreases with frequency. The decay of strain with frequency is consistent with the intuition that a slow field will cause a large deformation, while the droplet cannot respond to a fast field. A strain of 1% at 1000 rad/s is significant; rheological measurements are routinely done at a strain of 1%, and it is quite possible that dielectric measurements would be affected by a strain of this magnitude. This is coherent with the shift of the loss peak in dielectric measurements around this frequency. This choice of polarization decay length scale, however, is unrealistic. $k = 10000\, m^{-1}$ corresponds to a polarization decay length of 50,000 molecular lengths, which is quite large. A reasonable decay length would be roughly 10 molecular lengths; since the 5CB molecule is roughly 20 A^o, this gives $k = 5 \times 10^7\ m^{-1}$. Figure 5.6 shows the strain calculation based on this value of larger k; this strain is probably too small to have any effect on the dielectric measurement.

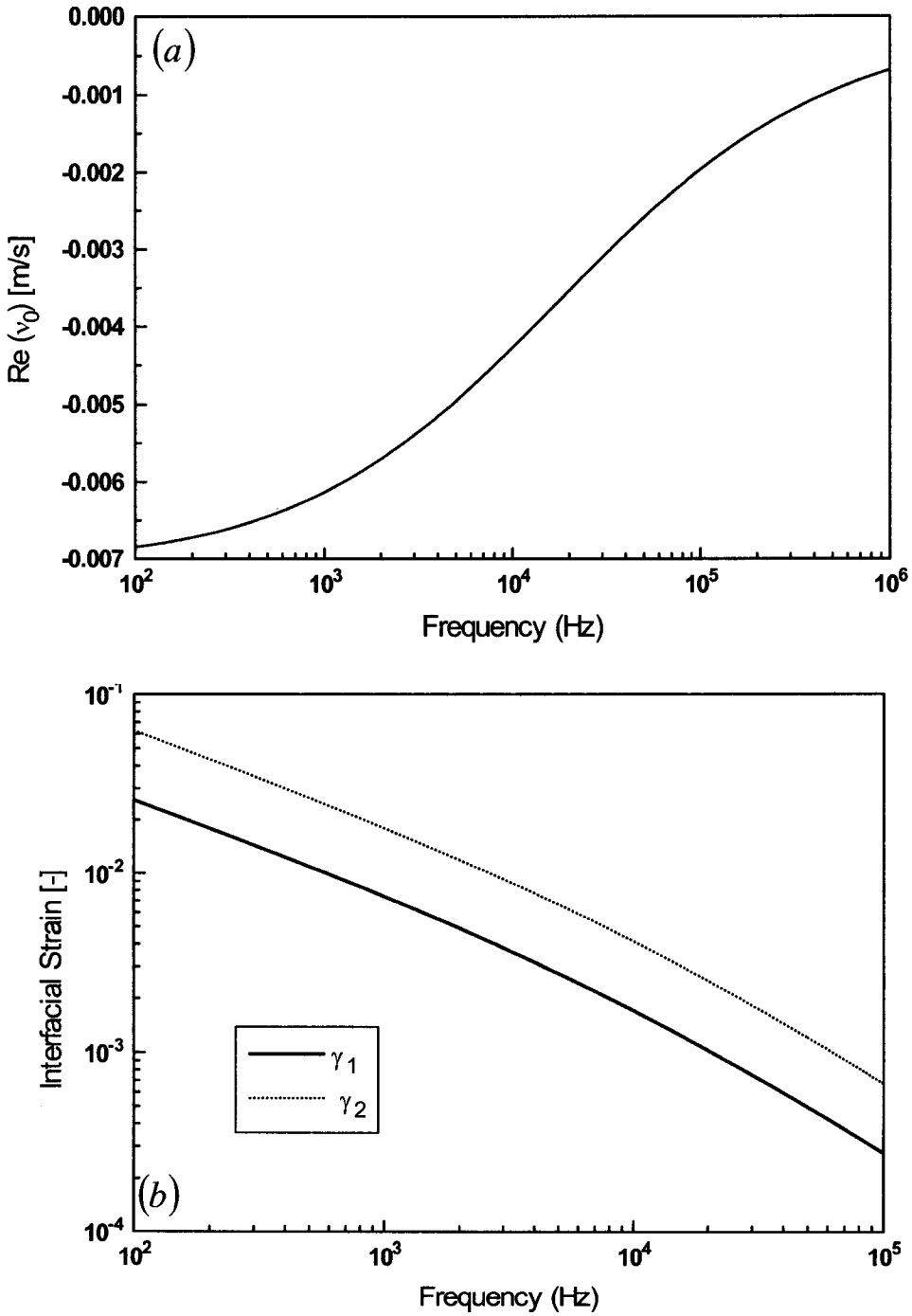

Fig 5.5: The real parts of (a) the interface velocity, and (b) the interfacial strain for a polarization decay length of 100 microns when $\boldsymbol{n}^0 = (0.6, 0.8, 0)$ and $\boldsymbol{E} = (2616, 2616, 0)$V/m.

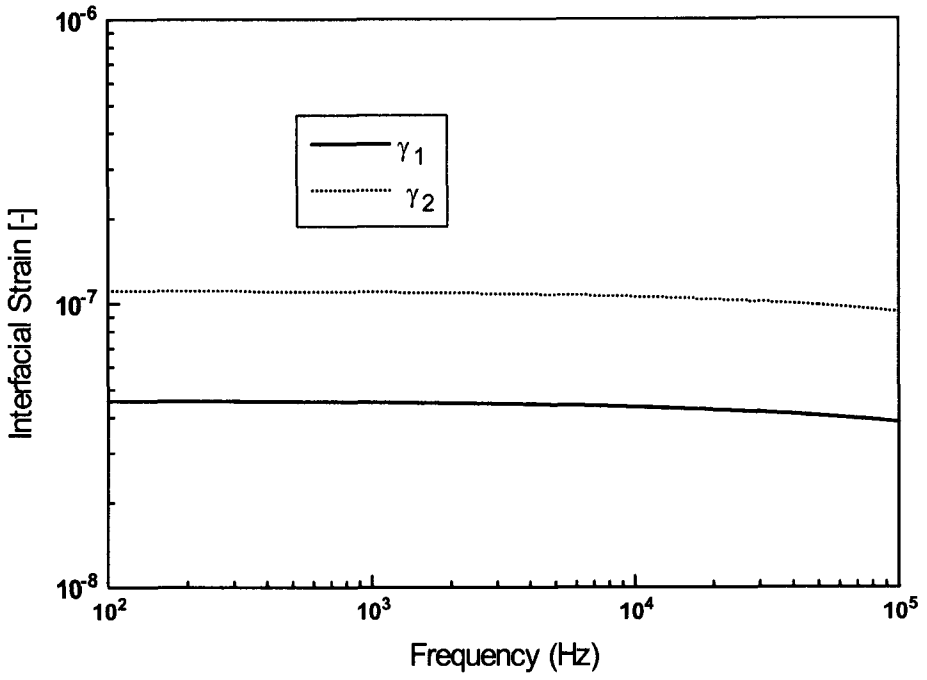

Fig. 5.6: The real part of the interfacial strain for a polarization decay length of 0.02 microns when $\boldsymbol{n}^0 = (0.6, 0.8, 0)$ and $\boldsymbol{E} = (2616, 2616, 0)$ V/m.

5.7 Spherical Geometry with Uniform Radial Initial Configuration

While planar calculations show frequency dependence of the deformation of the droplet, they are unable to predict a realistic absolute value of the deformation. One key feature missing in the planar approximation of the interface is the effect of curvature of the interface. In this section we will develop the governing equations for the dynamics of fluctuations in the radial director field of a spherical nematic droplet with rigid homeotropic anchoring under the influence of an applied alternating electric field. We examine the analytical solution of the governing equation for a very large spherical droplet.

For a uniaxial initial configuration $\left(n_1^0,0,0\right)$, using spherical coordinates (r,θ,ϕ) with the origin at the center of the droplet,

$$\nabla \boldsymbol{n}^0 = \boldsymbol{e}_\theta \frac{n_r^0}{r}\boldsymbol{e}_\theta + \boldsymbol{e}_\phi \frac{n_r^0}{r}\boldsymbol{e}_\phi \tag{5.76}$$

$$\nabla.\boldsymbol{n}^0 = \frac{2n_r^0}{r}, \quad and \quad \nabla \times \boldsymbol{n}^0 = 0 \tag{5.77}$$

$\boldsymbol{e}_\theta$ and $\boldsymbol{e}_\phi$ are unit vectors along $\theta-$ and $\phi-$ directions, respectively.

Such a purely radial configuration will be allowed in equilibrium only if the total energy is finite. The elastic free energy density of a perfectly radial nematic droplet is given by

$$2W_g^0 = K_1\left(n_{a,a}^0\right)^2 + K_2\left(\varepsilon_{abc}n_a^0 n_{c,b}^0\right)^2 + K_3 n_b^0 n_{a,b}^0 n_c^0 n_{a,c}^0 = 4K_1\frac{1}{r^2} \tag{5.78}$$

Thus, the energy per unit volume has a singularity at the center of the droplet. The energy, however, which is equal to $\int\frac{4\pi r^2 dr}{r^2} \sim \int dr$, is finite in any region in space.

Therefore, the perfectly radial configuration of nematogens in a spherical droplet is permissible. This is in contrast to the fact that the uniform radial orientation of molecules in a cylindrical geometry is not permissible.

This uniform radial configuration of the molecules is perturbed infinitesimally by the applied electric field $(E_r, E_\theta, 0)$. Let the small perturbation of the director be $\boldsymbol{u}$ such that $\boldsymbol{n} = \boldsymbol{n}^0 + \boldsymbol{u}$. Since there is no variation of the forcing field in the $\phi-$direction, we assume no $\phi-$dependence.

Let us define non-dimensional variables $\xi = \frac{r}{R}$ and $\zeta = \omega t$. K denotes a number with the dimensions of the Frank elastic constants. The governing equations for the director perturbation are

$$u_r = 0 \tag{5.79}$$

$$\frac{\partial u_\theta}{\partial \zeta} = \frac{K}{R^2 \gamma_1 \omega}\left\{\begin{array}{l} \frac{K_3}{K}\frac{\partial^2 u_\theta}{\partial \xi^2} + \frac{K_3}{K}\frac{\partial}{\partial \xi}\left(\frac{u_\theta}{\xi}\right) + \frac{K_1}{K}\frac{1}{\xi^2}\frac{\partial^2 u_\theta}{\partial \theta^2} \\ + \frac{K_3}{K}\left(\frac{1}{\xi}\frac{\partial u_\theta}{\partial \xi}\right) + \frac{K_3}{K}\left(\frac{1}{\xi}\frac{u_\theta}{\xi}\right) \\ + \frac{K_1}{K}\frac{1}{\xi^2}\frac{\partial}{\partial \theta}\left(\frac{u_\theta}{\tan\theta}\right) + 2\frac{K_1}{K}\frac{u_\theta}{\xi^2} \end{array}\right\} + \frac{PE_\theta}{\gamma_1 \omega} \tag{5.80}$$

$$u_\phi = 0 \tag{5.81}$$

The differential equation for u_θ is very difficult to be solved exactly, due to its non-linearity. Nonetheless, the presence of small parameter $\varepsilon = K/(R^2\gamma_1\omega)$, for the large radius of droplet radius R, makes it possible to use perturbation techniques to obtain a good approximation to the solution. The basic strategy is to obtain a solution valid for $\varepsilon = 0$ and then to add correction terms to account for the fact that ε is not identically

zero, but merely small. This procedure replaces the original problem by a sequence of smaller ones. Perturbation problems may be *regular* or *singular*, depending on what happens for $\varepsilon = 0$. For the problem at hand, we need to have both kinds of perturbation.

5.7.1 Regular Perturbation Analysis

For the case of very small ε (i.e., $\varepsilon << 1$), using a Maclaurin series to express the dependence of the solution u on ε yields

$$u_\theta = u_0 + \varepsilon u_1 + \varepsilon^2 u_2 + O(\varepsilon^3) \tag{5.82}$$

where $u_0, u_1, \text{and } u_2$ are coefficients of expansion and $O(\varepsilon^3)$ denotes terms of the *mathematical order* of ε^3. The problem now is to determine the coefficient functions, $u_n(\zeta, \xi)$. Substituting Eq. (5.82) in Eq. (5.80), and comparing the terms of different orders of ε on left-hand side and right-hand side of equation, we obtain

Terms of the order of ε^0: $$\frac{\partial u_0}{\partial \zeta} = \frac{PE_\theta}{\gamma_1 \omega} \tag{5.83a}$$

Terms of the order of ε^1: $$\frac{\partial u_1}{\partial \zeta} = \left(-\frac{K_1}{K}\frac{1}{\sin^2\theta} + 2\frac{K_1}{K} \right)\frac{u_0}{\xi^2} \tag{5.83b}$$

Terms of the order of ε^2:

$$\frac{\partial u_2}{\partial \zeta} = \left\{ \begin{array}{l} \dfrac{K_3}{K}\dfrac{\partial^2 u_1}{\partial \xi^2} + \dfrac{K_3}{K}\dfrac{\partial}{\partial \xi}\left(\dfrac{u_1}{\xi}\right) + \dfrac{K_1}{K}\dfrac{1}{\xi^2}\dfrac{\partial^2 u_1}{\partial \theta^2} + \dfrac{K_3}{K}\left(\dfrac{1}{\xi}\dfrac{\partial u_1}{\partial \xi}\right) \\ + \dfrac{K_3}{K}\left(\dfrac{u_1}{\xi^2}\right) + \dfrac{K_1}{K}\dfrac{1}{\xi^2}\dfrac{\partial}{\partial \theta}\left(\dfrac{u_1}{\tan\theta}\right) + 2\dfrac{K_1}{K}\dfrac{u_1}{\xi^2} \end{array} \right\} \tag{5.83c}$$

The solutions of Eqs. (5.83a) and (5.83b) require no spatial boundary condition. Hence, these solutions are valid only far away from the interface. The solution is

$$u_o(\xi,\zeta) = -i\frac{PE_{\theta 0}}{\gamma_1 \omega} e^{i\zeta} - \varepsilon \frac{\beta}{\xi^2} e^{i\zeta} + O(\varepsilon^2) \tag{5.84}$$

where $\beta = \left(-\frac{K_1}{K}\frac{1}{\sin^2\theta} + 2\frac{K_1}{K} \right)\frac{PE_{\theta 0}}{\gamma_1 \omega}$. This is the *outer solution*, valid outside thin boundary layer.

5.7.2 Singular Perturbation Analysis

Since the small parameter ε multiplies the highest-order term (i.e., the highest derivative), setting $\varepsilon = 0$ reduces the order of the Eq. (5.80). This reduction of order is sufficient to invalidate a regular perturbation expansion. The fact that ε multiplies the highest derivative is an immediate indication that the perturbation problem is singular.

If we set $\varepsilon = 0$, the differential equation reduces to $\frac{\partial u_\theta}{\partial \zeta} = \frac{PE_\theta}{\gamma_1 \omega}$. Although accurate for the core region in the center of the droplet, this approximation is obviously incorrect near the interface. The solution to this equation cannot satisfy the boundary condition that u_θ be exactly zero at the surface. The message here is that whereas ξ in Eq. (5.80) is scaled adequately for the core region, a different variable is needed in the boundary layer. To rescale the radial coordinate for the boundary layer, let

$$\eta = (1-\xi)\varepsilon^b \tag{5.85}$$

The quantity $(1-\xi)$, which is small in the boundary layer, is "stretched" using the factor ε^b to obtain a coordinate $O(1)$. That is, $\eta = O(1)$ in the boundary layer. Because ε is small, making the stretching factor large will require $b < 0$.

$$\xi = 1 - \eta\varepsilon^{-b} \tag{5.86a}$$

$$\frac{\partial}{\partial \xi} = -\frac{1}{\varepsilon^{-b}}\frac{\partial}{\partial \eta} = -\varepsilon^b \frac{\partial}{\partial \eta} \tag{5.86b}$$

$$\frac{\partial}{\partial\xi}\left(\frac{\partial}{\partial\xi}\right)=\varepsilon^{2b}\frac{\partial}{\partial\eta^2} \tag{5.86c}$$

Changing to the new independent variable, Eq. (5.80) becomes

$$\frac{\partial u_\theta}{\partial\zeta}=\left\{\begin{array}{l}\varepsilon^{2b+1}\dfrac{K_3}{K}\dfrac{\partial^2 u_\theta}{\partial\eta^2}-\varepsilon^{b+1}\dfrac{K_3}{K}\dfrac{\partial}{\partial\eta}\left(\dfrac{u_\theta}{\left(1-\eta\varepsilon^{-b}\right)}\right)-\varepsilon^{b+1}\dfrac{K_3}{K}\dfrac{1}{\left(1-\eta\varepsilon^{-b}\right)}\dfrac{\partial u_\theta}{\partial\eta}\\ +\varepsilon\dfrac{K_3}{K}\left(\dfrac{u_\theta}{\left(1-\eta\varepsilon^{-b}\right)^2}\right)+\varepsilon\dfrac{K_1}{K}\dfrac{1}{\left(1-\eta\varepsilon^{-b}\right)^2}\dfrac{\partial}{\partial\theta}\left(\dfrac{u_\theta}{\tan\theta}\right)\\ +2\varepsilon\dfrac{K_1}{K}\dfrac{u_\theta}{\left(1-\eta\varepsilon^{-b}\right)^2}+\varepsilon\dfrac{K_1}{K}\dfrac{1}{\left(1-\eta\varepsilon^{-b}\right)^2}\dfrac{\partial^2 u_\theta}{\partial\theta^2}+\dfrac{PE_\theta}{\gamma_1\omega}\end{array}\right\} \tag{5.87}$$

Given that $\eta\varepsilon^{-b}$ will be small in the boundary layer (i.e., $b<0$), the coefficient of the first derivative can be simplified using an expansion of the form

$$1/(1-x)=1+x+O(x^2)\ for\quad x\to 0.$$
$$1/(1-x)^2=1+2x+O(x^2)\ for\quad x\to 0$$

This expansion yields

$$\frac{\partial u_\theta}{\partial\zeta}=\left\{\begin{array}{l}\varepsilon^{2b+1}\dfrac{K_3}{K}\dfrac{\partial^2 u_\theta}{\partial\eta^2}-\varepsilon^{b+1}\dfrac{K_3}{K}\dfrac{\partial}{\partial\eta}\left(u_\theta\left(1+\eta\varepsilon^{-b}\right)\right)-\varepsilon^{b+1}\dfrac{K_3}{K}\left(1+\eta\varepsilon^{-b}\right)\dfrac{\partial u_\theta}{\partial\eta}\\ +\varepsilon\dfrac{K_3}{K}\left(u_\theta\left(1+2\eta\varepsilon^{-b}\right)\right)+\varepsilon\dfrac{K_1}{K}\left(1+2\eta\varepsilon^{-b}\right)\dfrac{\partial}{\partial\theta}\left(\dfrac{u_\theta}{\tan\theta}\right)\\ +2\varepsilon\dfrac{K_1}{K}u_\theta\left(1+2\eta\varepsilon^{-b}\right)+\varepsilon\dfrac{K_1}{K}\left(1+2\eta\varepsilon^{-b}\right)\dfrac{\partial^2 u_\theta}{\partial\theta^2}+\dfrac{PE_\theta}{\gamma_1\omega}\end{array}\right\} \tag{5.88}$$

The required value of b is determined by the dominant balance. The equation must remain second order, and this requires $2b+1=0$, or $b=-1/2$. Thus, the boundary layer coordinate is $\eta=(1-\xi)\varepsilon^{-1/2}$ and the corresponding director balance equation is

$$\frac{\partial u_\theta}{\partial \zeta} = \left\{ \begin{array}{l} \frac{K_3}{K}\frac{\partial^2 u_\theta}{\partial \eta^2} - \varepsilon^{1/2}\frac{K_3}{K}\frac{\partial}{\partial \eta}\left(u_\theta\left(1+\eta\varepsilon^{1/2}\right)\right) - \varepsilon^{1/2}\frac{K_3}{K}\left(1+\eta\varepsilon^{1/2}\right)\frac{\partial u_\theta}{\partial \eta} \\ +\varepsilon\frac{K_3}{K}\left(u_\theta\left(1+2\eta\varepsilon^{1/2}\right)\right) + \varepsilon\frac{K_1}{K}\left(1+2\eta\varepsilon^{1/2}\right)\frac{\partial}{\partial\theta}\left(\frac{u_\theta}{\tan\theta}\right) \\ +2\varepsilon\frac{K_1}{K}u_\theta\left(1+2\eta\varepsilon^{1/2}\right) + \varepsilon\frac{K_1}{K}\left(1+2\eta\varepsilon^{1/2}\right)\frac{\partial^2 u_\theta}{\partial\theta^2} + \frac{PE_\theta}{\gamma_1\omega} \end{array} \right\} \tag{5.89}$$

The fact that ε appears only as powers of $\varepsilon^{1/2}$ in above equation suggests an expansion for the boundary layer region of the form

$$u_\theta = u_0 + \varepsilon^{1/2}u_1 + \varepsilon u_2 + O(\varepsilon^{3/2}) \tag{5.90}$$

Terms of the order of ε^0: $\frac{\partial u_0}{\partial \zeta} = \frac{K_3}{K}\frac{\partial^2 u_0}{\partial \eta^2} + \frac{PE_\theta}{\gamma_1\omega}$ (5.91a)

Terms of the order of $\varepsilon^{1/2}$:

$$\frac{\partial u_1}{\partial \zeta} = \left\{\frac{K_3}{K}\frac{\partial^2 u_1}{\partial \eta^2} - \frac{K_3}{K}\frac{\partial u_0}{\partial \eta} - \frac{K_3}{K}\frac{\partial u_0}{\partial \eta}\right\} = \frac{K_3}{K}\left(\frac{\partial^2 u_1}{\partial \eta^2} - 2\frac{\partial u_0}{\partial \eta}\right) \tag{5.91b}$$

Terms of the order of ε :

$$\frac{\partial u_2}{\partial \zeta} = \left\{\frac{K_3}{K}\frac{\partial^2 u_2}{\partial \eta^2} - 2\eta\frac{K_3}{K}\frac{\partial u_0}{\partial \eta} - 2\frac{K_3}{K}\frac{\partial u_1}{\partial \eta} + \frac{K_1}{K}\frac{\partial}{\partial\theta}\left(\frac{u_0}{\tan\theta}\right) + 2\frac{K_1}{K}u_0 + \frac{K_1}{K}\frac{\partial^2 u_0}{\partial\theta^2}\right\} \tag{5.91c}$$

We seek a solution of Eqs. (5.91a, b, c) in the form of

$$u_0(\xi,\theta,\zeta) = u_{00}(\xi,\theta)e^{i\zeta} \tag{5.92a}$$

$$u_1(\xi,\theta,\zeta) = u_{10}(\xi,\theta)e^{i\zeta} \tag{5.92b}$$

$$u_2(\xi,\theta,\zeta) = u_{20}(\xi,\theta)e^{i\zeta} \tag{5.92c}$$

Using the strong anchoring boundary condition, $u_\theta(\eta=0)=0$, the solution of Eqs. (5.91) is

$$u_\theta(\eta) = \frac{P_0 E_{\theta 0}}{\gamma_1 \omega\left(i - \frac{K_3}{K}k^2\right)}\left(e^{-k\eta} - e^{-\alpha(1+i)\eta}\right)$$
$$+ \varepsilon^{1/2}\frac{K_3}{K}2k\frac{P_0 E_{\theta 0}}{\gamma_1 \omega\left(i - \frac{K_3}{K}k^2\right)^2}\left(e^{-k\eta} - e^{-\alpha(1+i)\eta}\right) \qquad (5.93)$$
$$- \varepsilon^{1/2}\frac{PE_{\theta 0}}{\gamma_1 \omega\left(i - \frac{K_3}{K}k^2\right)}\eta e^{-\alpha(1+i)\eta} + O(\varepsilon)$$

where $\alpha = \sqrt{\frac{K}{2K_3}}$. This is the *inner solution*, valid inside thin boundary layer.

5.7.3 Composite Analysis

The inner solution for $u_\theta(r)$ is $u_i(\xi)$ obtained by the singular perturbation analysis and the outer solution of $u_\theta(r)$ is $u_o(\eta)$ is obtained by the regular perturbation analysis. Now, these solutions must be matched. Unlike problems involving distinct regions separated by a definite surface, such as a phase boundary, this matching is not accomplished at a fixed location. Instead the matching must be done in an asymptotic sense expressed as

$$\lim_{\xi \to 1} u_i(\xi) = \lim_{\eta \to \infty} u_o(\eta) \qquad (5.94)$$

Eq. (5.94) is based on the observation that for $\varepsilon << 1$, large values of the boundary layer coordinate η correspond to values of the original variable ξ near unity. In general, an overall or composite solution can be constructed by adding the solutions for the two regions and subtracting the part of the answer that is common to both solutions:

$$u_\theta = u_i(\xi) + u_o(\eta) - \lim_{\xi \to 1} u_i(\xi) = u_i(\xi) + u_o(\eta) - \lim_{\eta \to \infty} u_o(\eta) \tag{5.95}$$

The last term in either form of Eq. (5.95) corrects for the "double counting" which would otherwise occur in matching region defined either by $\eta \to \infty$ or $\xi \to 1$. The composite solution for the present problem is

$$\begin{aligned} u_\theta(\eta) = & \frac{P_0 E_{\theta 0}}{\gamma_1 \omega \left(i - \frac{K_3}{K} k^2 \right)} \left(e^{-k\eta} - e^{-\alpha(1+i)\eta} \right) \\ & + \varepsilon^{1/2} \frac{K_3}{K} 2k \frac{P_0 E_{\theta 0}}{\gamma_1 \omega \left(i - \frac{K_3}{K} k^2 \right)^2} \left(e^{-k\eta} - e^{-\alpha(1+i)\eta} \right) \\ & - \varepsilon^{1/2} \frac{P_0 E_{\theta 0}}{\gamma_1 \omega \left(i - \frac{K_3}{K} k^2 \right)} \eta e^{-\alpha(1+i)\eta} + O(\varepsilon)) \end{aligned} \tag{5.96}$$

This completes the solution for the director perturbation up to $O(\varepsilon)$. The real part of the composite solution is given by, $\mathrm{Re}(u_\theta(\eta,t)) =$

$$\begin{aligned} & \frac{P_0 E_{\theta 0}}{\gamma_1 \omega} \frac{1}{1+\chi^2} \begin{pmatrix} e^{-k\eta}(\sin\omega t - \chi\cos\omega t) \\ + e^{-\alpha\eta}(\chi\cos(\omega t - \alpha\eta) - \sin(\omega t - \alpha\eta)) \end{pmatrix} \\ & + \frac{P_0 E_{\theta 0}}{\gamma_1 \omega} \frac{1}{1+\chi^2} \left(e^{-\alpha\eta}(1-\xi)(\chi\cos(\omega t - \alpha\eta) - \sin(\omega t - \alpha\eta)) \right) \\ & + \frac{K_3}{K} \frac{P_0 E_{\theta 0}}{\gamma_1 \omega} \frac{2k\varepsilon^{1/2}}{(\chi^2+1)^2} \begin{pmatrix} e^{-k\eta}((\chi^2-1)\cos\omega t - 2\chi\sin\omega t) \\ + e^{-\alpha\eta} \begin{pmatrix} 2\chi\sin(\omega t - \alpha\eta) \\ -(\chi^2-1)\cos(\omega t - \alpha\eta) \end{pmatrix} \end{pmatrix} \\ & + O(\varepsilon) \end{aligned} \tag{5.97}$$

where $\chi = k^2 K_3 / K$. The first term in this solution is same as that for a **planar interface** and the second term is a first approximation for the effects of **surface curvature**. The third term is entirely due to **polarization decay**. Fig. 5.7 shows the

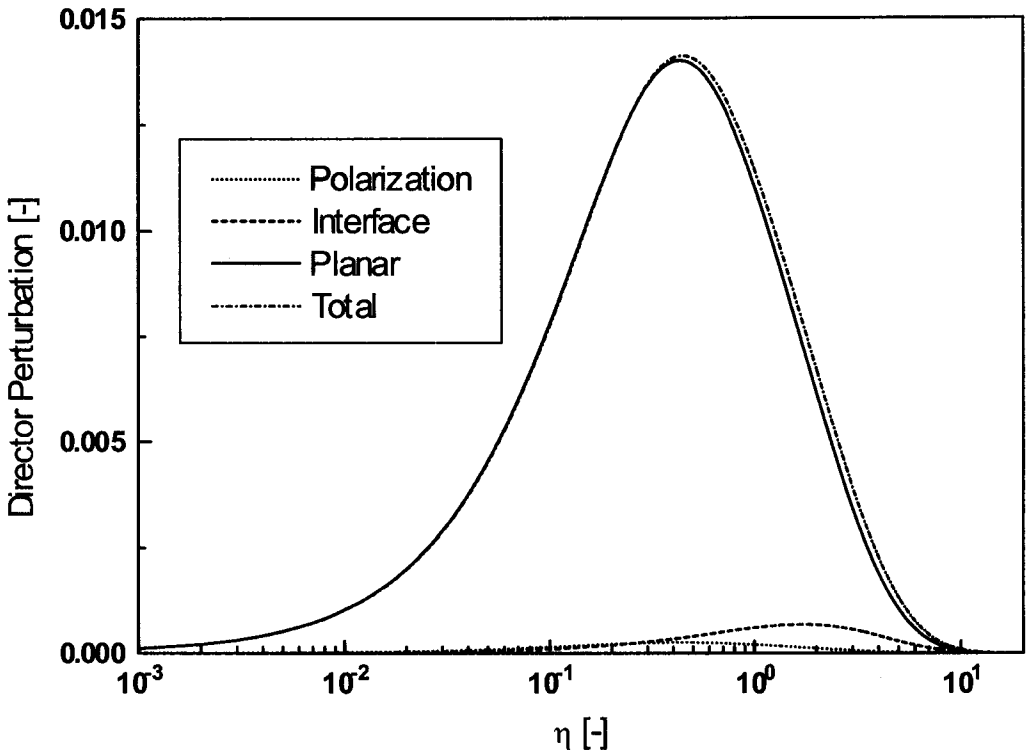

Fig. 5.7: The root mean square values of Planar, Interfacial, and Polarization contribution to Total director perturbation for a radial nematic droplet when $\boldsymbol{E} = (0,3700,0)V/m$.

relative importance of these three terms on director perturbation. The planar interface contribution to director fluctuation always dominates over the other two effects.

Various Stresses:

The kinematic measures are

$$N_r^0 = \frac{\partial u_r}{\partial t} = 0 = \frac{\partial u_\phi}{\partial t} = N_\phi^0$$
$$N_\theta^0 = \frac{\partial u_\theta}{\partial t} \tag{5.98}$$

Therefore, the components of stress tensor can be expressed as

$$\sigma_{\theta r} = \alpha_3 \frac{\partial u_\theta}{\partial t} - K_1 \frac{2}{r} \frac{\partial u_\theta}{\partial r}$$
$$\sigma_{r\theta} = \alpha_2 \frac{\partial u_\theta}{\partial t} - K_3 \left(\frac{1}{r} \frac{\partial u_\theta}{\partial r} + \frac{u_\theta}{r^2} \right) \tag{5.99}$$
$$\sigma_{\theta\theta} = -K_1 \frac{2}{r^2} - K_1 \frac{\partial u_\theta}{r \partial \theta} \frac{1}{r}$$
$$\sigma_{rr} = \sigma_{\phi r} = \sigma_{\phi\theta} = \sigma_{r\phi} = \sigma_{\theta\phi} = \sigma_{\phi\phi} = 0$$

The above director perturbation has been obtained without taking into account the flow field in the liquid crystalline phase. The effect of the velocity gradient may still be insignificant on the director perturbation, but the velocity itself in the liquid crystalline phase is highly dependent on the director perturbation. This will affect the stresses at the boundary. Therefore, one cannot proceed as in section 5.6.6 to find the velocity field in the isotropic phase and the associated velocity of the nematic-isotropic interface in a self-consistent manner. One particular difficulty with the spherical droplet is visualizing the local velocity of the interface in a manner such that droplet as a whole is not moving.

5.8 Summary

We have presented a complete analytical treatment of the constitutive equations of nematodynamics, according to the hydrodynamical approach of Leslie-Ericksen, for a semi-infinite nematic sample subjected to a far-field oscillating electric field. The velocity and director fields are taken into account exactly. In the linearized limit, the local electric field is independent of the small director perturbation. The local electric field is the dominant factor for director perturbation. The velocity field is induced by the perturbation of the director by the electric field. The deformation of the interface appears to be too small to effect the dielectric measurements. For slightly curved interfaces we can analytically obtain the director perturbation and the effect of curvature on it, but we cannot solve the velocity fields on the either side of the interface in a self-consistent manner. The planar contribution dominates, however, so local interfacial strains as computed within this approximation must still be small.

Chapter 6

CONCLUSION and FUTURE WORK

Linear viscoelastic measurements on low viscosity fluids with the TA Instruments controlled stress AR 1000 rheometer produce spurious results (negative storage modulus and oscillations in the magnitude of complex viscosity). The most likely explanation is that the high frequency oscillatory data is corrupted by the uncertainty in the measurement of the moment of inertia of the rotor.

The unusual temperature dependence of the interfacial tension between a thermotropic low-molar mass nematic liquid crystal and an amorphous liquid, in which the interfacial tension is an increasing function of temperature, is probably a consequence of homeotropic orientation at the interface and the loss of nematic order with increasing temperature. That the increase of interfacial tension with temperature extends well above the bulk N-I transition is apparently because of the residual nematic order at the interface that is observed by optical microscopy. The interfacial tension in the smectic-A phase appears to be even less than that in the nematic, but direct measurements cannot be made.

The fact that the dielectric response of the 5CB and 8CB dispersions depends strongly on the structural state of the droplets and the viscosity of the suspending PDMS is suggestive of a coupling with the mechanics of the interface that affects the spectrum of the dispersed phase and shifts the Maxwell-Wagner peak. This result is unexpected, but it is the most consistent explanation of the observation of a single relaxation in the 100 – 1,000 Hz range that is displaced from the expected Maxwell-Wagner relaxation. The mechanics of the interaction between an oscillating electric field and a droplet of a

material that can undergo a liquid crystalline transition and contains a permanent dipole is an unsolved problem, so our explanation must remain speculative.

6.1 FUTURE WORK

The future direction for this work should comprise two complementary approaches for understanding nematic-isotropic interfacial mechanics: continuum theory (electrodynamics of nematic droplet, and motion of a nematic droplet in a Newtonian fluid) and experiments (rheological and dielectric).

6.1.1 Electrodynamics of Nematic Droplet

To establish the correspondence between dielectric measurements and linear viscoelastic measurements, it is necessary to determine the response of a spherical nematic droplet in the presence of an ac electric field while allowing for the droplet interface to deform infinitesimally. Initially, a linearized Leslie-Ericksen (*LE*) material (Larson, 1999) with equal Frank elastic constants should be used to analyze the first-order effect of orientation fluctuations on the droplet deformation. The interaction of molecular dipoles with the applied electric field should be included in this formalism. The analytical solution of the complete problem is not viable, and we have seen that perturbation solutions that neglect the full droplet geometry are inadequate to explain the experimental observations, but a numerical solution should be possible. This analysis will describe the deformation of the droplet interface in terms of strain and displacement.

6.1.2 Motion of a Nematic Droplet in a Newtonian Fluid

The aim here is to determine the equivalent of the Hadamard-Rybczynski equation (Leal, 1992) for nematic drops. The analysis of droplet motion to obtain the density difference for interfacial measurement in Appendix B was based on a Newtonian

fluid equation, which is clearly adequate. To determine the drag force on a uniformly moving nematic drop in an infinite expanse of a quiescent Newtonian fluid one needs to solve the steady mass balance, linear momentum balance, and angular momentum balance equations simultaneously. The shear viscosity of low molar mass liquid crystals in the nematic phase may be independent of shear rate, but the effective viscosity in the circulating flow inside the nematic droplet might be different from the viscosity measured in a shear viscometer. Finally, one can address the effect of five independent Leslie viscosity coefficients and three independent Frank elastic constants of the liquid crystal on the circulating flow inside the drop and the resulting drag force experienced by the drop.

6.1.3 Experiments

To determine the true relation between dielectric measurements and linear viscoelastic measurements, one needs to be able to choose an immiscible liquid crystal – suspending fluid system where both measurements can be performed reliably. The expected frequency range in which interfacial effects are important in linear viscoelastic measurements depends strongly on the matrix viscosity. By raising the viscosity of the continuous matrix, it is possible to bring the interfacial relaxation down to the frequency range accessible to a rheometer (typically less than 100 rad/s). However, in such cases the continuous matrix may be so elastic that the response of the interface may not be detected. The other important consideration is the density mismatch between the liquid crystal and matrix fluid, which can cause significant droplet coalescence during the course of measurements. Identification of an appropriate system is thus a major challenge.

Appendix A

DYNAMIC MEASUREMENTS IN A CONE-and-PLATE RHEOMETER

To quote Walters (1963), "To my knowledge no satisfactory theory for oscillatory flows in the cone-and-plate viscometer has been published; which is not surprising, since there is no solution to the equations of motion (even for a purely viscous Newtonian liquid), which represent a regular transmission of a sinusoidal disturbance from the cone to the plate, or vice versa." All published solutions available so far for oscillatory flow in cone-and-plate geometry assume zero inertia of the sample. This is, of course, a critical assumption, especially when the viscosity/elasticity of the material is quite low. Here we solve the equation of motion, including inertial terms, for oscillatory flow in the cone-and-plate geometry and develop the theory for cone-and-plate rheometry in small amplitude oscillatory flow.

A.1 Equation of Motion: Spherical polar co-ordinates (r,θ,ϕ) are chosen with the cone and plate located at $\theta=\pi/2-\beta$ and $\theta=\pi/2$, respectively, as shown in Fig. A1. A couple is applied to the cone, forcing it to make small amplitude oscillations of amplitude χ_1 at angular velocity ω.

It is assumed that the physical components of the velocity vector $(v_{(r)}, v_{(\theta)}, v_{(\phi)})$ can be written in the form:

$$v_{(r)} = \mathrm{Re}\{u(r,\theta)e^{i\omega t}\} \tag{A1a}$$

$$v_{(\theta)} = \mathrm{Re}\{v(r,\theta)e^{i\omega t}\} \tag{A1b}$$

$$v_{(\phi)} = \mathrm{Re}\{w(r,\theta)e^{i\omega t}\} \tag{A1c}$$

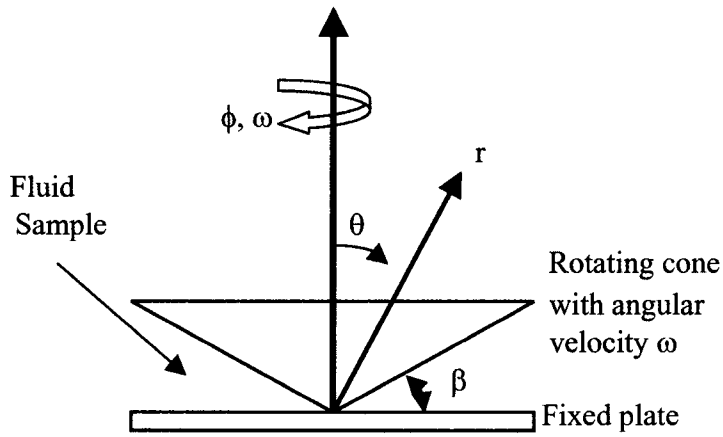

Fig A1: Cone-and-plate device; β is very small.

where u, v, and w are complex. This reduces the equation of motion in the ϕ direction to:

$$\frac{1}{r^2}\frac{\partial}{\partial r}\left(r^2\frac{\partial w}{\partial r}\right)+\frac{1}{r^2\sin\theta}\frac{\partial}{\partial\theta}\left(\sin\theta\frac{\partial w}{\partial\theta}\right)-\frac{w}{r^2\sin^2\theta}=-\alpha^2 w \tag{A2}$$

where $\alpha^2=-\dfrac{i\omega\rho}{\eta^*}$,

ρ is the density of the fluid, and η^* is the complex viscosity. The boundary conditions are

$$w(r,\pi/2-\beta)=i\omega\chi_1(r\cos\beta) \tag{A3a}$$

$$w(r,\pi/2)=0 \tag{A3b}$$

A separable solution of Eq. (A2) in the form $w=\omega\, r\sin\theta\ \chi(\theta)$ does not exist. A solution of (A2) subject to boundary conditions (A3) that is valid for small αr can be written in the form (Maude and Walters, 1964)

$$\begin{aligned} w=&\left[r-\frac{\alpha^2r^3}{10}+\frac{\alpha^4r^5}{280}-\frac{\alpha^6r^7}{15120}+\cdots\right]R_1'(\theta)\\ &+\left[\frac{\alpha^2r^3}{10}-\frac{\alpha^4r^5}{180}+\frac{\alpha^6r^7}{7920}-\cdots\right]R_3'(\theta)\\ &+\left[\frac{\alpha^4r^5}{504}-\frac{\alpha^6r^7}{13104}+\cdots\right]R_5'(\theta)\\ &+\left[\frac{7\alpha^6r^7}{432432}-\cdots\right]R_7'(\theta) \end{aligned} \tag{A4}$$

where terms of the order of α^8r^9 have been neglected. In this equation

$$R_m'(\theta)=A_mP_m'(\cos\theta)+B_mQ_m'(\cos\theta) \tag{A5}$$

where P_m and Q_m are Legendre functions of the first and second kind, respectively, and the prime denotes differentiation with respect to θ. A_m and B_m are constants given by

$$A_m = \frac{-i\omega\ \chi_1 \cos\beta\ Q_m'(\pi/2)}{Q_m'(\pi/2-\beta)\ P_m'(\pi/2) - P_m'(\pi/2-\beta)\ Q_m'(\pi/2)}$$
$$B_m = \frac{i\omega\ \chi_1 \cos\beta\ P_m'(\pi/2)}{Q_m'(\pi/2-\beta)\ P_m'(\pi/2) - P_m'(\pi/2-\beta)\ Q_m'(\pi/2)} \qquad \text{(A6a, b)}$$

where $P_m'(\pi/2)$ is the value of $dP_m(\cos\theta)/d\theta$ at $\theta = \pi/2$, etc.

The relevant shear stress $\tau_{\theta\phi}$ at the cone is given by

$$\tau_{\theta\phi} = \frac{\eta^*}{r}\left\{\frac{\partial w}{\partial \theta} - w\ \cot\theta\right\} e^{i\omega t} \qquad \text{(A7)}$$

The equation of motion of the cone is

$$C + C_F = I\ddot{\phi} \qquad \text{(A8)}$$

where C is the couple imposed on the cone, C_F is the couple on the cone due to the fluid, and $\ddot{\phi}$ is the angular acceleration of the cone.

For a cone of radius R

$$C_F = \int_0^R \tau_{\theta\phi}\Big|_{\theta=(\pi/2-\beta)} 2\pi\ r^2 \sin^2(\pi/2-\beta) dr \qquad \text{(A9)}$$

The couple imposed on the cone is given by

$$C = M_0 e^{i\omega t} e^{ip} \qquad \text{(A10)}$$

where p is the phase lag of the output displacement waveform behind the input couple.

For Eq. (A4) to be useful in rheometry, Eq. (A8) along with Eqs. (A9) and (A10) should yield a simple expression for η' and G'. The complex viscosity η^*, however, is embodied in α^2. Hence, we use simplifications in Eq. (A2).

A.2 SIMPLIFICATIONS

1. No Fluid Inertia: ρ = 0 and $\beta << 1$; In this case solution of Eq. (A2) subject to boundary condition (A3) is straightforward and Eq. (A8) yields:

$$\eta' = \frac{3M_0 \sin p}{2R^3 \pi \omega \chi_1} \beta \tag{A11a}$$

$$G' = \frac{3\left(\frac{M_0 \cos p}{\chi_1} + I\omega^2\right)}{2\pi R^3} \beta \tag{A11b}$$

This was the result shown in Eq. (2.8).

2. Finite Fluid Inertia: $\beta << 1$, ρ = finite, but $i\omega\rho R^2\beta^2/\eta^*$ = ε <<1; In this case we can use a regular perturbation expansion as follows:

$$\overline{w} = \overline{w}_0 + \varepsilon\overline{w}_1 + \varepsilon^2\overline{w}_2 + O(\varepsilon^3) \tag{A12}$$

Substituting Eq. (A12) in Eq. (A2) and collecting different powers of ε, we obtain $[\bar{r} = r/R, \overline{w} = w/(i\omega\chi_1 R)]$

$$\varepsilon^0: \qquad \frac{1}{\bar{r}^2}\left[\frac{\partial}{\partial \bar{r}}\left(\bar{r}^2 \frac{\partial \overline{w}_0}{\partial \bar{r}}\right) + \frac{\partial^2 \overline{w}_0}{\partial \theta^2} - \overline{w}_0\right] = 0 \tag{A13}$$

$$\text{with } \overline{w}_0(\bar{r}, \pi/2) = 0 \text{ and } \overline{w}_0(\bar{r}, \pi/2 - \beta) = \bar{r}\cos\beta$$

$$\varepsilon^1: \qquad \frac{1}{\bar{r}^2}\left[\frac{\partial}{\partial \bar{r}}\left(\bar{r}^2 \frac{\partial \overline{w}_1}{\partial \bar{r}}\right) + \frac{\partial^2 \overline{w}_1}{\partial \theta^2} - \overline{w}_1\right] = \overline{w}_0 \tag{A14}$$

$$\text{with } \overline{w}_1(\bar{r}, \pi/2) = 0 \text{ and } \overline{w}_1(\bar{r}, \pi/2 - \beta) = 0$$

$$\varepsilon^2: \qquad \frac{1}{\bar{r}^2}\left[\frac{\partial}{\partial \bar{r}}\left(\bar{r}^2\frac{\partial \overline{w}_2}{\partial \bar{r}}\right)+\frac{\partial^2 \overline{w}_2}{\partial \theta^2}-\overline{w}_2\right]=\overline{w}_1 \tag{A15}$$

$$\text{with } \overline{w}_2(\bar{r},\pi/2)=0 \text{ and } \overline{w}_2(\bar{r},\pi/2-\beta)=0$$

The solution of Eq. (A13) is

$$\overline{w}_0=\bar{r}\cot\beta\cos\theta$$

The solution of Eq. (A14) is

$$\overline{w}_1=\bar{r}^3\left(\frac{2.65\times10^{-2}}{\beta}\cos(\sqrt{11}\theta)+\frac{1.44\times10^{-2}}{\beta}\sin(\sqrt{11}\theta)+\frac{\cot\beta\cos\theta}{10}\right)$$

The solution of Eq. (A15) is

$$\overline{w}_2=\bar{r}^5\left(\begin{array}{l}\dfrac{3.03\times10^{-4}}{\beta}\cos(\sqrt{29}\theta)+\dfrac{2.095\times10^{-4}}{\beta}\sin(\sqrt{29}\theta)\\ \dfrac{1.47\times10^{-3}}{\beta}\cos(\sqrt{11}\theta)+\dfrac{7.99\times10^{-4}}{\beta}\sin(\sqrt{11}\theta)+\dfrac{\cot\beta\cos\theta}{280}\end{array}\right)$$

In determining the coefficients of the cosine and sine terms in $\overline{w}_1$ and $\overline{w}_2$, we have linearized the non-linear terms in β (sine and cosine terms). This expression is valid for any arbitrarily small β << 1. Hence, we have

$$w=i\omega\chi_1 R\left[\overline{w}_0+\varepsilon\overline{w}_1+\varepsilon^2\overline{w}_2+O(\varepsilon^3)\right] \tag{A16}$$

Eq. (A9) gives,

$$\frac{C_F}{e^{i\omega t}}=59.94\mathrm{R}^3\eta^* i\omega\chi_1-0.01461\rho\omega^2R^5\chi_1+i8.508\times10^{-7}\frac{\rho^2\omega^3R^7\chi_1}{\eta^*} \tag{A17}$$

Here we have used the fact that $\beta=2^o=\pi/90\ rad$, in order to simplify the expression.

Equating Eq. (A17) to $M_0 e^{ip} + I\omega^2 \chi_1$, we obtain η' and G'. The base solution ($\rho = 0$) is:

$$\eta' = \frac{M_0 \sin p}{59.94 w \chi_1 R^3}, \tag{A18a}$$

$$G' = \frac{\frac{M_0 \cos p}{\chi_1} + I\omega^2}{59.94 R^3} \tag{A18b}$$

This is identical to the Eqs. (2.8) and (A11) mentioned earlier for the same case. The first order inertial correction to this solution yields:

$$\eta' = \frac{M_0 \sin p}{59.94 w \chi_1 R^3}, \tag{A19a}$$

$$G' = \frac{\frac{M_0 \cos p}{\chi_1} + I\omega^2}{59.94 R^3} + 2.437 \times 10^{-4} \rho \omega^2 R^2 \tag{A19b}$$

Compared to the base solution, η' is unaltered, but G' increases due to fluid inertia. The correction proportional to $\rho\omega^2 R^2$ is of the expected form. Including the second order correction terms in η' and G' is now straightforward, as we have already calculated the couple on the cone due to the fluid up to the second order term, but it is complicated algebraically. This issue is addressed in chapter 2.

We learned recently that Eq. (A19) has also been derived by Golden *et al.* (1990) in a Ph.D. thesis at the University of Plymouth, Plymouth, UK, although the result is unpublished. Golden *et al.* (1990) find

$$\eta' = \frac{M_0 \sin p}{\left(\frac{2\pi}{3\beta}\right) w \chi_1 R^3}, \tag{A20a}$$

$$G' = \frac{\dfrac{M_0 \cos p}{\chi_1} + I\omega^2}{\left(\dfrac{2\pi}{3\beta}\right)R^3} + \frac{\beta^2}{5}\rho\omega^2 R^2 \qquad \text{(A20b)}$$

which is equivalent to our result for $\beta = 2^o = \pi/90 \ \ rad$. However, there is a difference in the methodologies employed by Golden *et al.* (1990) and us in arriving at the same result. Golden *et al.* (1990) derived their result by perturbing the full solution of equation of motion given by Nally (1965), whereas we have derived our result by perturbing the equation of motion itself.

The corresponding results for a parallel plate geometry are straightforward to derive and are summarized up to the first order correction as follows:

$$\eta' = \frac{M_0 \sin p}{\chi_1}\frac{2h}{\pi\omega R^4} \qquad \text{(A21a)}$$

$$G' = \left(\frac{M_0 \cos p}{\chi_1} + I\omega^2\right)\frac{2h}{\pi R^4} + \frac{\rho\omega^2 h^2}{3} \qquad \text{(A21b)}$$

The second order correction in η' and G' is complicated algebraically here also.

Inertia affects the complex dynamic viscosity in the same way in both cone-and-plate flow and parallel plate flow. First order correction does not affect η', but does affect G'. The first order inertial correction increases G' for both flows. The second order inertial correction affects both η' and G'.

Appendix B

MEASUREMENT OF DENSITY DIFFERENCE

The density difference between 5CB and PDMS was determined by measuring the velocity of a spherical droplet of 5CB in a large expanse of quiescent PDMS. The PDMS was filled into a curvette and equilibrated in the environmental chamber used for the pendant droplet experiments. 5CB was equilibrated at the same temperature for at least one hour in a 10 μl syringe. A 5 μl droplet of 5CB (approximately 2 mm in diameter) was then formed at the tip of the needle by depressing the plunger, and the time required to travel between two marked points away from both ends was recorded. The velocities of three different droplets were measured at each temperature. Video images of the droplets confirmed that they were indeed spherical. The drag force was determined from the Hadamard-Rybczynski equation (Leal, 1992) for the motion of a droplet of a Newtonian liquid in an infinite expanse of a quiescent Newtonian fluid and equated to the buoyant force, which is the product of $\Delta\rho$, the droplet volume, and the gravitational acceleration; the density difference then follows from the equation

$$\Delta\rho = \frac{3U\eta_2}{2ga^2}\frac{3\lambda+2}{\lambda+1} \tag{B1}$$

U is the droplet velocity, a is the radius, η_2 is the viscosity of the continuous phase, λ is the ratio of the droplet viscosity to the viscosity of the suspending fluid, and g is the gravitational acceleration.

The volume of the spherical droplet is known to within 0.1 μl, hence the uncertainty in the estimation of the radius is less than 1%. This translates to an

uncertainty of less than 2% in $\Delta\rho$, since $\Delta\rho$ is proportional to the inverse square of the diameter. The uncertainly in recording the time is of order 0.2 s out of a total time of order 10 s, which introduces an additional 2% uncertainly in $\Delta\rho$. The use of the Hadamard-Rybczynski equation introduces an additional uncertainty, since the equation is valid only for a droplet of a Newtonian fluid; the shear viscosity of 5CB in the nematic phase is independent of shear rate, but the effective viscosity in the circulating flow inside the nematic droplet might be different from the viscosity measured in a shear viscometer. We expect this effect to be small, however, and we anticipate an uncertainty of no more than 5% in the density difference.

The density difference data for the 5CB/PDMS pair are shown in Fig. B1. Density difference calculations based on the data of Gannon and Faber (1978) and Tintaru *et al.* (2001) are also shown for comparison. Our data lie between the two sets. Our data are within 5% of Gannon and Faber (1978) below T_{NI}, while we observe a sharper rise in $\Delta\rho$ above T_{NI}. The translating 8CB droplet does not remain spherical, so we were unable to measure the density difference of the 8CB/PDMS pair directly. Hence, we used the density of 8CB as reported by Tintaru *et al.* (2001) to compute the density difference. In view of the fact that the density difference for 5CB determined from the data of Tintaru *et al.* (2001) is high relative to our direct measurement, we must anticipate that the magnitude of the interfacial tension for the 8CB/PDMS interface may be somewhat lower than shown in Fig. 3.5.

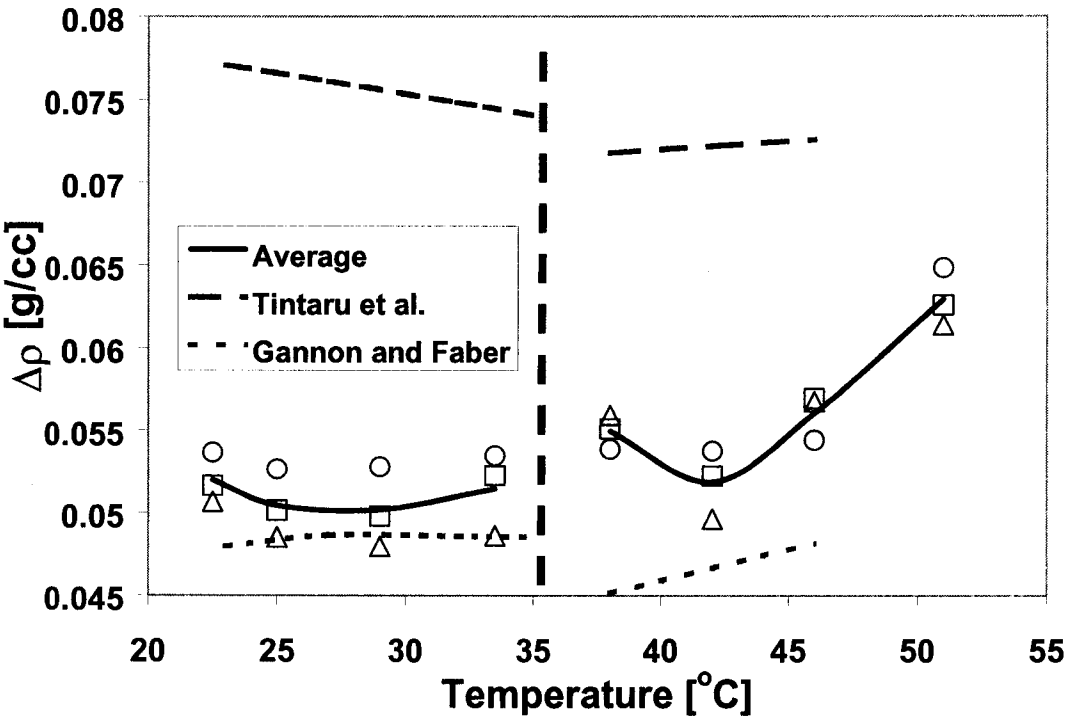

Fig B1: Density difference of the 5CB/PDMS system. The solid line passes through is the average of three data points. The upper dashed line is computed from the manufacturer's data for the density of PDMS and the data of Tintaru *et al.* (2001) for the density of 5CB, while the lower dotted line is computed from the data of Gannon and Faber (1978) for the density of 5CB. The dashed vertical line shows the bulk N-I transition temperature.

Appendix C

ISSUES IN LC BLEND DIELECTRIC SPECTROSCOPY

C.1 Effect of Water Solubility in Silicone Oil

Solubility of water in PDMS is in the parts per billion range, but even trace amounts of water present in PDMS can interact with -C≡N group of the liquid crystal. Water molecules can potentially form hydrogen bonds with the -C≡N terminal group of the liquid crystal molecule. The water molecule has a permanent dipole moment, which can interact with the applied electric field in a manner independent of the liquid crystal.

To determine the possible effect of trace amounts of water in the PDMS that might have migrated to the interface, we performed a set of controlled experiments. After preparing the 6.2% 5CB dispersion in usual manner, the sample was divided into three parts. The first sample was kept in a desiccater for 144 hours under vacuum. The second sample was left open in the air in a vial for 144 hours, while the third sample was kept in a tightly capped vial, as has been done for all other experiments. Transfer of the desiccated sample to the dielectric sample cell was done quickly in a nitrogen gas environment.

Figure C1 shows the complex dielectric permittivity of a 6.2% 5CB dispersion in silicone oil in three controlled experiments at 33 ^{o}C. There is no effect of changing the environment, as the dielectric spectrum remains essentially unchanged in all three controlled experiments.

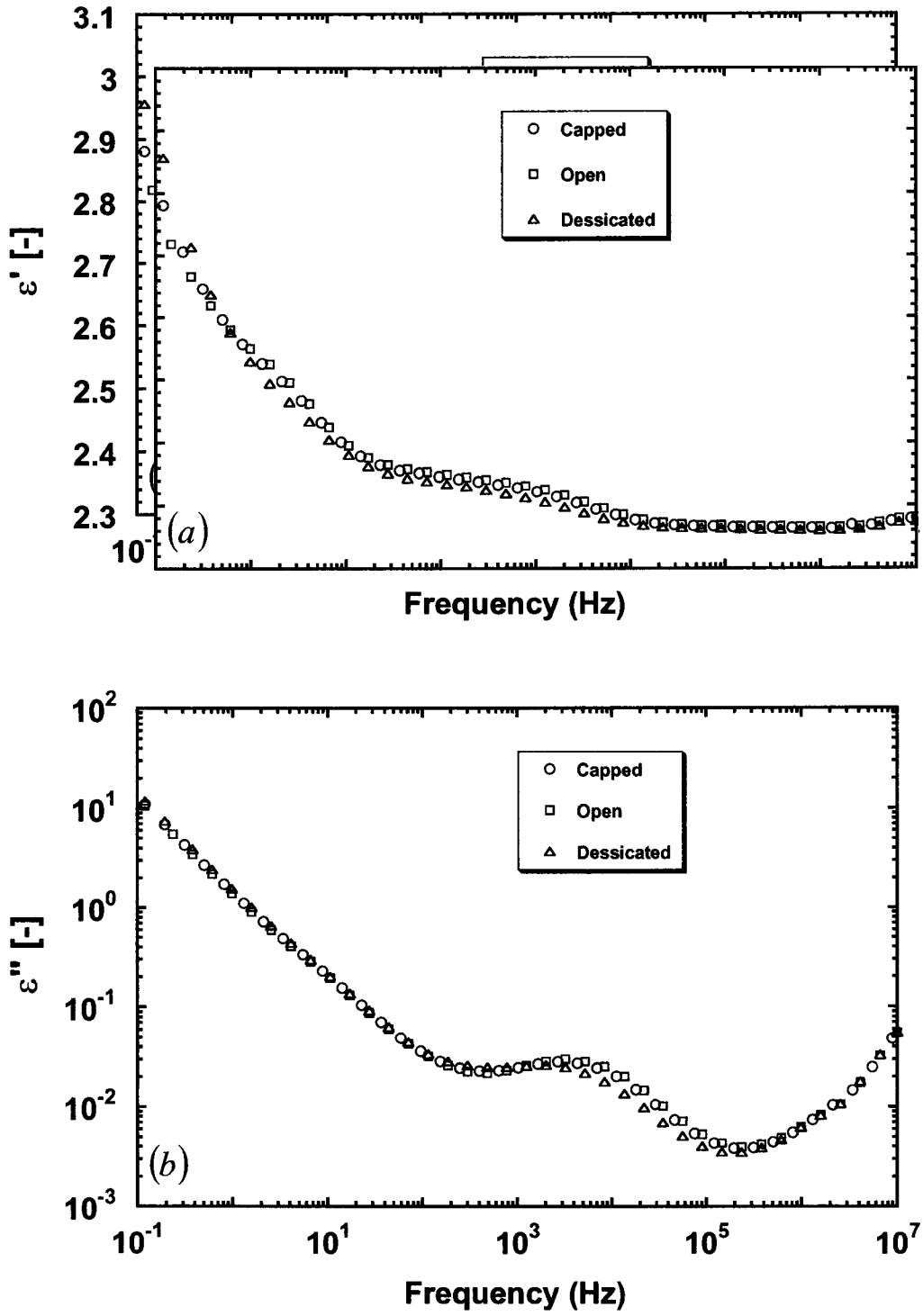

Fig C1: Frequency dependent (a) capacitive spectrum $\varepsilon'(\omega)$ and (b) loss spectrum $\varepsilon''(\omega)$ of 6.2% dispersion of 5CB in PDMS 200 at 33 °C in three controlled environments.

C.2 Effect of Surface Conductivity

The presence of some surface-active materials at the droplet interface can cause surface conductivity in the tangential direction. Water might be attracted by the –C≡N end group of the liquid crystal, for example, and cause some conduction in the tangential direction at the interface. In the same fashion, some surface coatings might potentially alter the response of the droplet interface. Consider the lossy dielectric sphere with a surface layer of thickness $\Delta << R$, where R is the radius of sphere, as shown in Fig. C2. Let us denote the familiar ohmic surface conductivity (in Siemens) of the thin resistive surface layer by λ. Then, from Jones (1995), the effective complex dielectric permittivity of the dispersed phase is $\varepsilon_D^* - i\frac{2\lambda/R}{\varepsilon_0\omega} = \varepsilon'_D - i\left(\varepsilon''_D + \frac{2\lambda/R}{\varepsilon_0\omega}\right)$. For the low frequency limit, the equivalent complex dielectric permittivity of the dispersed phase reduces to $\varepsilon'_D - i\left(\frac{\sigma_D + 2\lambda/R}{\varepsilon_0\omega}\right)$. Surface conductance increases the effective dc conductivity of the droplet by the radius-dependent factor $2\lambda/R$. This term has same effect as changing the bulk conductivity of 5CB. However, changing the bulk conductivity of either phase does little or nothing to alter the relaxation behavior of the blend. Figure C3 compares the experimental data with the calculations based on Maxwell-Wagner model (section 4.4) with a surface conductivity contribution $2\lambda/R$ that is 20% of σ_D, the actual conductivity of 5CB ($\sigma_D/\varepsilon_0 = 2200/\mathrm{s}$). The corresponding surface conductivity is 2 x 10^{-14} Siemens.

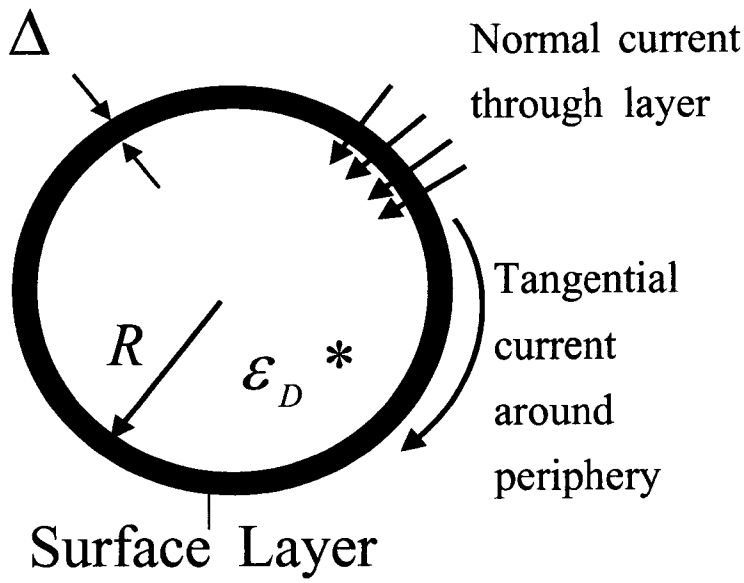

Fig C2: Dielectric sphere with very thin outer layer of thickness Δ, showing the pathways for electric current.

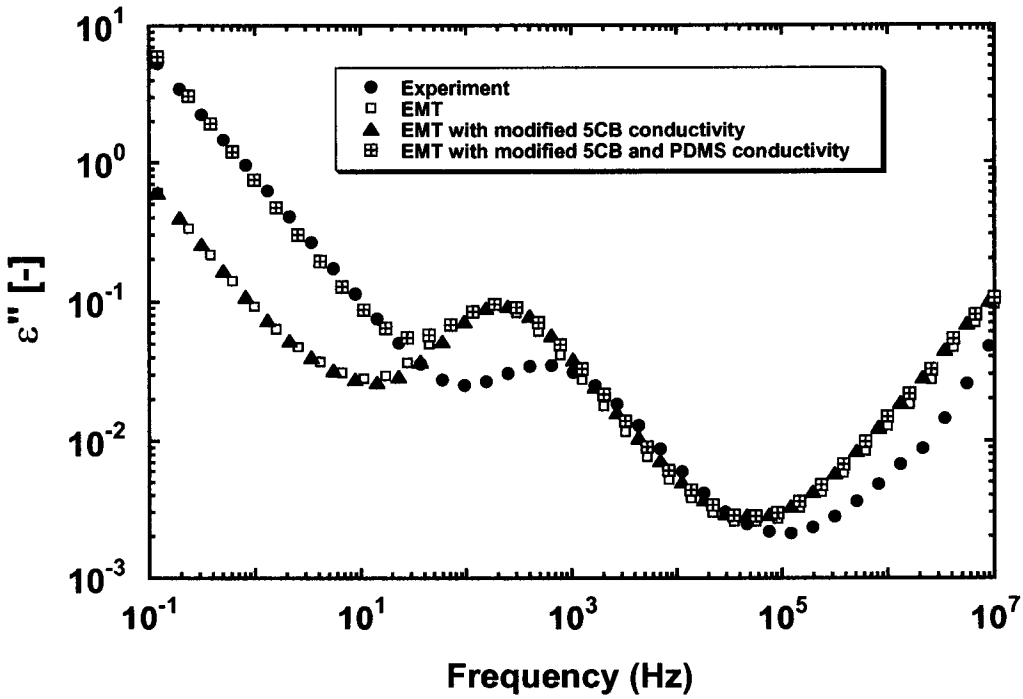

Fig C3: Dielectric loss factor of 6.2% 5CB blend in PDMS at 32 °C. The PDMS conductivity has been adjusted to match the experimental low frequency data.

C.3 Spherical Shell in Uniform Field with Ohmic Loss

Another possibility for the discrepancy between the data and EMT calculations could be the existence of an outer droplet layer with dielectric properties different from the inner core. Consider a lossy dielectric spherical droplet covered with a single layer of uniform thickness. Figure C4 shows a layered lossy dielectric sphere subjected to a uniform electric field. The concentric outer shell and inner core have complex permittivities ε_S^* and ε_D^*, respectively, while the outer radius is R_o and the core radius is R_i. It is assumed that there is no free (unpaired) electric charge anywhere. Then, the effective homogeneous complex dielectric permittivity of the core-shell system is (Jones, 1995):

$$\varepsilon_{eff}^* = \varepsilon_s^* \left\{ \frac{a^3 + 2\left(\frac{\varepsilon_D^* - \varepsilon_s^*}{\varepsilon_D^* + 2\varepsilon_s^*} \right)}{a^3 - \left(\frac{\varepsilon_D^* - \varepsilon_s^*}{\varepsilon_D^* + 2\varepsilon_s^*} \right)} \right\} \tag{C1}$$

where $a = R_o / R_i$. This equation can also be written as:

$$2\left(a^3 - 1\right)\left(\varepsilon_s^*\right)^2 + \left(\begin{matrix} \varepsilon_D^* a^3 + 2\varepsilon_D^* \\ -\varepsilon_{eff}^* - 2a^3 \varepsilon_{eff}^* \end{matrix} \right)\varepsilon_s^* + \left(\begin{matrix} \varepsilon_D^* \varepsilon_{eff}^* \\ -\varepsilon_D^* a^3 \varepsilon_{eff}^* \end{matrix} \right) = 0 \tag{C2}$$

We seek to determine the dielectric properties of the shell region (the dielectric properties of the core region are that of bulk 5CB) that would bring the EMT spectrum and experimental spectrum together. Therefore, we need to solve Eq. (C1) for ε_S^*. The only adjustable parameter is the ratio of two radii, a. Equation (C2) is quadratic in

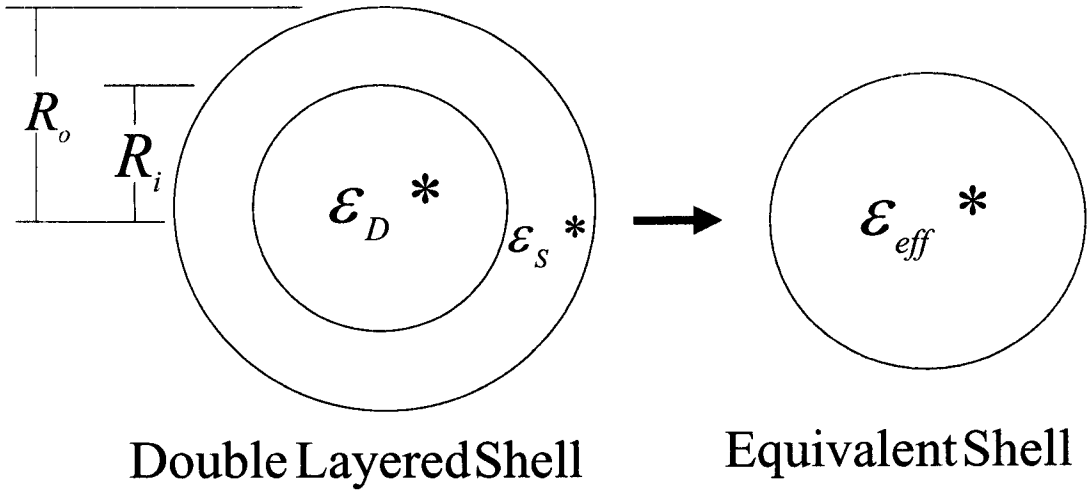

Fig C4: Layered spherical shell and equivalent homogeneous sphere with apparent dielectric permittivity ε_{eff} * defined by Eq. C1.

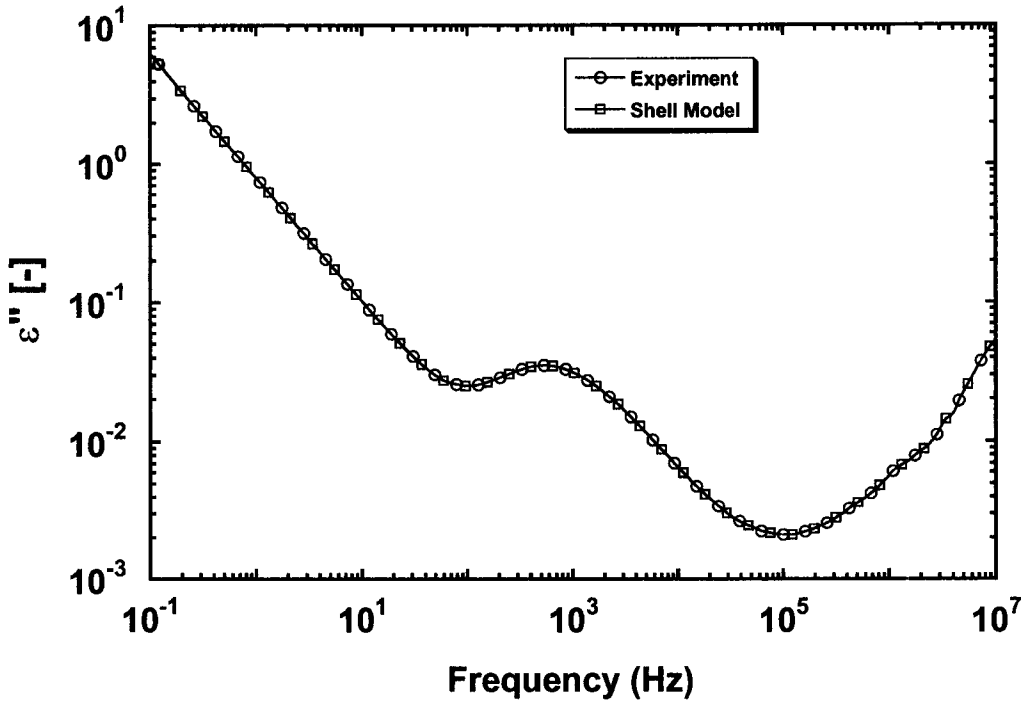

Fig C5: Dielectric loss factor of 6.2% 5CB blend obtained experimentally and using a spherical shell model. Dielectric properties of shell are given in Figs. C6 and C7.

ε_S *: for each ε_{eff} *, ε_D * and a, there exist two complex numbers, ε_S *, that satisfy Eq. (C1).

Figures C6 and C7 show the two sets of the required thin layer dielectric spectra data for the 6.2% 5CB blend at 32 °C that generate the Fig. C5 with absolute deviation from experimental data at any frequency less than 10^{-14}. The value of $a = R_o/R_i$ used is 1.1. In these figures, we compare ε_S * with experimental dielectric properties of 5CB, ε_D *, which is assumed to occupy the core of the layered spherical droplet. Not only does ε_S * deviate strongly from ε_D *, but also the general trend of ε_S * is unrealistic. A peak in ε'_S and a negative peak in ε''_S are not possible. Moreover, this model requires negative values of ε'_S and ε''_S. We have varied the diameter ratio a from 1.01 to 15 and it does not affect the qualitative behavior shown in Figs. C6 and C7. Modifying the conductivity of silicon oil also does not affect the general behavior as shown in Figs. C6 and C7. Hence a core-shell model for the LC-PDMS system is unlikely to explain the dielectric data.

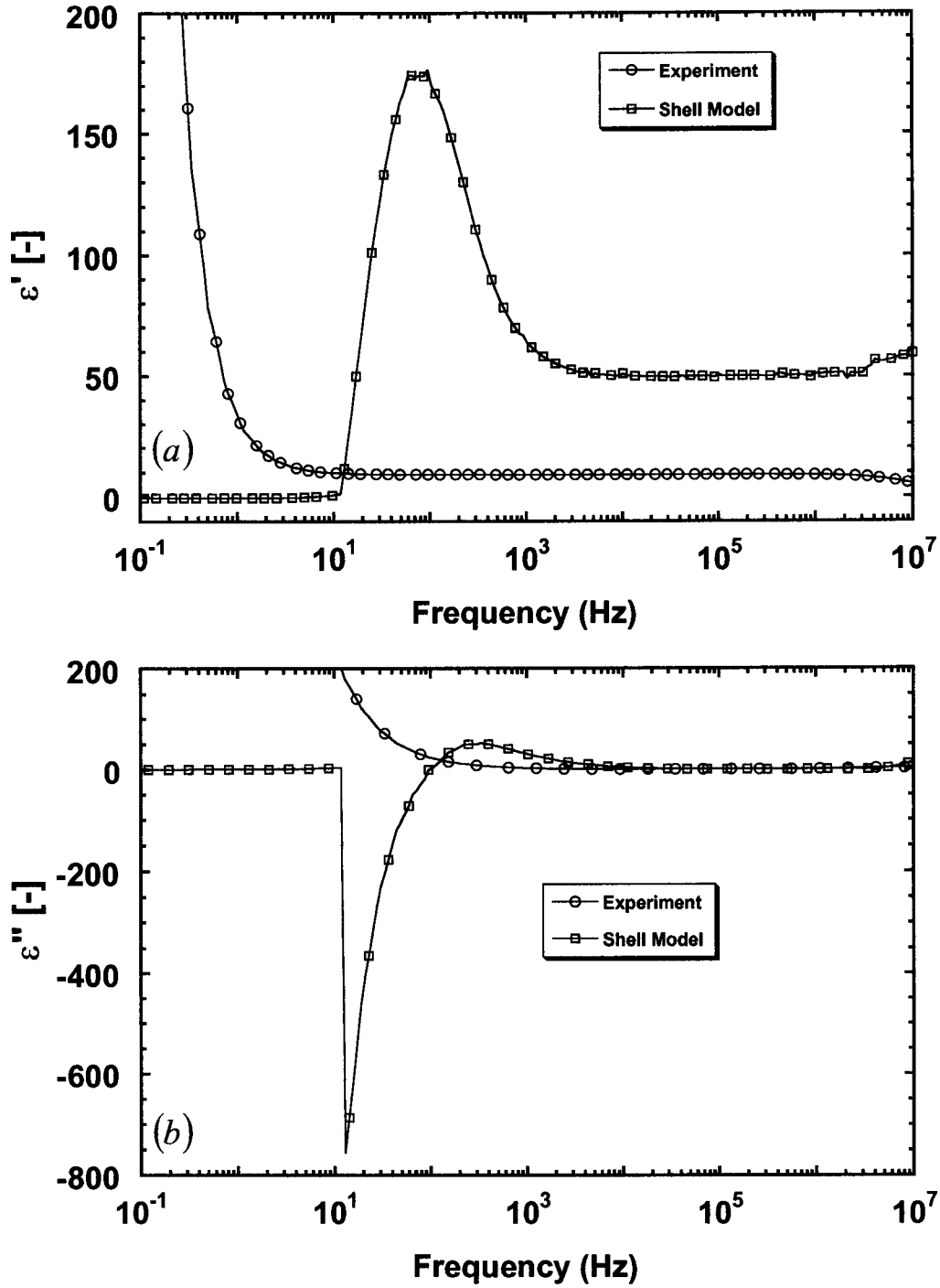

Fig C6: Comparing the frequency dependent (a) capacitive spectrum $\varepsilon'(\omega)$ and (b) loss spectrum $\varepsilon''(\omega)$ of pure 5CB with a hypothetical shell material at 32 °C. The first solution of Eq. (C2) with a = 1.1.

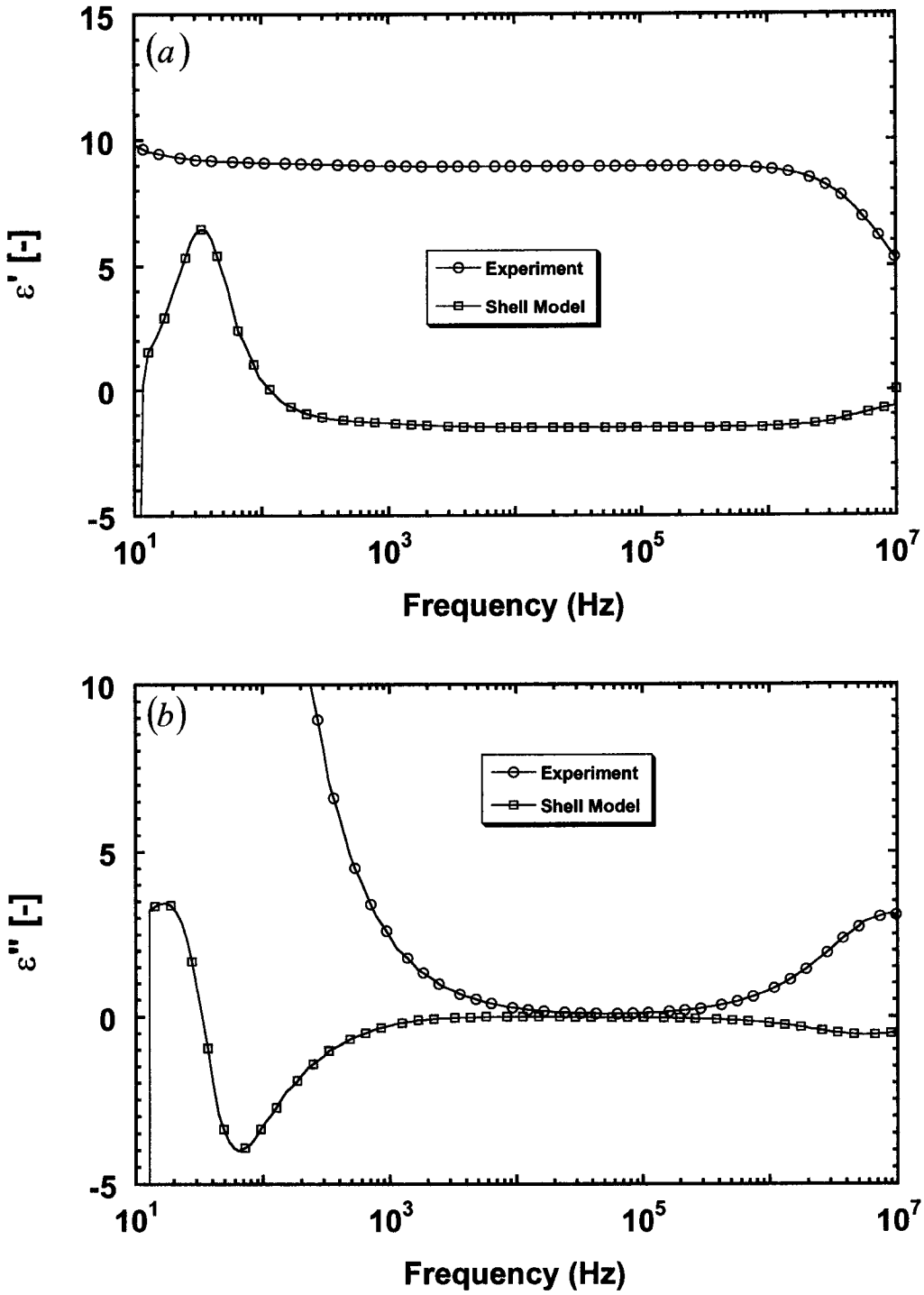

Fig C7: Comparing the frequency dependent (a) capacitive spectrum $\varepsilon'(\omega)$ and (b) loss spectrum $\varepsilon''(\omega)$ of pure 5CB with a hypothetical shell material at 32 °C. The second solution of Eq. (C2) with a = 1.1.

C.4 Ultimate Disappearance of Loss Peak

At temperatures above the nematic-isotropic transition, where the core liquid crystal molecules are in the isotropic state, those in the interfacial region still interact with the interface. This interaction can induce finite order to the molecules in the interfacial region even in the isotropic phase, unless the temperature is so high that the thermal motion overcomes the anchoring effect. Figure C8 shows the structure of the interface of 5CB on an N, N-dimethyl-N- octadecyl-3-aminopropyltrimethoxysilyl chloride (DMOAP) coated glass surface, as obtained from atomic force microscopy experiments performed above the nematic-isotropic phase transition temperature by Kocevar and Musevic (2001). This order is a decreasing function of temperature and finally approaches zero. The loss of order corresponds to the disappearance of intermediate peak in the dielectric loss; this is evident from Fig. C9, which shows the dielectric constant and dielectric loss factor of a 5% 8CB dispersion in PDMS 200 at high temperatures, where bulk 8CB will be in the isotropic phase. A peak in ε'' and a deflection in ε' are clearly visible at 60 °C and 75 °C, while there is no deflection in ε' and no peak in ε'' at 102 °C and 117 °C. The thin bright ring near the droplet interface, as observed in polarized-light microscopy, disappears only at temperatures exceeding 100 °C for a 5% dispersion of 8CB in PDMS 200.

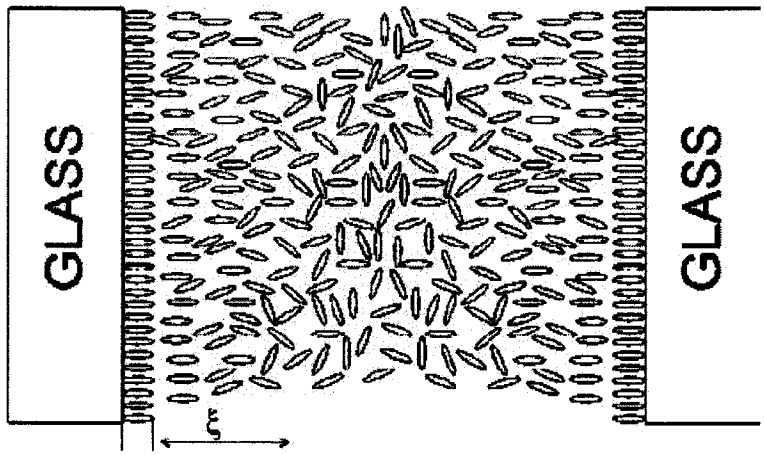

Fig C8: Structure of the interface of 5CB on a DMOAP coated glass surface, as obtained from atomic force microscopy experiments, performed above the nematic-isotropic phase transition temperature. The first, surface-adsorbed layer of LC molecules shows smectic-like elastic compressibility and is stable more than 20 K above the clearing point. The width of the paranematic layer is of the order of the correlation length ξ and increases as we approach the clearing point from above. (Kocevar and Musevic 2001).

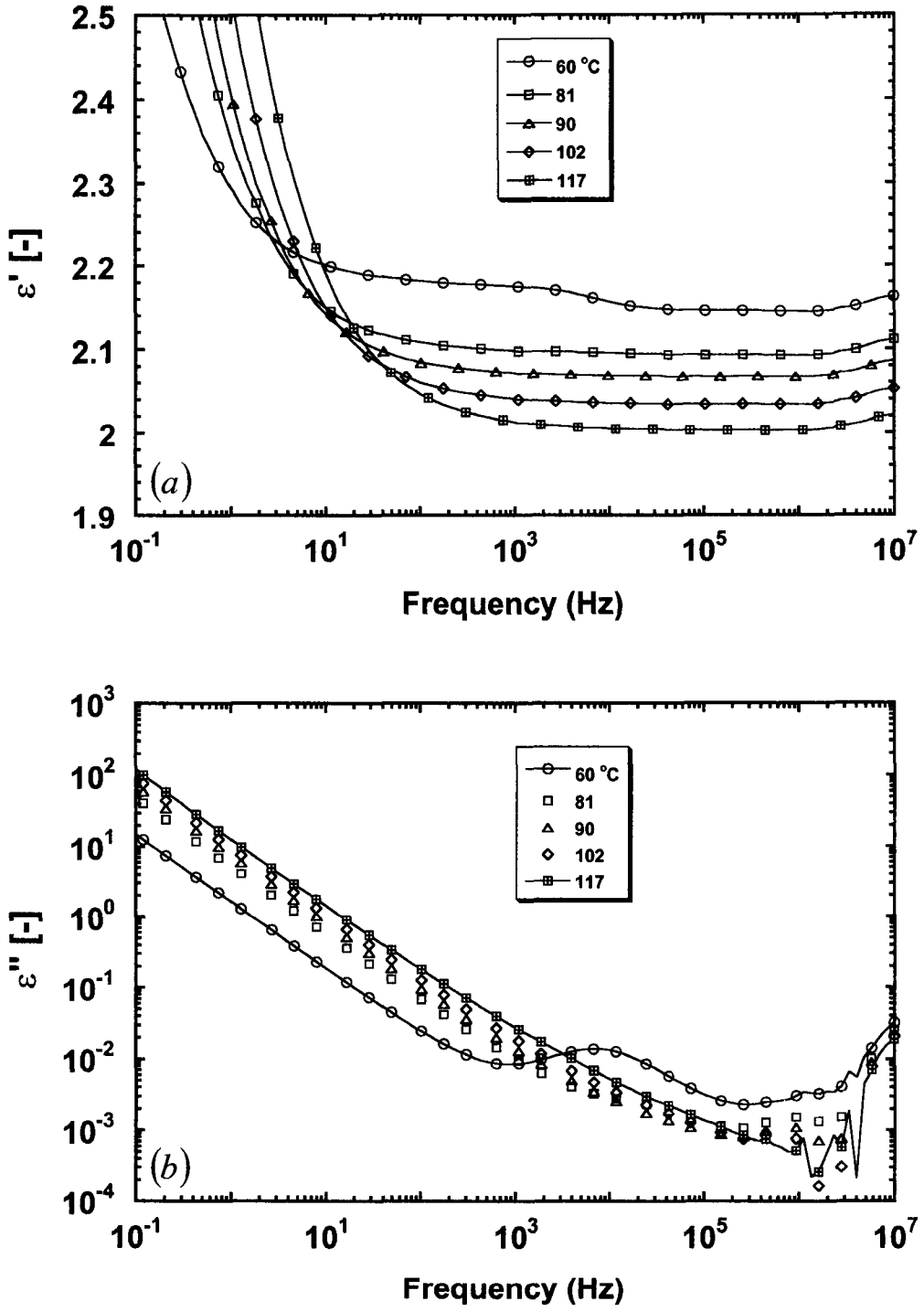

Fig C9: Frequency-dependent (a) capacitive spectrum $\varepsilon'(\omega)$ and (b) loss spectrum $\varepsilon''(\omega)$ of a 5 % dispersion of 8CB in PDMS 200 at temperatures above the nematic-isotropic transition temperature.

C.5 Effect of Varying Voltage (rms and dc-bias)

In a linear viscoelastic measurement, a strain sweep experiment is often performed prior to the frequency sweep experiment to determine the characteristic strain above which storage and loss moduli begin to depend on strain amplitude and are not strictly linear properties. The same concept applies to dielectric spectroscopy, and a voltage sweep experiment is necessary to determine the linear regime beyond which the current-voltage relationship is non-linear. Figure C10 shows the variation of the maximum in dielectric loss with the root-mean square voltage at zero dc-bias. The location of the maximum in loss peak is independent of rms voltage. The magnitude of the loss peak remains constant up to a voltage of 1.5 V at 30 °C and to 1 V at 40 °C, beyond which it begins to decrease with rms voltage. This confirms that the voltage that we have chosen for the frequency sweep experiments lies within the linear regime.

Applying a dc-bias voltage will induce preferential orientation of the molecular dipoles. As pointed out earlier, the location of the loss peak is independent of the rms voltage. The peak location does, however, seem to be weakly dependent on the dc-bias voltage, and the magnitude of the loss peak is dependent on both the dc-bias and the rms voltage. Figure C11 shows the variation of dielectric loss with frequency for a 6.2% dispersion of 5CB in PDMS 200 at 30 °C at different voltages. The capacitive dielectric constant is insensitive to any voltage (ac or dc-bias). When the dc-bias is 0.5 V, the magnitude of the loss peak decreases with rms voltage, while at a dc-bias of 3.0 V, the magnitude of loss peak increases with rms voltage (Fig. C12a). The trend remains the same at 40 °C, as shown in Fig. C12b.

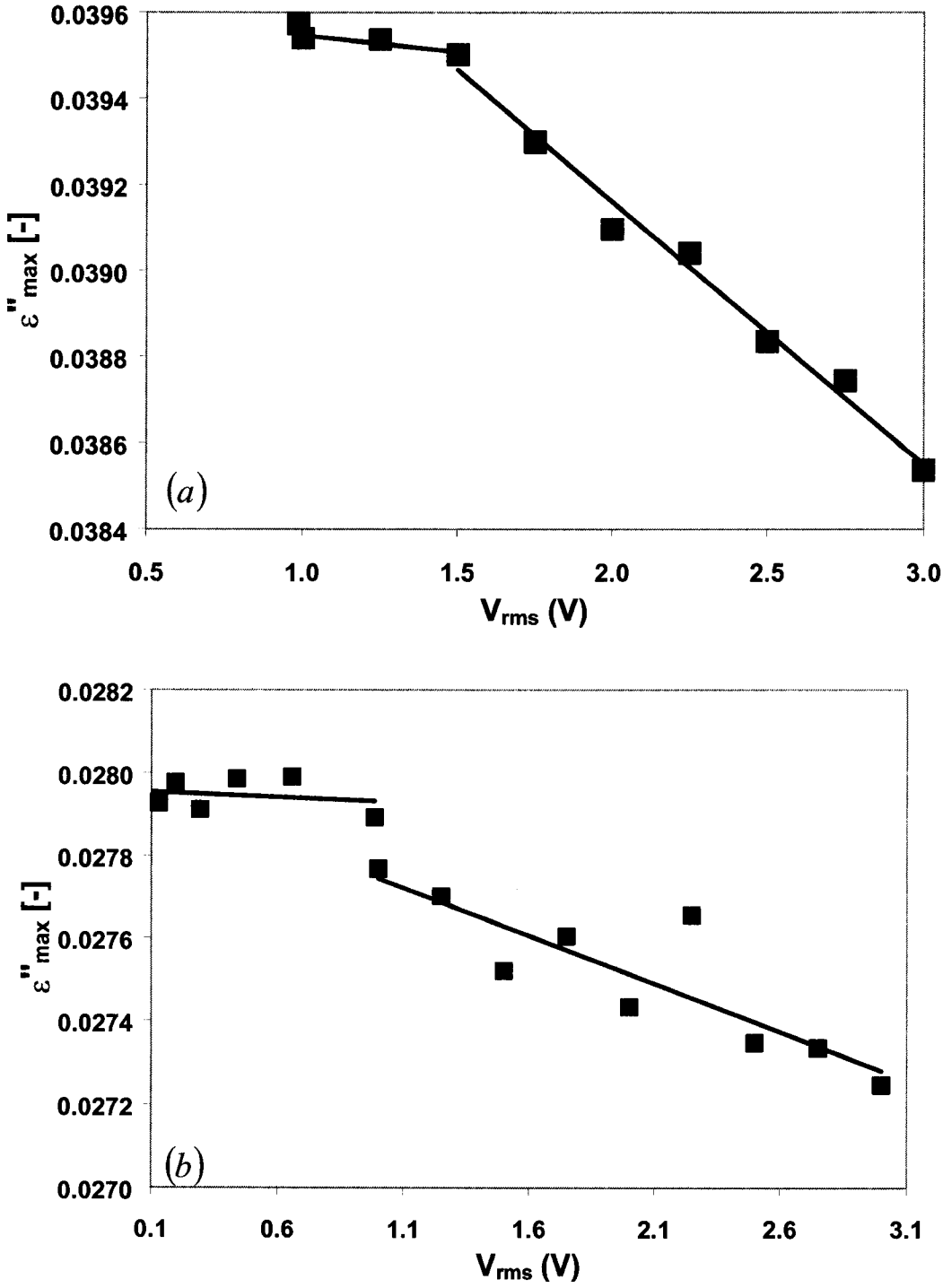

Fig C10: Maximum in dielectric loss versus root-mean-square voltage at (a) 30 °C and (b) 40 °C for 6.2% 5CB dispersion in PDMS with no dc-bias.

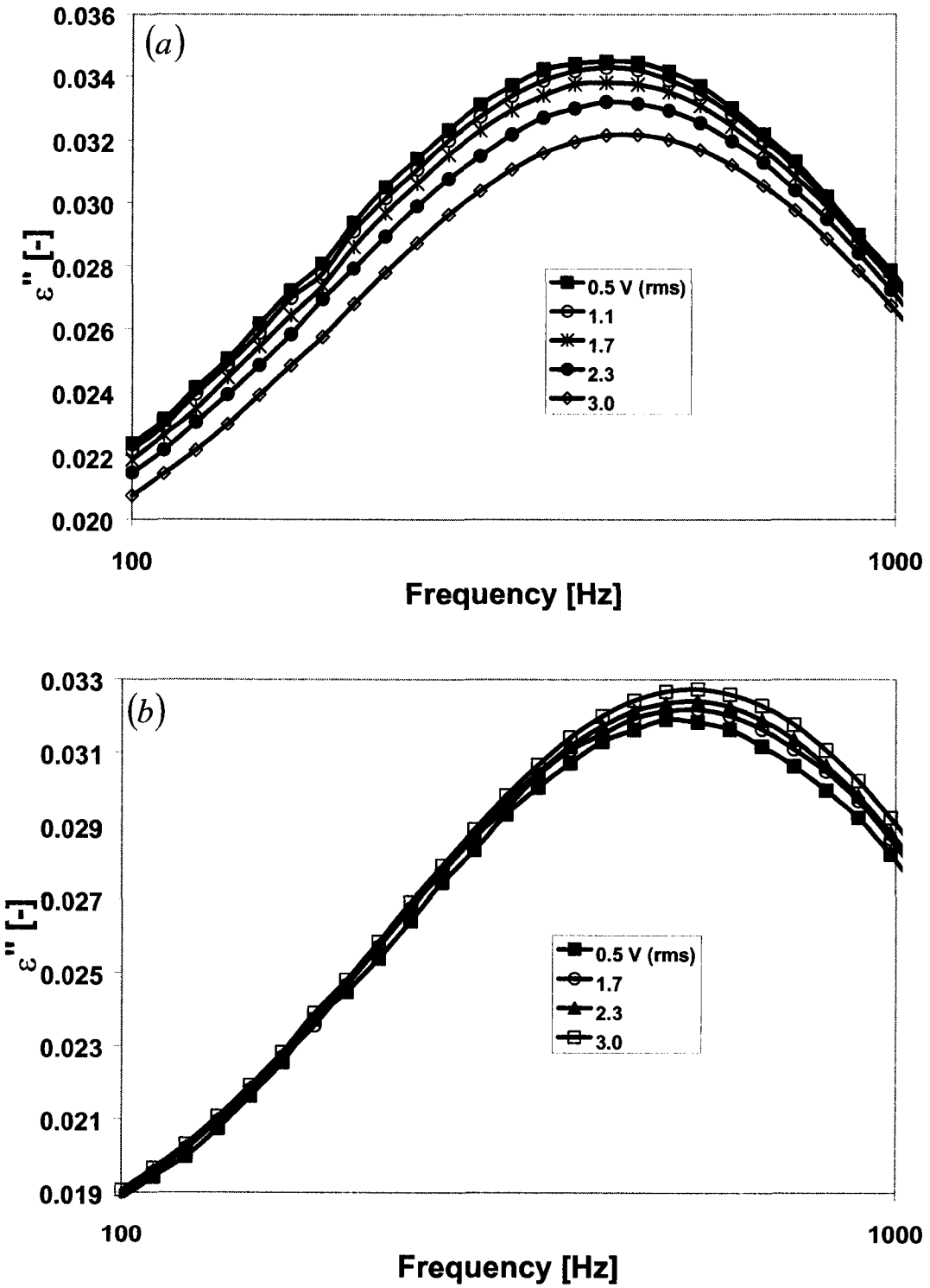

Fig C11: Comparing the frequency dependent loss spectrum $\varepsilon''(\omega)$ of 6.2% dispersion of 5CB in PDMS 200 at 30 °C with dc-bias (a) 0.5 V and (b) 3.0 V.

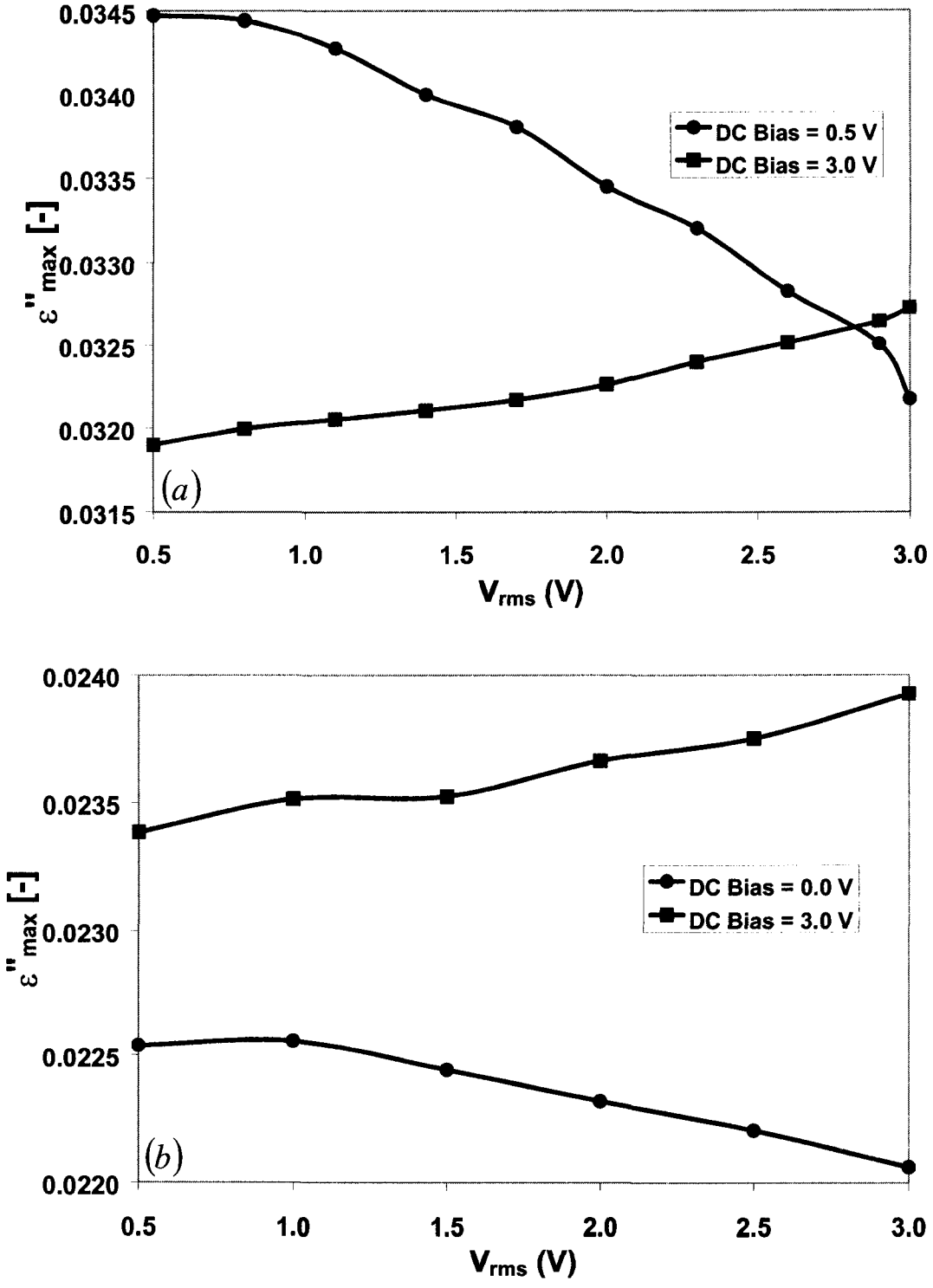

Fig C12: The variation of maximum in dielectric loss with root-mean-square voltage at (a) 30 °C and (b) 40 °C for 6.2% dispersion of 5CB in PDMS 200.

REFERENCES

Adamson, A.W., and A.P. Gast. *Physical Chemistry of Surfaces*; John Wiley and Sons, New York, 1997; Chapter 3.

Andrienko, D., A. Dyadyusha, A. Iljin, Y. Kurioz, and Y. Reznikov, "Measurement of azimuthal anchoring energy of nematic liquid crystal on photoaligning polymer surface," *Mol. Cryst. Liq. Cryst.* **321**, 271-281 (1998).

Batchelor, G.K. *An Introduction to Fluid Dynamics;* Cambridge University Press, Cambridge, 2000.

Bird, R.B., R.C. Armstrong, and O. Hassager. *Dynamics of polymeric liquids. Volume 1: Fluid Mechanics*; John Wiley and Sons, New York, 1987.

Bose, T.K., B. Campbell, S. Yagihara, and J. Thoen, "Dielectric relaxation study of alkylbiphenyl liquid crystals using time-domain spectroscopy," *Phys. Rev. A* **36**, 5767-5773 (1987).

Burghardt, W.R., "Oscillatory shear flow of nematic liquid crystals," *J. Rheol.* **35**, 49-62 (1991).

Burghardt, W.R., and G.G. Fuller, "Role of director tumbling in the rheology of polymer liquid crystal solutions," *Macromolecules* **24**, 2546–2555 (1991).

Carius, H.E., A. Schonhals, D. Guigner, T. Sterzynski, and W. Brostow, "Dielectric and mechanical relaxation in the blends of a polymer liquid crystal with polycarbonate," *Macromolecules* **29**, 5017-5025 (1996).

Chandrasekhar, S. *Liquid Crystals*; Cambridge University Press, Cambridge, 1992.

Clarke, S.J., C.J. Adams, G.J. Ackland. J. White, and J. Crain, "Properties of liquid crystal molecules from first principles computer simulation," *Liq. Cryst.* **22**, 469-475 (1997).

Cognard, J., "The anisotropy of the surface tension of polar liquids: the case of liquid crystals," *J. Adhes.* **17**, 123-134 (1984).

Cogswell, F.N., "Composites of melt-processing polymers having improved processibility," US Patent 4386174 (1983).

deGennes, P.G., and J. Proust. *The Physics of Liquid Crystals*; Clarendon Press, Oxford, 1993.

Doerr, T.P., and P.L. Taylor, "Simulation of liquid crystal anchoring at an amorphous polymer surface from various initial configurations," *Mol. Cryst. Liq. Cryst.* **330**, 491-501 (1999).

Drozd-Rzoska, A., and S. J. Rzoska, "Complex dynamics of isotropic 4-cyano-4-*n*-pentylbiphenyl (5CB) in linear and nonlinear dielectric relaxation studies," *Phys. Rev. E* **65**, 041701 (2002).

Ericksen, J.L., "Theory of Anisotropic Fluids," *Trans. Soc. Rheol.* **4**, 29-39 (1960).

Ericksen, J.L., "Conservation Laws for Liquid Crystals," *Trans. Soc. Rheol.* **5**, 23-34 (1961).

Feynman, R.P., R.B. Leighton, and M. Sands. *Feynman Lectures on Physics, Vol. II: Mainly Electromagnetism and Matter*; Addison-Wesley Publishing Company, Reading, MA, 1964; Chapter 11.

Frunza, S., L. Frunza, A. Schoenhals, H.L. Zubowa, H. Kosslick, H.E. Carius and R. Fricke, "On the confinement of liquid crystals in molecular sieves: dielectric measurements," *Chem. Phys. Lett.* **307**, 167-176 (1999).

Gannon, M.G.J., and T.E. Faber, "The surface tension of nematic liquid crystals," *Philos. Mag. A.* **37**, 117-135 (1978).

Golden, K., R.M. Davies, and T.E.R. Jones. *Ph.D. Thesis*, University of Plymouth, Plymouth, UK (1990).

Griffiths, D.F., and K. Walters, "On edge effects in rheometry," *J. Fluid Mech.* **42**, 379-399 (1970).

Gu, D., and A.M. Jamieson, "Shear deformation of homeotropic monodomains: Temperature dependence of stress response for flow-aligning and tumbling nematics," *J. Rheol.* **38**, 555-571 (1994).

Heuser, G., and E. Krause, "The flow fields of newtonian fluids in cone and plate viscometers with small angles," *Rheol. Acta* **18**, 553-564 (1979).

Hill, N.E., W.E. Vaughan, and M. Davies. *Dielectric Properties and Molecular Behavior;* Van Nostrand Reinhold Company, London, 1969.

Itatani, S., and T. Shikata, "Dielectric relaxation behavior of aqueous dodecyldimethylamineoxide solutions," *Langmuir* **17**, 6841-6850 (2001).

Jamieson, A.M., D. Gu, F.L. Chen, and S. Smith, "Viscoelastic behavior of nematic monodomains containing liquid crystal polymers," *Prog. Polym. Sci.* **21**, 981-1033 (1996).

Jones, T.B. *Electromechanics of Particles*; Cambridge University Press, Cambridge, 1995.

Jones, T.E.R., J.M. Davies, and H.A. Barnes, "Dynamic flow properties of materials in a constant stress rheometer," *Proc IX Intl. Congress on Rheology* **4**, 45-52 (1984).

Jones, T.E.R., J.M. Davies, and A. Thomas, "Fluid inertia effects on a controlled stresss rheometer in its oscillatory mode," *Rheol. Acta* **26**, 14-19 (1987).

Keentok, M., and R.I. Tanner, "Cone-plate and parallel plate rheometry of some polymer solutions," *J. Rheol.* **26**, 301-311(1982).

Keentok, M., and S.C. Xue, "Edge fracture in cone-plate and parallel plate flows," *Rheol. Acta* **38**, 321-348 (1999).

Kocevar, K., and I. Musevic, "Forces in the isotropic phase of a confined nematic liquid crystal 5CB," *Phys. Rev. E* **64**, 051711 (2001).

Kozak, A., J.K. Moscicki, and G. Williams, "On dielectric relaxation in liquid crystals," *Mol. Cryst. Liq. Cryst.* **201**, 1-12 (1991).

Krekhov, A.P., L. Kramer, A. Buka, and A.N. Chuvirov, "Flow alignment of nematics under oscillatory shear," *J. Phys. II France* **3**, 1387-1396 (1993).

Kreul, H.G., S. Urban, and A. Wurflinger, "Dielectric studies of liquid crystals under high pressure: static permittivity and dielectric relaxation in the nematic phase of pentylcyanobiphenyl (5CB)," *Phys. Rev. A* **45**, 8624-8631 (1992).

Krishnaswamy, S., "Experimental determination of the surface tension of two liquid crystals," *Proc. Int. Conf. Liq. Cryst.*, 487-489 (1980).

Larson, R.G. *The Structure and Rheology of Complex Fluids*; Oxford University Press: Oxford, 1999.

Leal, L.G. *Laminar Flow and Convective Transport Processes*; Butterworth-Heinemann Boston, 1992.

Leslie, F.M., "Some constitutive equations for anisotropic fluids," *Quart. J. Mech. Appl. Math.* **19**, 357-370 (1966).

Leslie, F.M., "Some constitutive equations for liquid crystals," *Arch. Rat. Mech. Anal.* **28**, 265-283 (1968).

Li, X., and M.M. Denn, "Interface between a liquid crystalline polymer and a flexible polymer," *Macromolecules*, **35**, 6446-6454 (2002).

Lin, S.-Y., K. McKeigue, and C. Maldarelli, "Diffusion controlled surfactant adsorption studied by pendant drop digitization," *AIChE J.* **36**, 1785-1795 (1990).

Lin, S.-Y., and H.-F. Hwang, "Measurement of low interfacial tension by pendant drop digitization," *Langmuir* **10**, 4703-4709 (1994).

Lin, S.-Y., L.-J. Chen, J.-W. Xyu, and W.-J. Wang, "An examination on the accuracy of interfacial tension measurement from pendant drop profiles," *Langmuir* **11**, 4159-4166 (1995).

Lu, J.-M., T.-Y. Yu, and Y.-L. Yang, "Molecular field theory and monte carlo simulation of phase transition in surface-aligned nematic films," *Science in China, ser. A* **36**, 624-631 (1993).

Lubensky, T.C., D. Pettey, N. Currier, and H. Stark, "Topological defects and interactions in nematic emulsions," *Phys. Rev. E* **57**, 610-625 (1998).

Macdonald, I.F., "Parallel superposition of simple shearing and small amplitude oscillatory motions," *J. Rheol.* **17**, 537-555, (1973).

Macosco, C.W. *Rheology: Priciples, Measurements and Applications*; John Wiley and Sons, New York, 1994.

Maude, A.D., and K. Walters, "Approximate theory for oscillatory experiments with a cone-and-plate viscometer," *Nature* **201**, 913-914 (1964).

Mijovic, J., and J. Sy, "Dipole dynamics and macroscopic alignment in molecular and polymeric liquid crystals by broad-band dielectric relaxation spectroscopy," *Macromolecules* **33**, 9620-9629 (2000).

Nally, M.C., "The oscillatory motion of an elastico-viscous liquid in a cone-and-plate viscometer," *Brit. J. Appl. Phys.* **16**, 1023-1031 (1965).

O'Konski, C.T., and F.E. Harris, "Electric free energy and the deformation of droplets in electrically conducting systems," *J. Phys. Chem.* **61**, 1172-1174 (1957).

Olangunju, D.O., "Inertial effect on the stability of viscoelastic cone-and-plate flow," *J. Rheol.* **38**, 151-168 (1993).

Olangunju, D.O., and L.P. Cook, "Secondary flows in cone and plate flow of an Oldroyd-B fluid," *J. Non-Newtonian Fluid Mech.* **46**, 29-47 (1993a).

Olangunju, D.O., and L.P. Cook, "Linear stability analysis of cone and plate flow of an Oldroyd-B fluid," *J. Non-Newtonian Fluid Mech.* **47**, 93-105 (1993b).

Olangunju, D.O., "Effect of free surface and inertia on viscoelastic parallel plate flow," *J. Fluid Mech.* **343**, 317-330 (1997).

Paddon, D.J., and K. Walters, "On edge effects and related sources of error in rotational rheometry," *Rheol. Acta* **18**, 565-575 (1979).

Palierne, J.F., "Linear rheology of viscoelastic emulsions with interfacial tension," *Rheol. Acta* **29**, 204–214 (1990).

Parodi, O., "Stress Tensor for a Nematic Liquid Crystal," *J. Phys. (Paris)* **31**, 581-584
(1970).

Rai, P.K., M.M. Denn, and C. Maldarelli, "Interfacial tension of liquid crystalline droplets," *Langmuir* **19**, 7370-7373 (2003).

Renardy, Y., and D.O. Olangunju, "Inertial effect on stability of cone-and-plate flow. Part 2: Non-axissymmetric modes," *J. Non-Newtonian Fluid Mech.* **78**, 27-45 (1998).

Rey, A.D., and M.M. Denn, "Dynamical phenomenon in liquid-crystalline materials," *Annu. Rev. Fluid Mech.* **34**, 233-266 (2002).

Rondelez, F., D. Diguet, and G. Durand, "Dielectric and resistivity measurements on room temperature nematic MBBA," *Mol. Cryst. Liq. Cryst.* **15**, 183-189 (1971).

Self, R.H., C.P. Please, and T.J. Slucking, "Deformation of nematic liquid crystals in electric field,: *Euro. J. Appl. Maths* **13**, 1-23 (2002).

Sinha, G.P., and F.M. Aliev, "Dielectric spectroscopy of liquid crystal in smectic, nematic, and isotropic phases confined in random porous media," *Phys. Rev. E.* **58**, 2001-2010 (1998).

Skarp, K., S.T. Lagerwall, and B. Steller, "Measurements of hydrodynamic parameters for nematic 5CB," *Mol. Cryst. Liq. Cryst.* **60**, 212-236 (1980).

Song, B., and J. Springer, "Surface phenomenon of liquid crystalline substances: temperature dependence of surface tension," *Mol. Cryst. Liq. Cryst.* **307**, 69-88 (1997).

Stark, H. *Ph.D. Thesis*, Institut für Theoretische und Angewandte Physik, University of Stuttgart, Stuttgart, Germany (1999).

Tintaru, M., R. Moldovan, T. Beica, and S. Frunza, "Surface tension of some liquid crystals in cyanophenyl series," *Liq. Cryst.* **28**, 793-797 (2001).

Torza, S., R.G. Cox, and S.G. Mason, "Electrohydrodynamic deformation and burst of liquid drops," *Phil. Trans. R. Soc. Lond. A* **269**, 295-319 (1971).

Walters, K., "Oscillatory experiments with a cone-and-plate viscometer," *Nature*, **200**, 458-458 (1963).

Walters, K. *Rheometry*; Chapman and Hall, London, 1975.

Walters, K., and N.D. Waters, "On the use of a Rheogoniometer. Part I – Steady Shear". In: R.E. Wetton, and R.W. Whorlow (eds) *Polymer Systems: Deformation and Flow*; Macmillan, London (1968).

Walters, K., and R.A. Kemp, "On the use of a Rheogoniometer. Part II – Oscillatory Shear". In: R.E. Wetton, and R.W. Whorlow (eds) *Polymer Systems: Deformation and Flow*; Macmillan, London (1968a).

Walters, K., and R.A. Kemp, "On the use of a Rheogoiniometer. Part III – Oscillatory shear between parallel plates," *Rheol. Acta* **7**, 1-8 (1968b).

Weingartner, H., A. Knocks, W. Schrader, and U. Kaatze, "Dielectric spectroscopy of the room temperature molten salt ethylammonium nitrate," *J. Phys. Chem. A* **105**, 8646-8650 (2001).

Williams, G., "Dielectric relaxation behavior of liquid crystals". In: G. Luckhurst, and C. Verancini (eds) *The Molecular Dynamics of Liquid Crystals;* Kluwer Academic Publishers, Dordrecht, 1994.

Wu, J., and P.T. Mather, "Interfacial tension in an immiscible blend containing a thermotropic liquid-crystalline polymer," paper HS12, 74th Ann. Meeting Society Rheology, Minneapolis, Oct. 13-17, 2002.

Wu, S. *Polymer Interface and Adhesion;* Dekker, New York, 1982.

Zakharov, A.V., and R.Y. Dong, "Dielectric and elastic properties of liquid crystals," *Phys. Rev. E* **64**, 031702 (2001).